Measurements of the B** and B$_s^{**}$ Mass Peaks and B Mixing using Data from the OPAL Experiment

Andrew Nigel Bell

Thesis submitted for the degree of
Doctor of Philosophy

October 1997

School of Physics and Space Research
Faculty of Science
The University of Birmingham

Synopsis

The OPAL detector has been used to collect data from decays of the Z^0 boson, produced with e^+e^- collisions at the LEP collider. Events recorded between 1991 and 1995 were used in measurements of time averaged B mixing and to study the properties of the B^{**} and B_s^{**} mass peaks.

The time averaged B mixing parameter χ was measured using data collected from 1992 to 1994. The method involved the measurement of jet charge in one hemisphere and lepton charge in the opposite hemisphere to identify the charge of the b quark at production and decay. The value measured is:

$$\chi = 0.100 \pm 0.012(\mathrm{stat}) \pm 0.020(\mathrm{syst})$$

The properties of the B^{**} and B_s^{**} mass peaks have been studied using the full data set. B hadrons were reconstructed using a vertex weight method and then combined with pions(B^{**}) or kaons(B_s^{**}) coming from the primary vertex. Monte Carlo data was used extensively in the optimisation of the B reconstruction and initial studies of the background. The background was finally estimated using the data sample itself.

The Q distribution of the B^{**} signal was fitted to a combination of two narrow and one wide Breit Wigner convoluted with the experimental resolution. The following parameters were then measured from a fit to this distribution.

$$\begin{aligned}
Q(1) &= 0.277 \pm 0.007(\mathrm{stat})^{+0.008}_{-0.023}(\mathrm{syst}) \\
Q(2) &= 0.367 \pm 0.018(\mathrm{stat})^{+0.015}_{-0.068}(\mathrm{syst}) \\
\frac{\sigma_{B^{**}}}{\sigma_{b-jet}} &= 0.294 \pm 0.018(\mathrm{data\ stat}) \pm 0.0015(\mathrm{mc\ stat})^{+0.024}_{-0.023}(\mathrm{syst})
\end{aligned}$$

The B_s^{**} signal was also fitted to a combination of two narrow and one wide Breit Wigner convoluted with the experimental resolution and the following parameters were then measured

$$\begin{aligned} Q(1) &= 0.0363 \pm 0.0028(\mathrm{stat})^{+0.0003}_{-0.0055}(\mathrm{syst}) \\ Q(2) &= 0.117 \pm 0.012(\mathrm{stat})^{+0.007}_{-0.020}(\mathrm{syst}) \\ \frac{\sigma_{B_s^{**}}}{\sigma_{b-jet}} &= 0.0576 \pm 0.0036(\mathrm{data\ stat}) \pm 0.0011(\mathrm{mc\ stat})^{+0.0059}_{-0.0061}(\mathrm{syst}) \end{aligned}$$

These results have been compared with similar measurements from other experiments.

Authors Contribution

The work presented in this thesis was carried out within the OPAL collaboration. This collaboration consists of several hundred physicists and technicians, each with their own area of expertise. As a large number of people are necessary to maintain the experiment and perform analysis it is often difficult to distinguish an individual's work. Therefore in this section I wish to highlight the contribution I have made to OPAL in the last three years.

The Birmingham University OPAL group is responsible for the maintenance and smooth running of the Muon Endcap subdetectors, which were built in conjunction with the Rutherford Appleton Laboratory. While resident at CERN for almost two years I acted as the Birmingham representative for the endcap. This involved sharing the daily monitoring of checks of the gas and high voltage systems, attending weekly OPAL status meetings and responding to any problems from the pit at any time of the day or night. I also made contributions to the monitoring software for the detector.

During my first year I started work on the measurement of B mixing in collaboration with others. My contribution was the measurement of a quantity called the charge separation. In my second year I finished this analysis and moved onto measuring the B^{**} and B_s^{**} mass peaks significantly extending early work within the collaboration. The previous work had been a high purity and low efficiency study, my aim was to increase the efficiency and to include the entire LEP 1 dataset. All of the B^{**} studies that are included are my own work.

Acknowledgements

I would like to thank the British tax-payers who generously funded my PhD via the Particle Physics and Astronomy Research Council.

I would like to thank all those people who have assisted me in the past three years. For much assistance with my thesis work thanks go to my supervisor Peter Watkins, and to Martin Jimack for putting up with my many blunders while at CERN (and afterwards). Also thanks to Dave Rees for all the help he gave me when I started my first real analysis with him. John Wilson, Pedja Jovanovic and several others have helped me when I've been trying to fix problems with the OPAL muon endcaps.

I would also like to thank Mary Elizabeth and Sue Cannon for making my stay in Geneva as trouble free as possible. Also I would like to thank the people at UCL college for their understanding when I rolled their van one evening on the way to the pit, I know it wasn't a pretty sight afterwards! I would also like to say thanks to the hospital staff in Geneva for struggling to communicate with me in English while my hip recovered from it's mystery infection!

Thanks should also go to all the students at Birmingham and CERN for trying to make me think of something other than work. When I first went to CERN Dave Rigby was a source of many wonderful internet sites and could always be relied on for a distraction when you needed one. I would like to thank all those who went skiing with me during the two winters I lived in Geneva, although I would like to forget some of the positions I found myself in while trying to learn how to ski properly.

Thanks should also go to a company called Insight Logistics for giving me a reason to finish this thesis on time (well nearly).

Finally thank you to my family for their support and understanding during my student years.

Andrew Bell

October, 1997.

Contents

List of Figures

List of Tables

Chapter 1

Introduction

1.1 Standard Model

There are four known forces that are thought to be fundamental in nature and a small number of elementary particles which are influenced by these forces. The standard model successfully describes the electromagnetic, weak and strong interactions using two renormalisable gauge theories. The gravitational force is very weak when compared to the other forces at the energies that current accelerators can reach, hence its omission from the standard model is assumed to have an immeasurably small effect on any numerical results that can be compared with experimental data.

The Standard model contains two different species of elementary particles, the bosons and the fermions. The bosons are the gauge particles that mediate forces (e.g. the photon mediates the electromagnetic force) and have a spin of 1[a]. The fermions are further divided into quarks and leptons both having spin 1/2.

1.1.1 Quarks and Leptons

There are six flavours of quarks in the standard model up, charm and top having charge +2/3[b], and down, strange and bottom having charge -1/3. There are also six

[a]in units of $\hbar$
[b]in units of the electronic charge

types of lepton, the electron, muon and tau, having charge -1, and their corresponding neutrinos which have zero charge. The quarks and leptons can be grouped together into generations of a doublet of quarks and a doublet of leptons, as shown in table 1.1. Each successive generation is a heavier version of the previous one. Each fermion

Generations		
I	II	III
$\begin{pmatrix} \mathrm{u} \\ \mathrm{d} \end{pmatrix}$	$\begin{pmatrix} \mathrm{c} \\ \mathrm{s} \end{pmatrix}$	$\begin{pmatrix} \mathrm{t} \\ \mathrm{b} \end{pmatrix}$
$\begin{pmatrix} \nu_{\mathrm{e}} \\ \mathrm{e}^- \end{pmatrix}$	$\begin{pmatrix} \nu_\mu \\ \mu^- \end{pmatrix}$	$\begin{pmatrix} \nu_\tau \\ \tau^- \end{pmatrix}$

Table 1.1: The Fermion generations.

can be either left-handed or right-handed[c] except for the neutrinos which are always left-handed.

Each of the quarks and leptons have anti-particle partners with opposite quantum numbers (except spin) but the same mass. The anti-quarks are denoted by a bar above the particle name (e.g. the anti up quark is written $\overline{\mathrm{u}}$). The anti-leptons are denoted by their charge (e.g. the anti electron is written e^+).

1.1.2 Bosons

The interactions between fermions are mediated by the exchange of virtual[d] gauge bosons. The electromagnetic force is mediated by the massless photon (γ), the weak

[c]A right- (left-) handed particle has its spin vector aligned parallel (anti-parallel) to its momentum vector.

[d]The exchange process must take place over a time limited by the uncertainty principle in order to satisfy conservation laws.

interaction by the massive $W^{\pm}$ and Z^0 bosons and the strong interaction by an octet of massless gluons (g).

The electromagnetic interaction has an infinite range whereas the mass of the $W^{\pm}$ ($\simeq 80$ GeV/c^2) and the Z^0 ($\simeq 90$ GeV/c^2) gives the weak interaction an effective range of 10^{-18}m. The strong interaction has a typical range of $\leq 10^{-15}$m for reasons described in section 1.1.7.

The interaction of the gauge bosons with the fundamental fermions and the self-interaction of gauge bosons is described by the standard model using a set of relativistically invariant gauge theories.

1.1.3 Gauge Field Theories

Any system of interacting particles can be represented by a Lagrangian density, the symmetries of which will correspond to conserved quantities in Nature. The first such theory was quantum electrodynamics (QED) which describes the electromagnetic interaction. It is the most accurate theory known and has been tested to very high levels of precision.

For a quantum mechanical system of fermions, mediated by virtual bosons, the phase of the descriptive wavefunction is unobservable and thus can be varied without changing the physical characteristics of the system. Demanding invariance under a global change in this phase (or gauge) produces charge conservation in QED. The more stringent requirement of local gauge invariance (for which we require an invariant Lagrangian after arbitrary phase changes at each point in space-time) necessitates the introduction of compensating gauge fields, which correspond to the the gauge bosons. For example in QED the properties of the photon are predicted.

In order to construct successful field theories, that yield calculable results which can be compared to experimental observations, a procedure called 'renormalisation' must be performed.

1.1.4 Renormalisation

Feynman developed the tools which allow the possibility for a given process (say,

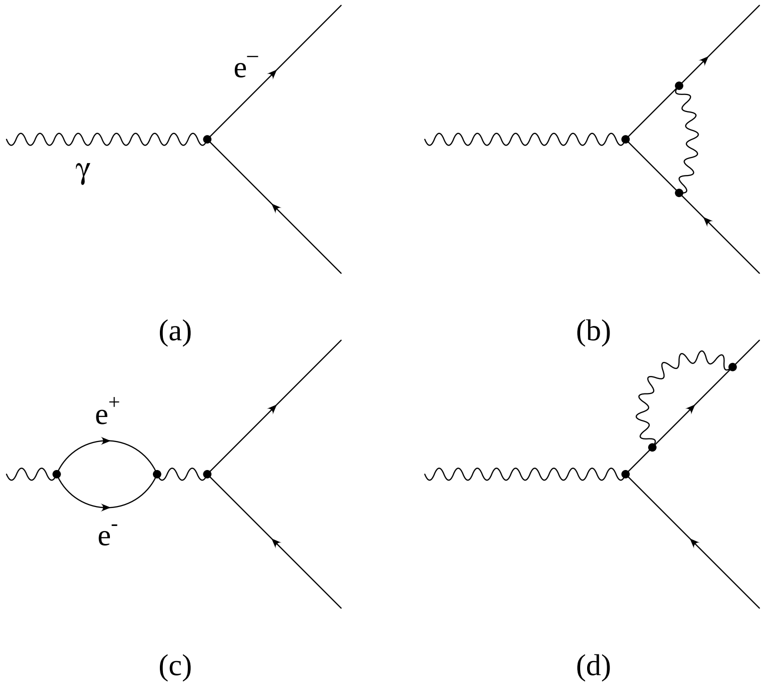

Figure 1.1: Feynman diagrams for the γ–e^- scattering process. Diagram (a) shows the basic zeroth order process and diagram (b) is a first order correction. Diagrams (c) and (d) show processes which cause the probability amplitude calculations for the scattering process to become divergent.

γ–e^- scattering) to be calculated from a pictorial representation. A unique Feynman diagram is used to represent each term in the perturbation expansion for the scattering process and the total probability is the sum of all the possible Feynman diagrams that have incoming and outgoing lines representing the interacting particles.

For example, figure 1.1a shows the basic zeroth order vertex in a simple QED γ–e^- scattering process, and figure 1.1b shows a first order correction. The probabilities for both these processes can be calculated through well behaved convergent expressions and compared to results from precise scattering experiments. Figures 1.1c and 1.1d show cases where the production of an e^+e^- pair from a γ or the bremsstrahlung of a γ from an electron are totally internal to one line of the Feynman diagram. If such diagrams are included with the lowest order diagrams the calculations become divergent and the net result becomes unphysical because the momenta of the internal lines are free and therefore must be integrated over an infinite range.

Renormalisation gets around these infinities by absorbing the troublesome diagrams into the original definition of the electron or photon lines. The charge of the electron associated with the lowest order QED interaction (figure 1.1a) is not the familiar charge measured in the laboratory (1.6×10^{-19}C), but rather, the bare charge. The measured charge is this bare charge including the higher order corrections. The theory is therefore renormalised by introducing an experimentally measured quantity. In the case of QED, this is the charge of the electron. One consequence of this is that the higher the energy of the probe used to investigate the structure of the electron, the larger the electron charge appears to be, since the outer layers of higher order 'shielding' are penetrated.

A quantity called α is used to denote the strength of the electromagnetic interaction[e] This is not a constant but is said to 'run' (vary) with the measurement energy. For example, $\alpha \simeq 0.0073$ when evaluated in low energy experiments, whereas, $\alpha \simeq 0.0078$ when measured by experiments operating around the Z^0 resonance. The coupling constant for the strong interaction also 'runs' (but in the opposite sense), as described in section 1.1.7.

1.1.5 The Electroweak Theory

The electromagnetic and weak interactions were first unified by Glashow in 1961 [2]. Some years later Weinberg and Salam reformulated this work [3] in terms of a renormalisable gauge field theory. In this theory the left handed elementary fermions in each generation are considered as two states of a system with weak isospin of $\frac{1}{2}$ ($I^W = \frac{1}{2}$). The right handed fermions enter the theory as singlet states with $I^W = 0$. The members of each doublet differ in their third component of weak isospin, I_3^W. Local gauge invariance is now demanded under rotations in weak isospin space, which transforms a particle into its doublet partner, e.g. an electron is transformed into an electron-neutrino. These transformations are known as the $\mathrm{SU(2)_L}$ rotation group, where the subscript L denotes only left handed particles are involved. In order to maintain gauge invariance under $\mathrm{SU(2)_L}$ transformations three fields must be introduced (W_i, $i = 1, 2, 3$). The $W^\pm$ bosons are then identified as the gauge bosons exchanged when a charged current interaction takes place. The physical fields associated to the $W^\pm$ are a linear

[e] $\alpha = \frac{e^2}{4\pi}$, where e is the charge of the electron.

combination of the W_1 and W_2 fields,

$$W^{\pm} = \frac{1}{\sqrt{2}}(W_1 \mp W_2) \ . \tag{1.1}$$

The $\mathrm{SU(2)_L}$ transformation alone cannot describe weak neutral current interactions, which is known to involve both left and right handed particles. In order to explain the weak neutral current interaction, a $\mathrm{U(1)_Y}$ gauge transformation is introduced and invariance under the combined transformation $\mathrm{SU(2)_L \times U(1)_Y}$ is required. The $\mathrm{U(1)_Y}$ transformation gives rise to a neutral field that couples to weak hypercharge, defined as

$$Y = 2(Q - I_3^W) \tag{1.2}$$

where Q is the electromagnetic charge, I_3^W is the third component of isospin and Y is the weak hypercharge. The physical weak neutral current and electromagnetic fields which correspond to the $\mathrm{Z^0}$ and the γ (A) are given by orthogonal linear combinations of the neutral weak isospin field, W_3, and the weak hypercharge field, B,

$$\mathrm{Z} = W_3 \cos\theta_W - \mathrm{B} \sin\theta_W \tag{1.3}$$

$$\mathrm{A} = W_3 \sin\theta_W - \mathrm{B} \cos\theta_W \tag{1.4}$$

where the weak mixing angle (θ_W) gives the relative strength between the weak and electromagnetic interactions. The weak mixing angle is not predicted by the Standard Model and must be determined experimentally.

1.1.6 Spontaneous Symmetry Breaking

The electroweak theory described so far is not consistent with nature since all the weak gauge bosons predicted are massless whereas they are very massive in nature. This discrepancy is remedied by the introduction of a complex scalar Higgs field with non-zero vacuum expectation value. This field spontaneously destroys the symmetry [5] of the gauge theory, but imbues the three weak gauge bosons with mass and - in the simplest model - leaves one scalar Higgs field uncoupled, this is thought to manifest itself as a massive scalar Higgs boson $\mathrm{H^0}$. The theory makes no absolute predictions for particle masses, however the photon and gluon masses are required to be zero and the $W^{\pm}$ and Z^0 masses can be calculated from the measured weak and electromagnetic coupling constants. The fermion masses have to be experimentally determined. The Higgs boson has not yet been found, but lower and upper bounds for the mass can be determined from other measured parameters and results. Recent direct searches for the Standard Model Higgs boson at LEP set the Higgs mass at more than 77 GeV at the 95% confidence level [6]. The combination of electroweak results from the four LEP experiments and the SLD collaboration set the Higgs boson mass at less than 465 GeV also at the 95% confidence level [7]. The next generation of experiments - particularly the LHC [8] - will be able to make more stringent tests on the Higgs hypothesis.

1.1.7 Quantum Chromodynamics

Quantum Chromodynamics (QCD) is a gauge invariant field theory based on the $SU(3)_c$ 'colour' group structure, proposed by Fritzsch, Leutwyler and Gell-Mann in 1973 [9]. It describes the strong interaction that binds quarks (q) into composite particles called baryons (qqq) and mesons ($q\overline{q}$). The strong force is mediated by gluons (g).

Gluons couple to the colour charge of quarks and other gluons. Colour charge can be thought of as analogous to the electrical charge in quantum electrodynamics. Three types of colour are postulated: red ($\overline{\text{red}}$), green ($\overline{\text{green}}$) and blue ($\overline{\text{blue}}$). The number of colours has been measured at electron-positron colliders where the cross-section for $e^+e^- \rightarrow q\overline{q}$ is three times greater than expected from calculations which contain no colour. There are eight physical gluons needed to maintain local gauge invariance under $SU(3)_c$, each of the gluons carries a colour-anticolour combination, while quarks carry a single colour.

It is postulated that only colourless particles can be directly observed and so single quarks cannot exist alone. This is called colour confinement and arises as a direct consequence of the asymptotic freedom associated with the strength of the strong force increasing with quark separation. Isolated quarks or composite quark states of non-zero net colour have never been observed.

The predictive power of electroweak calculations is very impressive. Such a strong claim cannot be made of QCD calculations due to the magnitude of the strong coupling constant, $\alpha_s(90\mathrm{GeV}) \sim 0.12$, compared to the magnitude of the electromagnetic coupling constant, $\alpha(90\mathrm{GeV}) \sim 0.008$. The coupling constant enters into probability amplitude calculations for a given process to the power of the number of boson-fermion vertices. The magnitude of the strong coupling constant increases with decreasing energy ($\alpha_s(10\mathrm{GeV}) \sim 0.19$). Workable perturbative calculations in QCD are therefore restricted to applications involving small distances (or large momentum transfers), where α_s is relatively small and the quarks can be considered as essentially non-interacting states[f]. For example, in Figure 1.2 the e^+e^- pair annihilates into an excited photon or Z^0 which subsequently decays into a primary $q\overline{q}$ pair. Electroweak theory predicts the probability of such decays with a relative accuracy of $\sim 2\%$. These primary quarks radiate gluons which can convert into $q\overline{q}$ pairs or radiate further gluons causing a $q\overline{q}$ shower. In principle, perturbative QCD should be able to provide a fully quantitative description of this process, although to date most calculations are only carried out to second order in α_s. The quarks dress themselves as hadrons by exciting the vacuum to provide further $q\overline{q}$ pairs and are observed as physical jets of baryons and mesons. Various empirical models exist to describe this process, since at energy scales typical of hadronic processes α_s becomes large enough ($\alpha_s \sim 1$) that perturbation theory can no longer be applied.

1.1.8 Quark Generation Mixing

In 1963, Cabibbo postulated that d and s quarks could mix, in order to explain experimental observations of strangeness changing currents [10]. Seven years later, the GIM (Glashow, Iliopoulus and Maiani) mechanism was introduced and predicted an extra quark, charm, to be the isospin partner of the strange quark. The GIM mechanism allowed the lack of flavour changing neutral currents in kaon decays to be explained [11]. In 1973 Kobayashi and Maskawa realised that adding a third quark generation would allow CP violation to be accommodated in the Standard Model [12]. The violation of a

[f]A free parameter in QCD, Λ_{QCD}, sets the scale at which α_s becomes 'strong'. This denotes the boundary between quasi-free quarks and gluons and bound hadronic states. It is determined by experiment to lie in the range $0.1 \rightarrow 0.5$ GeV [1].

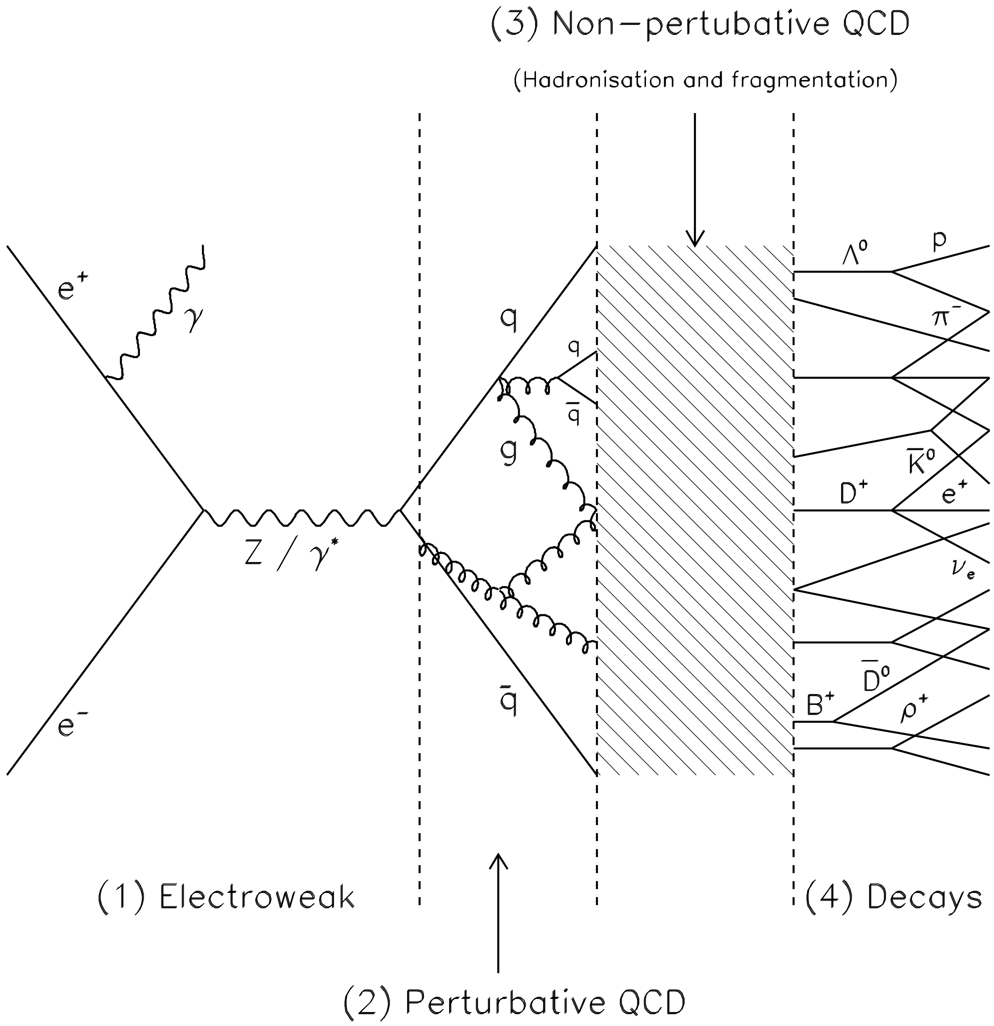

Figure 1.2: A schematic representation of the creation of a final multihadronic final state from an e^+e^- interaction at a centre of mass energy around the mass of the Z^0 gauge boson.

combined charge conjugation (C) and parity (P) symmetry was observed for the weak interaction in 1964, in the decay of neutral kaons [13].

Kobayashi and Maskawa (KM) proposed that a set of weak eigenstates (d$'$, s$'$, b$'$) should be invoked as a linear mix of the flavour eigenstates (d, s, b) :

$$\begin{pmatrix} \mathrm{d}' \\ \mathrm{s}' \\ \mathrm{b}' \end{pmatrix} = V_{\mathrm{KM}} \begin{pmatrix} \mathrm{d} \\ \mathrm{s} \\ \mathrm{b} \end{pmatrix}, \tag{1.5}$$

where the unitary rotation matrix is given by :

$$V_{\mathrm{KM}} = \begin{pmatrix} |\mathrm{V_{ud}}| & |\mathrm{V_{us}}| & |\mathrm{V_{ub}}| \\ |\mathrm{V_{cd}}| & |\mathrm{V_{cs}}| & |\mathrm{V_{cb}}| \\ |\mathrm{V_{td}}| & |\mathrm{V_{ts}}| & |\mathrm{V_{tb}}| \end{pmatrix}. \tag{1.6}$$

It is only by convention that quarks with electric charge $+\frac{2}{3}$ are unmixed. The matrix elements are not predicted by the Standard Model but they can be measured and constrained experimentally. All the matrix elements can, in principle, be determined from the weak decays of the relevant quarks or from deep inelastic neutrino scattering [14]. The matrix elements $|\mathrm{V_{tq}}|$ can be determined from unitarity bounds. The measured magnitudes of the matrix elements are currently [14] :

$$\begin{pmatrix} |\mathrm{V_{ud}}| & |\mathrm{V_{us}}| & |\mathrm{V_{ub}}| \\ |\mathrm{V_{cd}}| & |\mathrm{V_{cs}}| & |\mathrm{V_{cb}}| \\ |\mathrm{V_{td}}| & |\mathrm{V_{ts}}| & |\mathrm{V_{tb}}| \end{pmatrix} = \begin{pmatrix} 0.9745 \rightarrow 0.9757 & 0.219 \rightarrow 0.224 & 0.002 \rightarrow 0.005 \\ 0.218 \rightarrow 0.224 & 0.9736 \rightarrow 0.9750 & 0.036 \rightarrow 0.046 \\ 0.004 \rightarrow 0.014 & 0.034 \rightarrow 0.046 & 0.9989 \rightarrow 0.9993 \end{pmatrix},$$

where the range quoted is for the 90% confidence level. These values show the dominant quark decay scheme is t $\rightarrow$ b $\rightarrow$ c $\rightarrow$ s $\rightarrow$ u.

1.2 b Quark Physics

Quark pair events ($\mathrm{e^+ + e^- \rightarrow q + \overline{q}}$) are the most common $\mathrm{Z^0}$ mediated decays. The QCD interaction ensures that the primary quark and anti-quark are not observed in isolation. Additional quarks and anti-quarks are produced spontaneously in a process called fragmentation and jets of hadrons are observed in the detector. The original quark and anti-quark become parts of two of the final hadrons. These events therefore contain a large number of tracks and have large amounts of energy deposited in the calorimeters. Because of the large number of hadrons in the final state they are called 'multihadronic' events. b quarks are the heaviest quarks produced at LEP and are of particular interest as it is possible to employ tagging methods to separate these events from other multihadronic events.

When a b quark decays semi-leptonically, e.g. $\mathrm{b}\to\mathrm{c}\ell^-\overline{\nu}_\ell$, the charged leptons tend to have large momentum and are therefore easy to identify amongst the other particles in the event. Another feature of b hadrons is their relatively long lifetime ($\sim$ 1.5ps) when compared to light flavoured hadrons which allows tagging via secondary decay vertices displaced from the primary vertex. A measure of how well a track fits to a vertex can be obtained by looking at the impact parameter of the track with respect to the two vertices (The impact parameter is the distance between the vertex and the point of closest approach of the track to that vertex). In some analyses the secondary vertex is not reconstructed and just the impact parameter with respect to the primary vertex is used as a tag for b hadrons.

Many different types of analysis are being carried out in the b-quark area and a some of these are now briefly described:

1.2.1 Electroweak Measurements using $\mathrm{Z}^0 \to \mathrm{b}\overline{\mathrm{b}}$ Events

The partial decay width of the Z^0 to $\mathrm{b}\overline{\mathrm{b}}$, $\Gamma_{b\overline{b}}$ is of interest because the $\mathrm{Z}^0\mathrm{b}\overline{\mathrm{b}}$ vertex corrections differ from those for other quarks and leptons as it has a different dependence on the top mass from those of the other quarks. It is also possible that new physics beyond the standard model might first be seen in $\Gamma_{b\overline{b}}$ because new couplings to massive particles might affect this vertex more than others. Measurements are made of the fraction of hadronic events at the Z^0 peak which contain primary $\mathrm{b}\overline{\mathrm{b}}$ pairs and this can be related to the quantity

$$R_b \equiv \frac{\Gamma(\mathrm{Z}^0 \to \mathrm{b}\overline{\mathrm{b}})}{\Gamma(\mathrm{Z}^0 \to \mathrm{hadrons})} \tag{1.7}$$

R_b has in the past been measured as being anomalously low when compared to the standard model, however more recent measurements now give a value consistent with the standard model [15].

The differential cross-section for the production of fermion-antifermion pairs in e^+e^- annihilation can be expressed as

$$\frac{\mathrm{d}\sigma}{\mathrm{d}\cos\theta} \propto 1 + \cos^2\theta + \frac{8}{3}A_{\mathrm{FB}}\cos\theta \tag{1.8}$$

where A_{FB} is the forward-backward asymmetry and is related to the weak mixing angle $\sin^2\theta_{\mathrm{W}}$. The weak mixing angle is important in electro-weak theory for giving the relative strengths of the electromagnetic and weak forces (see section 1.1.5). As it is easy to separate b events from other quark events it is possible to measure the asymmetry, $A_{\mathrm{FB}}^{\mathrm{b}}$, for b quarks.

1.2.2 Mixing and Lifetime

If a B^0 meson is formed then an electroweak process called mixing may occur. In the mixing process b quarks can become $\overline{\mathrm{b}}$ quarks before the meson decays. This process occurs due to box diagrams as shown in figure 1.3.

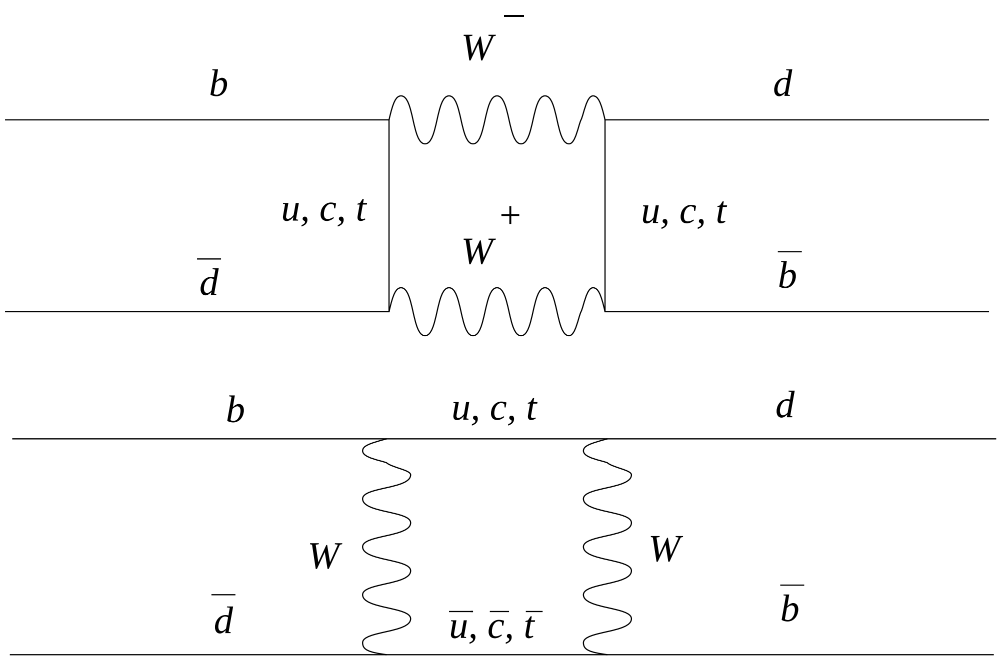

Figure 1.3: Mixing Diagrams.

The mixing probability $P(t)$ has a time dependence

$$P(t) \propto (1 - \cos(\Delta M t)) \tag{1.9}$$

where ΔM is the difference in mass between the mass eigenstates [67]. Measurements are now being made of this time dependent mixing and of the time averaged mixing given by

$$\chi_q = \int_0^\infty P_q(t)dt \tag{1.10}$$

If both $\mathrm{B_d^0}$ and $\mathrm{B_s^0}$ are produced then the measured χ will be given by

$$\chi = f_d \frac{B_d}{\langle B \rangle} \chi_d + f_s \frac{B_s}{\langle B \rangle} \chi_s \tag{1.11}$$

where f_d and f_s are the fractions of b hadrons that are produced as $\mathrm{B_d^0}$ and $\mathrm{B_s^0}$ mesons respectively, and B_d, B_s, and $\langle B \rangle$ are branching fractions for $\mathrm{B_d^0}$, $\mathrm{B_s^0}$, and the b-hadron admixture respectively decaying to the observed mode. Since the amount of mixing involves the strength of the coupling of the top quark to the quarks in the B meson the measurement of mixing is important for the determination of the elements of the Kobayashi–Maskawa matrix, V_{td} ($\mathrm{B_d^0}$–$\mathrm{\overline{B}_d^0}$ mixing) and V_{ts} ($\mathrm{B_s^0}$–$\mathrm{\overline{B}_s^0}$ mixing). The measurement of χ is used to correct measurements of A_{FB} and also to determine the value of f_s since the value of χ_s is known to good precision. A measurement of time averaged mixing is presented in Chapter 4.

The branching ratios $\mathrm{b \rightarrow c}$ and $\mathrm{b \rightarrow u}$ are used in the determination of the Kobayashi–Maskawa matrix elements V_{cb} and V_{ub} respectively. Measurements of b hadron lifetimes can also be used in calculations of these Kobayashi–Maskawa matrix elements.

1.2.3 Spectroscopy

The production of the orbitally excited B mesons $\mathrm{B^{**}}$ and $\mathrm{B_s^{**}}$ is of interest since their expected decay modes $\mathrm{B^{**} \rightarrow B^{(*)}}\pi$ and $\mathrm{B_s^{**} \rightarrow B^{(*)}K}$ would allow the matter/anti-matter nature of the produced B meson to be identified from the charge of the π or K. This could be useful for several analyses including B-$\mathrm{\overline{B}}$ mixing and searches for CP violation.

It is also interesting to measure the mass and width of the resonances as these have been predicted by heavy quark effective theory (HQET) [16]. If a hadron contains a heavy quark, Q, QCD shows more symmetries as the heavy quark mass becomes large when compared to a typical QCD scale(e.g. the spin of the heavy quark and the total angular momentum of the light quark are separately conserved). These symmetries allow the spectrum and decays of heavy-light ($Q\overline{q}$) mesons to be predicted. Since $m_b \gg \Lambda_{\mathrm{QCD}}$, heavy quark symmetry should provide a good description of the B and $\mathrm{B_s}$ mesons. The properties of D and even K mesons should also show approximate heavy-quark symmetry. From these symmetries predictions have been made for the masses and widths of the the narrow S-wave $\mathrm{B^{**}}$ and $\mathrm{B_s^{**}}$ resonances using as inputs the measured masses of B,D and K mesons [16], these predictions are shown in table 1.2. For both $\mathrm{B^{**}}$ and $\mathrm{B_s^{**}}$ one of the resonances is predicted to decay either to a $\mathrm{B^*}$ or to a B.

Transition	Width (MeV)
$\mathrm{B^{**}}$	
$\mathrm{B_2^*(5771)} \rightarrow \mathrm{B^*}\pi$	11
$\mathrm{B_2^*(5771)} \rightarrow \mathrm{B}\pi$	11
$\mathrm{B_1(5759)} \rightarrow \mathrm{B^*}\pi$	17
$\mathrm{B_s^{**}}$	
$\mathrm{B_{s2}^*(5861)} \rightarrow \mathrm{B^*K}$	~ 1
$\mathrm{B_{s2}^*(5861)} \rightarrow \mathrm{BK}$	2.6
$\mathrm{B_{s1}(5849)} \rightarrow \mathrm{B^*K}$	~ 1

Table 1.2: HQET predictions for $\mathrm{B^{**}}$ and $\mathrm{B_s^{**}}$.

Chapter 2

The Accelerator and Detector

The LEP accelerator was constructed to make a detailed study of the electro-weak interaction. In this thesis $e^+e^- \rightarrow Z^0 \rightarrow b\overline{b}$ events recorded by the OPAL detector are studied.

2.1 The LEP Collider

The Large Electron Positron facility [18] lies in a (roughly) circular tunnel with a circumference of 26.7 km at an average depth of 100m below the French-Swiss border near Geneva. Bunches of electrons and positrons circulate in opposite directions and are made to collide at the four interaction points, where the detectors, ALEPH [19], DELPHI [20], L3 [21] and OPAL [22] have been constructed. The collisions occur at centre of mass energies between 80 and 183 GeV. LEP running has been separated into two main periods known as LEP1 and LEP2. At LEP1 the centre of mass energy was kept at a value suitable to produce Z^0 bosons and at LEP2 the energy has been raised to enable the first production of W^+W^- pairs. There was also a short period called LEP1.5 when the centre of mass energy was at intermediate values. This allowed testing of the equipment for LEP2 and also provided the opportunity to search for new particles.

2.1.1 The Injection System

The injection system used to introduce electrons and positrons into the main LEP ring is shown in figure 2.1. Electrons are stripped from a heated filament and accelerated in the

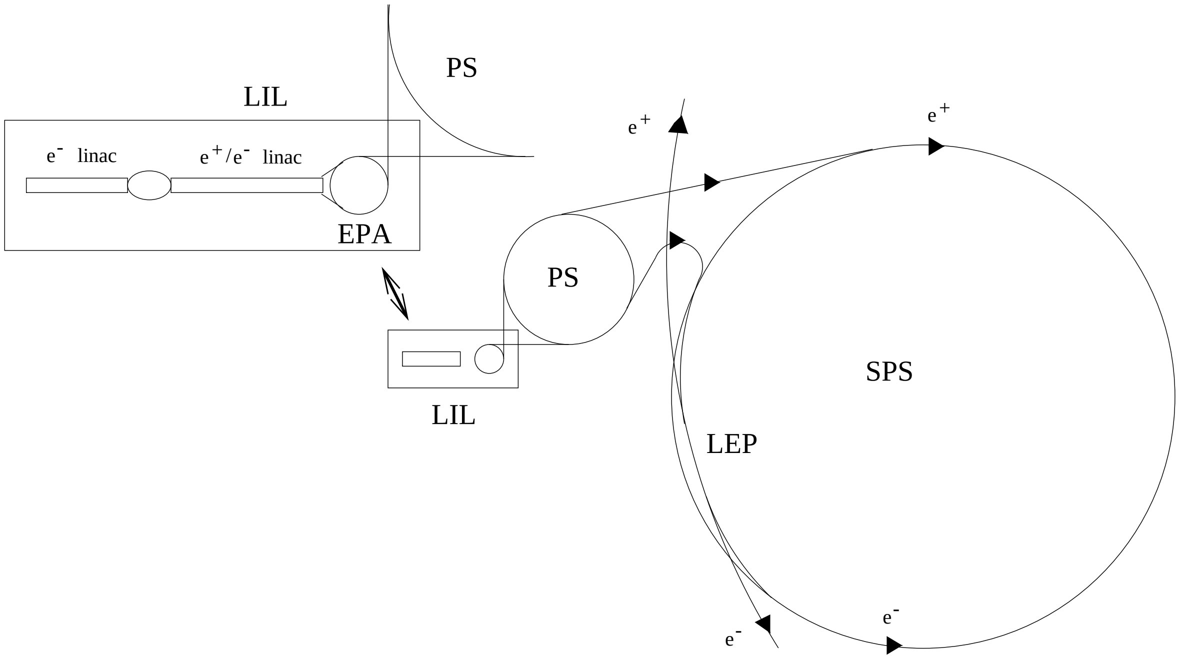

Figure 2.1: Schematic of the LEP injection and Acceleration system.

LEP Injector Linac (LIL) to 200 MeV and are directed into a tungsten target. e^+e^-pairs are produced by bremsstrahlung photons emitted during the rapid deceleration of the electrons. The positrons are then separated using a magnetic field, and the resulting positrons and electrons are accelerated to 600 MeV in the second part of LIL and stored in the Electron Positron Accumulator (EPA) ring. This ring stores the particles until a sufficiently large number of $e^-$and e^+have been accumulated to be injected into the 200m circumference Proton Synchrotron (PS) for acceleration to 3.5 GeV. The particles are then transfered into the 2.2 km circumference Super Proton Synchrotron (SPS) where they are accelerated to 20 GeV. These beams are then extracted from the SPS and injected into LEP. The use of the SPS complex to provide electrons and positrons for LEP does not interfere with the fixed target programs also fed by the SPS as it takes advantage of the dead-time in the pulsed proton cycle.

2.1.2 The Accelerating System

As the electrons and positrons travel in a (roughly) circular orbit they are under (almost) constant centripetal acceleration. An accelerated charge emits synchrotron radiation, the energy loss per revolution is given by equation 2.1.

$$\Delta E = \frac{4\pi}{3}\frac{e^2\beta^3\gamma^4}{R} \tag{2.1}$$

where R is the radius of the ring, β is the particle velocity as a fraction of the speed of light, and $\gamma = (1-\beta^2)^{-1/2}$. At a nominal energy of 46 GeV an electron loses approximately 180 MeV for each revolution of LEP so with the order of 10^{11} particles per bunch the energy losses are very large. This energy is replaced by radio frequency (RF) cavities.

Originally LEP was fitted with 128 copper RF cavities installed in the straight sections of the LEP ring and powered by 16 1–MW klystrons. More recently (for LEP2) super conducting cavities have been installed and used.

For the beams to continue circulating for long periods of time they are transported inside an evacuated beam pipe, in order to reduce the number of gas molecules with which the electrons and positrons can collide. The pressure inside the beam pipe is less than 3×10^{-9} torr. To keep the particles travelling in the circular orbit there are over 3000 bending (dipole) magnets and almost 2000 focusing (quadrupole, sextupole and octupole) magnets.

2.2 The OPAL Detector

The OPAL (Omni Purpose Apparatus for Lep) detector is designed to reconstruct and identify all known final state particles produced in e^+e^-collisions (except for $\nu\overline{\nu}$ final states), covering as much of the angular acceptance around the interaction point as possible. A perspective view and a cross-section of the OPAL detector are shown in figures 2.2 and 2.3. The co-ordinate system at OPAL is the standard right handed

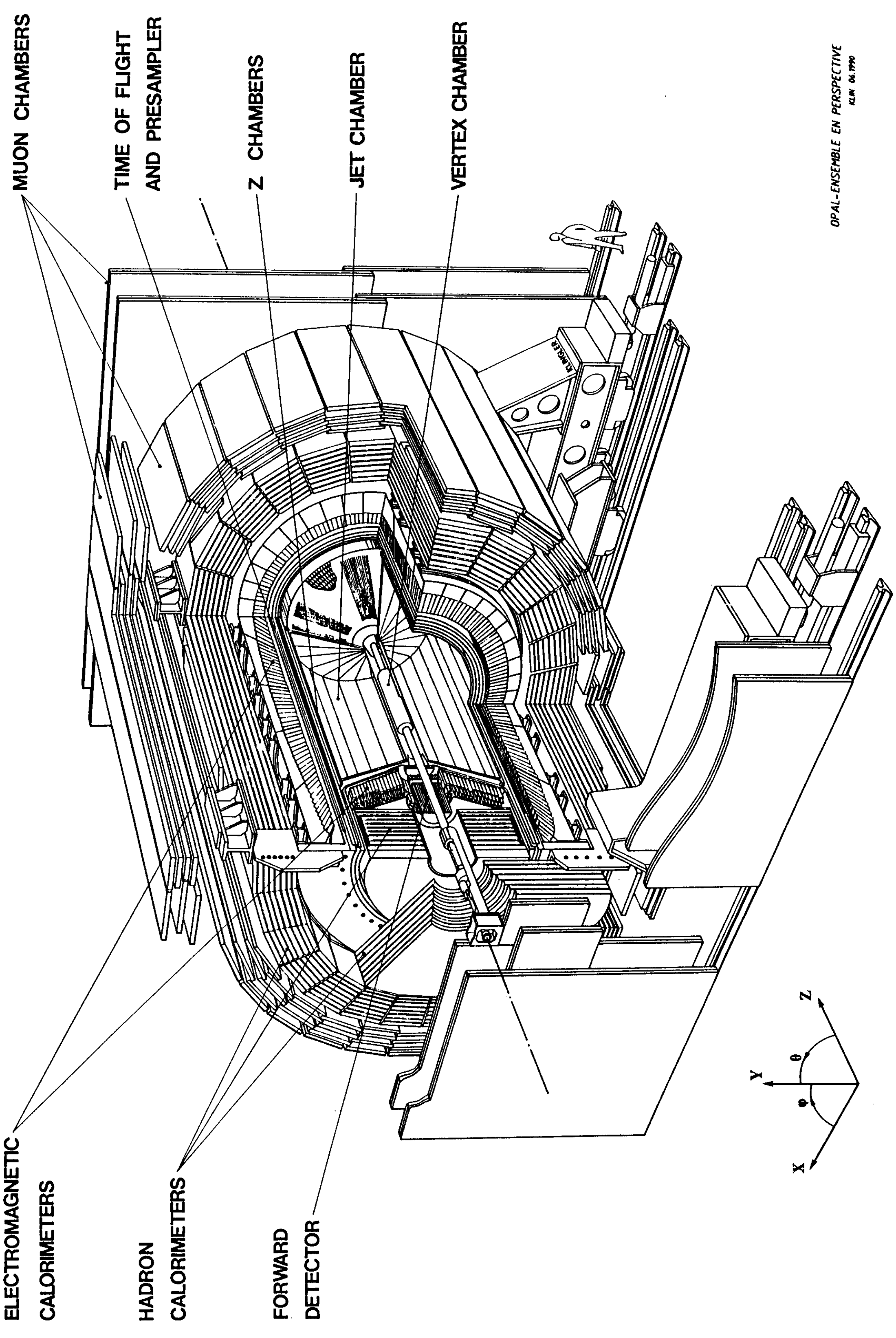

Figure 2.2: A perspective view of the OPAL detector.

a)

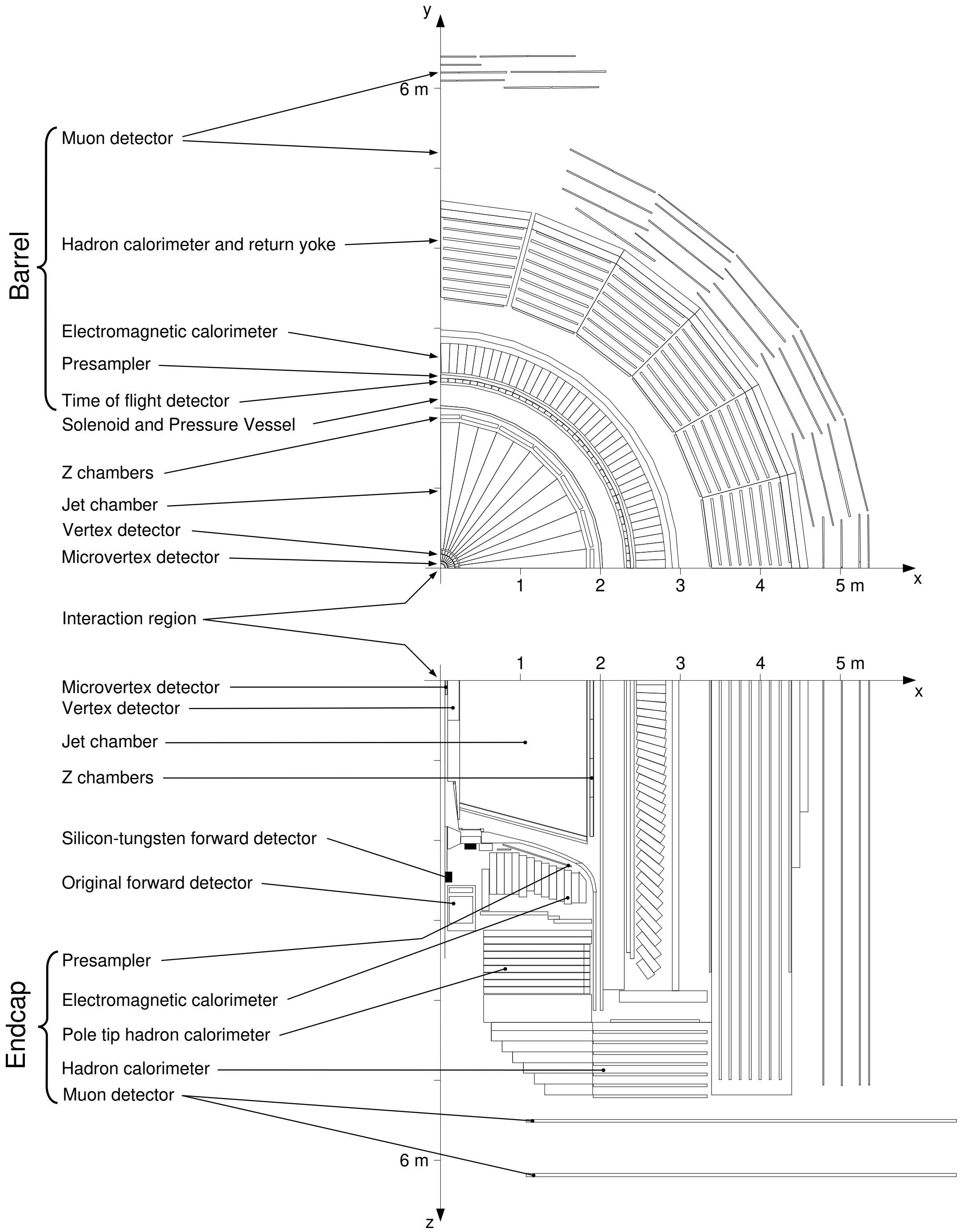

b)

Figure 2.3: Cross section of the OPAL detector a) Front view b) Top view.

Cartesian system, the origin of which is defined by the centre of the jet chamber (section 2.2.1.3). The z axis is defined in the direction of the electron beam through OPAL, the x axis points towards the centre of the LEP ring, and the y axis is therefore almost vertical (since LEP is slightly tilted). Also used are spherical polar co-ordinates (r, ϕ, θ) the angle of azimuth, ϕ, is measured about the z axis with the positive x axis defining $\phi = 0$. The polar angle, θ, is measured from the positive z axis, and the distance from the origin is denoted by r.

The detector consists of a set of concentric cylindrical subdetectors, centred on the interaction point, and closed off at the ends by the endcap detectors. Near the beam pipe are the vertex detectors which help to detect short lived particles that decay close to the primary vertex. Around these are the tracking chambers that measure the trajectory of charged particles via ionisation of a gas. A magnetic field is used to bend the charged particles so that their momenta can be measured from the track curvature. Next come the calorimeters, designed to absorb and measure the energy of charged and neutral particles. Firstly the electromagnetic calorimeter which is designed to absorb and measure the energy of photons and electrons via electromagnetic showering. This is followed by the hadron calorimeter which is designed to stop everything that passes through the electromagnetic calorimeter except muons and neutrinos. The outer layer of the detector comprises muon chambers where muons are detected.

2.2.1 The Central Detector

The central detector consists of a silicon microvertex detector and three drift chambers. The drift chambers (vertex detector, jet chamber and z chambers) are located inside a pressure vessel containing a gas mixture[a] at a pressure of 4 bar. The central detector is inside a solenoid supplying a uniform axial magnetic field of 0.435 T.

2.2.1.1 The Silicon Microvertex Detector (SI)

The silicon microvertex detector [23] has gone through several incarnations. First installed in 1991 it had two layers of single sided Silicon Microstrip Detectors at radii

[a] 88.2% argon, 9.8% methane, 2.0% isobutane

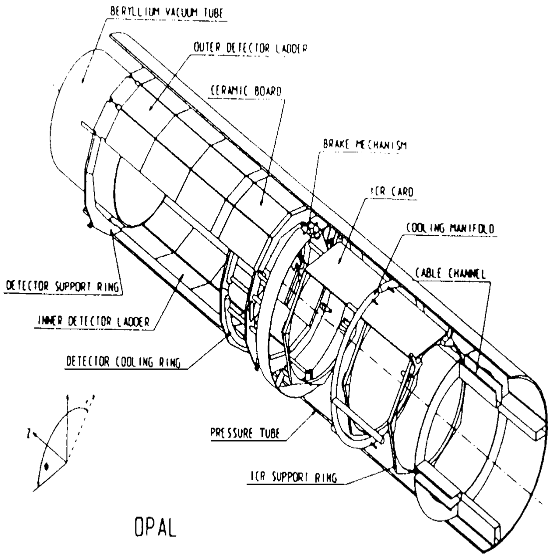

Figure 2.4: A cut-away view of the silicon microvertex detector *in situ* around the beryllium beam pipe. The silicon wafers are visible toward the top of the picture, and the read-out electronics are towards the bottom.

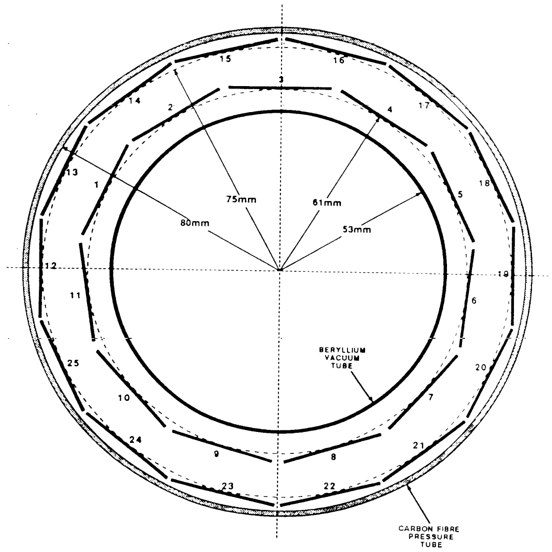

Figure 2.5: A view along the beam direction of the orientation of the silicon wafers in the microvertex detector. The beryllium beam pipe and the carbon fibre pressure tube are shown.

of 6 and 7.5 cm. The inner layer consisted of 11 ladders and the outer 14. Each ladder was 18cm long. Readout was in $r-\phi$ only. In 1993 it was upgraded and had $r-\phi$ and $r-z$ wafers glued back to back. For 1995 the number of ladders was increased to 12 and 15 in the inner and outer layers respectively and the ladders were tilted to close small gaps in ϕ. The spatial resolution of this detector is $5-10$ μm. The separation between the two concentric layers allows the two dimensional reconstruction of secondary decay vertices. This enables the lifetimes of short lived particles (τ, hadrons containing b or c quarks) to be measured and heavy quark (b or c) events to be tagged using an impact parameter or decay length technique. Figures 2.4 and figure 2.5 show the overall layout of the original (1991) microvertex detector and a view along the beam direction showing the orientation of the silicon detectors, respectively. The z coordinate is not used in the analyses presented in this thesis.

2.2.1.2 The Vertex Detector (CV)

The vertex detector [24] is 1m long and 470mm in diameter and consists of two concentric cylindrical layers of 36 sectors each. Each sector is defined by planes of cathode wires with a 1 mm radial spacing. The ionisation electrons are detected by an anode wire plane at the centre of the sector. The anode wires are alternated with potential wires which shape the electric field, producing a drift field of 2.5 kV cm^{-1} within a sector. The anode wires are staggered to resolve left-right ambiguities. In each sector the inner layer has a plane of 12 anode wires parallel to the beam axis (*axial wires*) while each sector in the outer layer has a plane of 6 anode wires at an angle of 4 degrees to the beam axis (*stereo wires*).

Axial and stereo wire coverage is provided over the angular range $|\cos\theta| < 0.92$ and axial wire only coverage is provided for $|\cos\theta| < 0.95$. The axial wires supply very good $r-\phi$ resolution while combining the axial and stereo information gives an accurate z resolution. The detector achieves a precision of 55 μm in $r-\phi$ and 700 μm in $r-z$.

2.2.1.3 The Jet Chamber (CJ)

The jet chamber [25] is a large multiwire drift chamber of length 400 cm at an outer radius of 185 cm and has an inner radius of 25cm. The end planes of the chamber are conical. The chamber consists of 24 identical sectors each containing a plane of 159 staggered (to resolve left right ambiguities) anode wires with a radial separation of 10 mm, alternated with potential wires. Cathode wires form the boundary between sectors. All wires are parallel to the beam axis. The drift field in each sector is maintained at 890 V cm^{-1}.

All 159 space-points are measured over the range $|\cos\theta| < 0.73$ and at least 8 points are measured over 98% of the entire solid angle. The drift time for electrons created by the passage of charged particles is used to measure the position in $r-\phi$ and gives a resolution of 135 μm. The amount of charge collected at each end of the wire is used to give a rough z coordinate (with a resolution of $\approx$ 6 cm).

Particle identification is performed through the dE/dx measurement derived from the measured charge collected at each wire. Tracks with at least 130 measured points yield dE/dx resolutions of $\pm 3.8\%$ for minimum ionising pions in multihadronic events. Figure 2.6 shows the dE/dx value plotted as a function of the charged particle momentum for a variety of particle types.

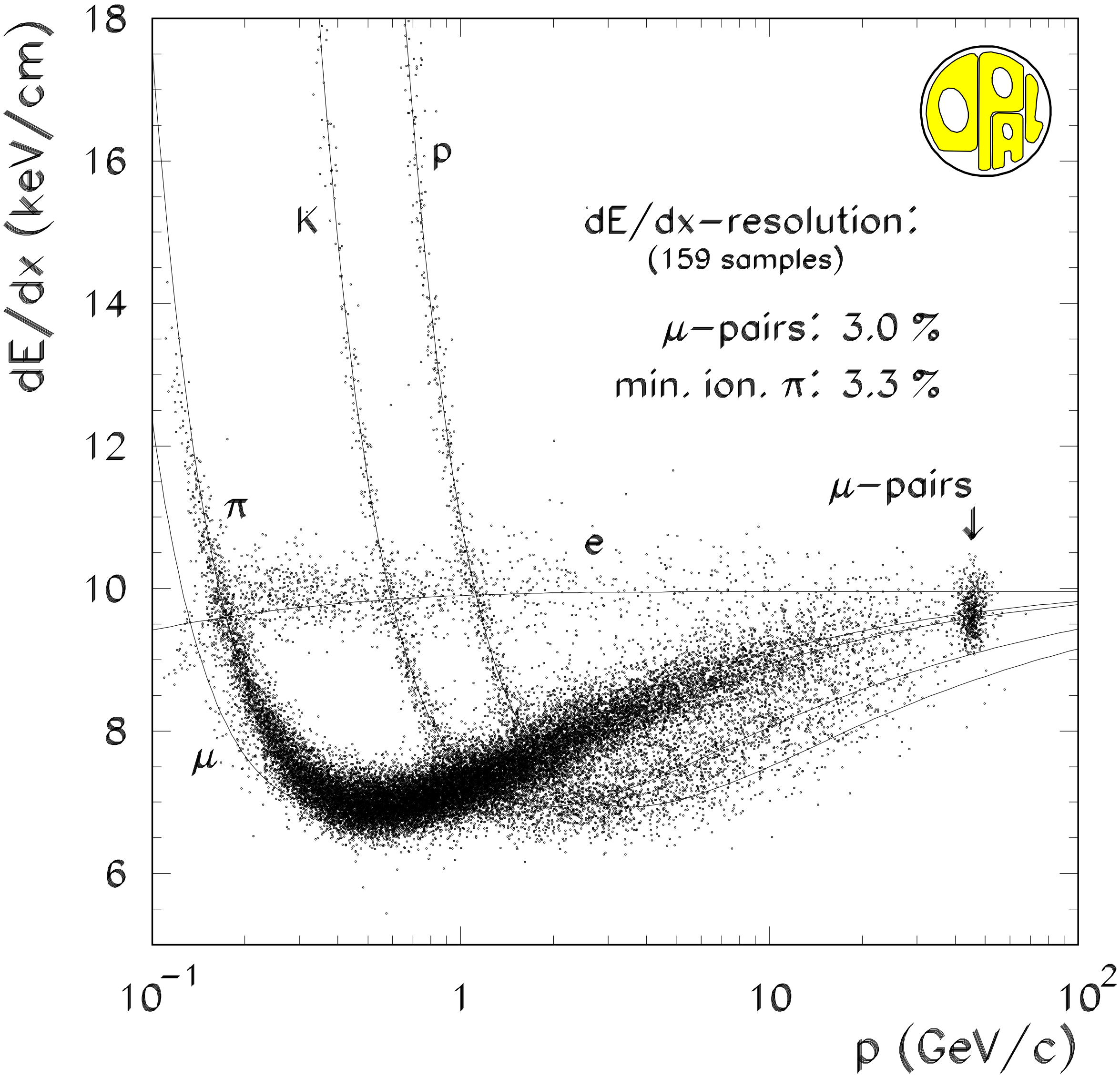

Figure 2.6: The measured and expected dE/dx for multihadronic tracks and muon pairs as a function of particle momentum.

2.2.1.4 The Z Chambers (CZ)

The z-chambers [26] are 24 drift chambers 400 cm long, 50cm wide and 5.9cm thick, divided into eight units. A polar range of $|\cos\theta| < 0.95$ is covered along with 94% of ϕ. Each unit has six staggered anode wires at right-angles to the beam axis. The z coordinate is measured with a resolution of around 300μm, and the charge division is used to give ϕ with a resolution in $r-\phi$ of 15mm.

2.2.2 The Magnet

The OPAL magnet is a conventional water-cooled solenoid inside an iron yoke, which doubles as showering material for the hadron calorimeter. A current of 7000 A is used to produce a uniform field of 0.435 T throughout the central detector. Less than 5 MW of power is consumed. The coil was wound as one unit to ensure low residual fields outside the solenoid in order to protect sensitive electronics.

2.2.3 The Time of Flight System (TOF)

The time of flight system measures the time-of-flight of particles from the interaction point. It consists of 160 scintillation counters forming a barrel layer 684 cm long at a mean radius of 236 cm. The information is used for triggering, to aid in the identification of low-momentum charged particles and to help in cosmic ray rejection.

2.2.4 The Electromagnetic Detector

The electromagnetic calorimeter is used to measure the energy and position of electrons and photons with energies in the range 100 MeV $\rightarrow$ 100 GeV. It also allows $\pi^0 - \gamma$ discrimination and, together with the central tracking system, electron–hadron discrimination. 98 % of the solid angle is covered by a barrel and two endcap sections. The detector consists of a presampler followed by a lead-glass calorimeter.

2.2.4.1 The Electromagnetic Presampler (PB,PE)

The presence of $\sim$2 radiation lengths in front of the calorimeter means that most electromagnetic showers start before reaching the lead glass blocks. Therefore the presampler is needed to measure the position and energies of these showers in order to improve overall spatial and energy resolution. The presampler in the barrel (PB) [27] consists of two layers of streamer tubes while the endcap presampler (PE) [28] is a multiwire proportional device mounted between the pressure bell and the endcap lead glass.

2.2.4.2 The Electromagnetic Calorimeter (ECAL)

The barrel calorimeter (EB) is made up of 9440 lead glass blocks arranged in a cylindrical array with each block pointing at the interaction point. These cover the angular range $|\cos\theta| < 0.82$. The endcap calorimeter (EE) [29] is similarly made of 1132 lead glass blocks arranged in two dome shaped arrays extending the range up to $|\cos\theta| = 0.98$. The Čerenkov light produced in the lead glass blocks is measured by photo-multipliers in the barrel and by vacuum photo-triodes in the endcap. Both the endcap and the barrel contain about 24 radiation lengths of material effectively giving complete absorption of electrons and photons. The ECAL gives an intrinsic energy resolution of $\sigma_E/E \simeq 15\%/\sqrt{E}$ in the barrel and $\sigma_E/E \simeq 20\%/\sqrt{E}$ in the endcap [30].

2.2.5 The Hadron Calorimeter (HCAL)

The hadron calorimeter measures the energy of hadrons that exit the electromagnetic calorimeter and also helps with muon identification. This detector is divided into a cylindrical barrel, two endcaps and two pole tips. The barrel and endcap are based on the same design [31] with the return yolk iron segmented such that the spacing between the 10 cm thick iron slabs is $\approx$ 30mm in both cases. The detectors placed in these spaces are limited streamer tubes. The barrel has 9 layers of detector and eight 10 cm thick slabs of absorber covering the region $|\cos\theta| < 0.81$. In the endcaps there are 8 layers of detector and 7 layers of absorber covering the region $0.81 < |\cos\theta| < 0.91$. The hadron pole-tips [32] cover the range $0.91 < |\cos\theta| < 0.99$. They consist of 10 layers of very thin proportional chambers situated in the magnet pole-tips.

2.2.6 The Muon Detector

After the hadron calorimeter only the very penetrating muon is expected to be detectable, for this the muon barrel and endcap detectors are used.

2.2.6.1 The Muon Barrel (MB)

The muon barrel [33] covers the range $|\cos\theta| < 0.72$ and is made up of 110 drift chambers, each 1.2 m wide, 90 mm thick and up to 10.4 m long (some are shorter to allow room for the magnet's support structures). They are arranged to form four layers. The $r - \phi$ measurement is obtained from the drift time to an accuracy of 1.5 mm. A z measurement is achieved from a system of diamond shaped cathode pads opposite the anode wires which give a resolution of around 1.5 mm.

2.2.6.2 The Muon Endcap (ME)

The muon endcaps [34] each consist of four 'quadrant' chambers each roughly 6 m by 6 m and two 'patch' chambers that are 3 m by 2.5 m arranged as shown in figure 2.7. The endcaps cover an angular range of $0.67 < |\cos\theta| < 0.985$.

Each chamber is made from two double layers of streamer-tubes, 67 cm apart (in z). The chambers are read out using strips both parallel and perpendicular to the streamer tubes. The position resolution obtained is approximately 1 mm for perpendicular strips and 3 mm for parallel strips.

2.2.7 The Forward Detector (FD) and SiW Luminometer (SW)

The forward detectors are situated at $|z| \simeq 2.6$ m covering very small angles to the beam (40 mrad to 200 mrad). Each contains an electromagnetic calorimeter, drift chambers [35] for tracking, and scintillator, allowing a measurement of the luminosity from Bhabha scattering to a precision of 0.6%.

In 1993 a silicon-tungsten luminometer [36] made of 19 layers of silicon interspersed

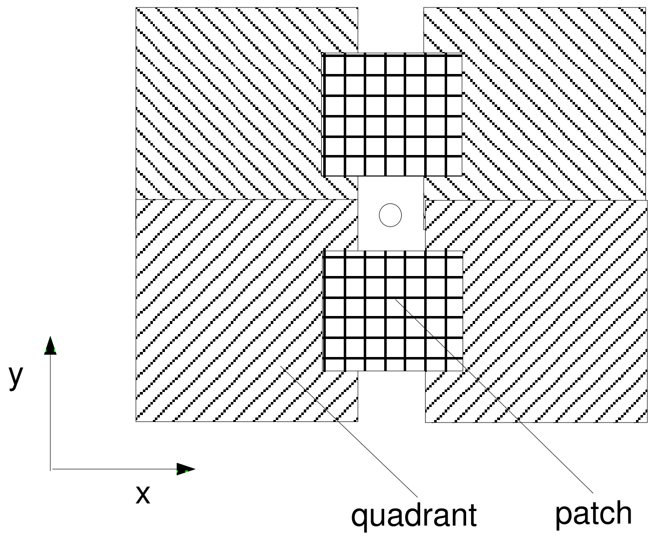

Figure 2.7: End view of the muon endcap detector.

with 18 layers of tungsten was installed and has been used to measure luminosity to a level of 0.1% [37].

2.2.8 The OPAL Trigger System

The digitisation of a physics event requires roughly 20 ms which when compared to the time between bunch crossings of 22 μs (with 4 bunches in LEP) is obviously too long, so some faster method of discriminating between real physics and background signals must be employed.

In order to reduce the data volume to an acceptable level whilst retaining maximum efficiency for triggering on e^-e^+ events, each contributing subdetector sends two kinds of signal to the central triggering system [38]. Firstly there are stand-alone triggers, such as energy sums and hit counts, and secondly the solid angle of the detector is divided up into 6 θ and 24 ϕ bins, with each subdetector supplying inputs to this matrix. The matrix is then checked for correlations between subdetectors in these regions. The $\theta - \phi$ matrix is then combined with the stand-alone triggers to form an overall trigger decision. If no event is to be digitised then the whole detector is reset ready for the next bunch crossing.

2.2.9 The Data Acquisition System

If an event passes the criteria of the trigger then an event number is sent to each subdetector. The subdetector is then read out into the local system crate(s) (LSC – a VME crate) where it is processed to reformat it and reduce the data size. The data is then passed to another VME crate, called the event builder. This crate takes all the information from the subdetectors and using the event numbers puts together a complete set of data for an event, before passing it to the filter.

The filter does a fast analysis of the event using calorimeter, TOF, muon chamber and reconstructed jet chamber information. This is used to classify the event and to reject obvious background events. The data is also compressed into a form called dense data (DD) which is saved to optical disks. The filter is also used for monitoring the output, particularly in the form of event displays.

Finally the data is processed by the OPAL reconstruction package, known as ROPE (Reconstruction of OPal Events) [39]. The input data for ROPE is produced either by the OPAL detector itself or by the OPAL simulation package GOPAL [40] (see section 2.2.10). The Rope code produces a summary of calculated quantities such as energy clusters in the calorimetry or reconstructed track momenta using the data from all subdetectors. This is written to the data summary tapes (DST's), and is available for physics analysis.

2.2.10 Simulation of the OPAL Detector

The OPAL Monte Carlo simulation program is known as GOPAL (Geant at OPAL) [40]. The detector is modelled using the GEANT package [41], using as inputs the geometries and densities of the various OPAL constituents. Particles generated by Monte Carlo event generators such as JETSET [42], HERWIG [43], KORALZ [44] and TAUOLA [45] are tracked through this material. Hits are recorded when they would have interacted with the detector material. The signals are then modelled to more accurately reflect the performance of the detector by adding noise, inefficiency and resolution effects. This data is reconstructed in the same way as genuine data, however the DST's have stored in them an extra bank carrying the true Monte Carlo information which can then be used later to 'cheat' and check the efficiency and purity of the analysis.

2.2.11 JETSET

In the analyses that follow Monte Carlo events have been used that have been generated with the JETSET program which has been tuned by OPAL to fit observations as well as possible. The tuning involves adjusting for example the probability for various decay chains to occur and also in the case of charm and bottom quarks the fragmentation parameters are adjusted. Fragmentation is the process by which colour confinement causes quark anti-quark pairs to be produced as well as the two original quarks produced via the decay of the Z^0. The tuned parameters control event properties including how much of the momentum is carried by the various hadrons that are eventually observed after the fragmentation process.

The Monte Carlo samples used in this thesis are detailed in table 2.1. Jetset 7.3

OPAL Name	Type	N_{events}	JETSET Version
R2218,R2291,R2292	udscb	3×10^6	7.3
R2790–R2793	udscb	4×10^6	7.4
R2776	$b\overline{b}$	1×10^6	7.4

Table 2.1: The specification of the Monte Carlo samples used.

is described in [48] and the parameters adjusted by the OPAL tune are described in [49]. A later version of the generator Jetset 7.4 and the corresponding OPAL tune are described in [50] and [51].

Chapter 3

Identifying $Z^0 \rightarrow b\overline{b}$ Events

Multihadronic ($Z^0 \rightarrow q\overline{q}$) events found in the OPAL detector have a characteristic shape consisting of two or more jets of particles, One such event is shown in figure 3.1. These events are selected online by the trigger and filter as discussed in section 2.2.9. Events are then subjected to a multihadronic selection and the charged tracks and electromagnetic clusters are combined into jets using jet finding algorithms. The primary vertex is then reconstructed and the tracks in each jet searched for secondary vertices. The presence of a secondary vertex indicates the presence of a long-lived bottom or charmed hadron. Properties of these secondary vertices are examined to measure the probability that it is the decay of a bottom hadron.

3.1 The Trigger and Filter Selection

The most important parts of the trigger used to select multihadronic events are :

The Track Trigger : At least two tracks are required to originate from the nominal event vertex, each with a transverse momentum of at least 0.45 GeV.

The Time-of-Flight Trigger : At least three non-adjacent scintillator counters must have registered hits.

The Electromagnetic Trigger : The summed raw energy in either the barrel or endcaps must be at least 6 or 7 GeV respectively.

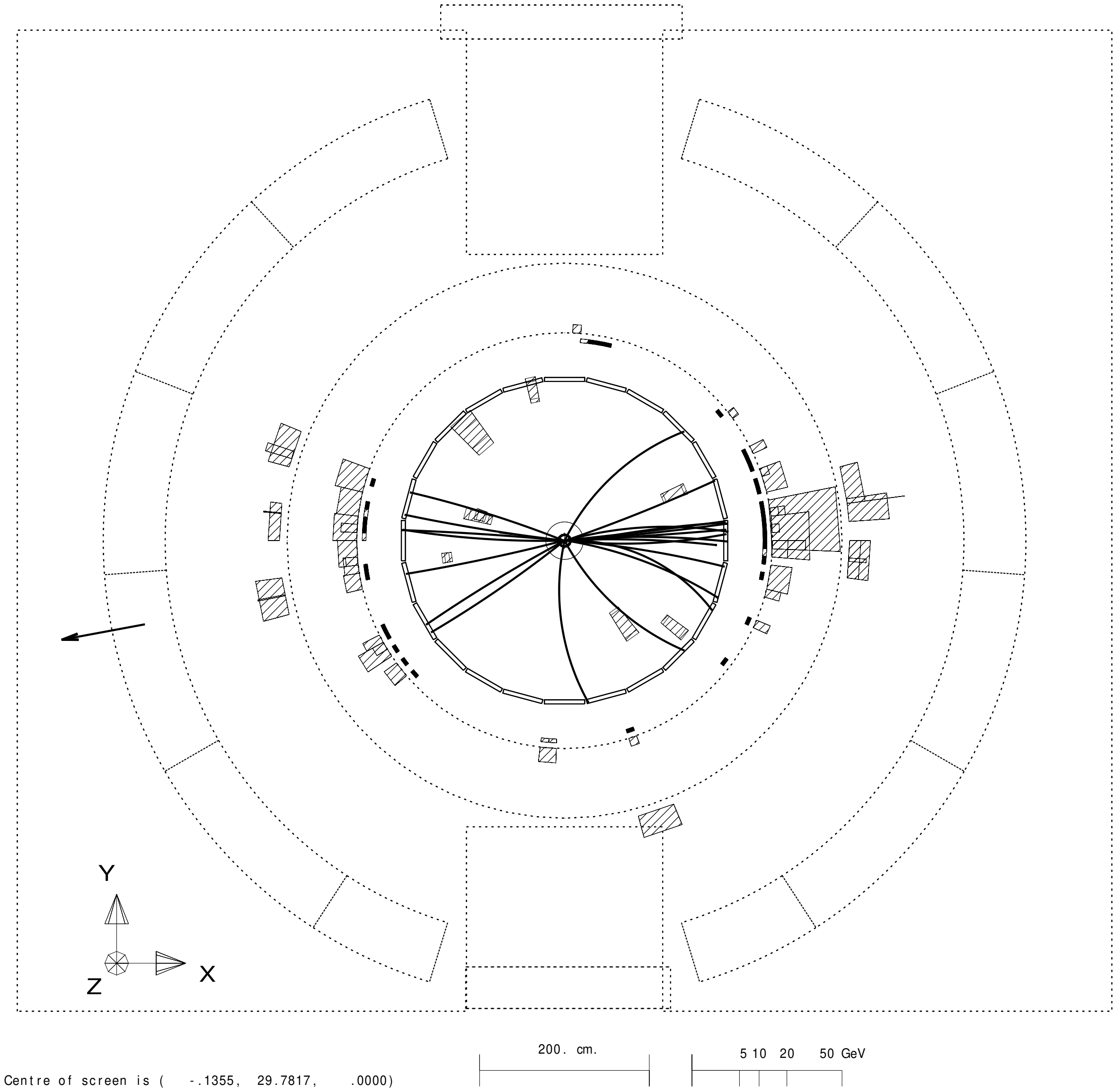

Figure 3.1: A typical $e^+e^- \rightarrow q\overline{q}$ event recorded with the OPAL detector, looking along the beam direction. Two jets of particles are clearly visible. The tracks are reconstructed in the central jet chamber, the inner (outer) layers of blocks represent energy deposited in the electromagnetic (hadronic) calorimeter. The arrow represents a muon recorded by the barrel muon detector.

A high level of redundancy is achieved due the high multiplicities of multihadronic events. The overall efficiency exceeds 99%.

The filter performs a preliminary classification based on the Gold Plated Multihadron Selection [54]. This uses only information from the electromagnetic calorimeters and the TOF. It is loose enough to maintain a high efficiency and not exclude possible new physics processes. Events with at least five tracks form the raw data-set for the analyses presented in this thesis. Table 3.1 shows the number of raw events for each year of data taking.

Year	Number of Events
1991	407720
1992	861458
1993	831422
1994	1890461
1995	831881

Table 3.1: The number of raw events for each year of OPAL data-taking used in this thesis.

3.2 The Multihadronic Selection

All tracks and electromagnetic clusters to be used in the selection need to satisfy the conditions show in tables 3.2 and 3.3.

Good Electromagnetic Clusters		
	Barrel	Endcap
Raw energy (E_{raw})	≥ 0.1 GeV	≥ 0.2 GeV
Number of blocks in cluster	≥ 1	≥ 2

Table 3.2: Quality conditions required by the multihadronic selection algorithm for electromagnetic clusters.

Good Charged Tracks	
Number of CJ hits	≥ 20
$\lvert \mathrm{d}_0 \rvert$	≤ 2.0 cm
$\lvert \mathrm{z}_0 \rvert$	≤ 40.0 cm
Radius of first hit	≤ 60.0 cm
Transverse momentum w.r.t. beam axis	≥ 0.05 GeV
$\lvert \cos\theta \rvert$	≤ 0.995

Table 3.3: Quality conditions required by the multihadronic selection algorithm for charged tracks. (d_0 is the distance from the average beamspot to the tracks point of closest approach to the beamspot and z_0 is the z coordinate when the track is at it's point of closest approach (p.c.a.) to the origin of coordinates.)

Using the good clusters two ratios, $\mathrm{R_{vis}}$ and $\mathrm{R_{bal}}$ are constructed:

$$\mathrm{R_{vis}} = \frac{\mathrm{E_{tot}}}{\sqrt{\mathrm{s}}}, \tag{3.1}$$

$$\mathrm{R_{bal}} = \frac{\mathrm{E_{bal}}}{\mathrm{E_{tot}}}, \tag{3.2}$$

where, $\mathrm{E_{tot}} = \sum \mathrm{E_{raw}}$ and $\mathrm{E_{bal}} = \sum \mathrm{E_{raw}} \cos\theta$[a]. The sums are over $\mathrm{N_{clus}}$ good clusters.

In order to pass this selection the event must satisfy:

- $\mathrm{N_{clus}} \geq 7$ good clusters,
- $\mathrm{N_{chgd}} \geq 5$ good tracks,
- $\mathrm{R_{vis}} \geq 0.10$,
- $\mathrm{R_{bal}} \leq 0.65$.

The multiplicity requirements ($\mathrm{N_{clus}}$, $\mathrm{N_{chgd}}$) are tuned to minimise the background from $\mathrm{Z^0}$ decays to charged lepton pairs. The $\mathrm{R_{vis}}$ (visible energy) requirement discards two-photon events. The $\mathrm{R_{bal}}$ (momentum imbalance) requirement rejects two-photon

[a] θ is the angle to the electron beam direction

events, interactions of the LEP beams with residual gas molecules (and beam pipe), and cosmic rays in the endcap detectors.

The selection has an efficiency of $\sim$ 98.4% [53] with reduced detector acceptance at small θ being the major source of inefficiency. The main backgrounds are from $\tau^+\tau^-$ and two-photon events, which have been estimated to form (0.11$\pm$0.03)% and (0.5$\pm$0.02)% of the final multihadronic sample respectively [53]. Background from interactions of the LEP beams with the beam pipe or residual gas molecules, cosmic rays, $\mu^+\mu^-$ or e^+e^- events have been determined to be negligible [53].

3.3 Additional Quality Requirements

Further selection criteria have been applied for the analyses presented in this thesis. The most important subdetectors for the selection of $Z^0 \rightarrow b\overline{b}$ events and the measurement of secondary vertices were required to be fully operational. These detectors are: CV, CJ, CZ, EB and EE.

Charged tracks used in the analyses were required to satisfy the following conditions:

- Minimum transverse momentum = 0.15 GeV/c,
- Maximum value of $|\tan(\lambda)|$[b] = 100,
- Maximum value of $|z_0|$ = 200 cm,
- Maximum momentum = 65 GeV/c,
- Minimum number of CJ hits = 20,
- Maximum value of $|d_0|$ = 5 cm,
- Maximum χ^2 from the x-y track fit = 100.

In addition electromagnetic clusters were required to satisfy :

[b] $\tan(\lambda) = \cot(\theta)$

- Minimum raw energy of cluster = 0.05 GeV,
- Minimum corrected energy of cluster in EB = 0.1 GeV,
- Minimum corrected energy of cluster in EE = 0.2 GeV.

All events were required to contain at least 7 good tracks and 7 good clusters.

3.4 Jet Finding

Two different algorithms are used in this thesis to group charged tracks and unassociated[c] electromagnetic clusters into jet-like topologies. The two algorithms are known as the 'JADE E0 scheme' and the 'cone jet finder'. The analysis in chapter 4 (a measurement of B mixing) uses the JADE jet-finder while the analysis in chapter 5 (measurement of the B^{**} and B_s^{**} mass peaks) uses the cone jet-finder.

3.4.1 The JADE Algorithm

This algorithm was first developed by the JADE collaboration [56] and is implemented at OPAL with the 'E0' recombination scheme [57]. A scaled mass :

$$\mathrm{y_{ij}} = \frac{2\mathrm{E_i E_j}\,(1-\cos\theta_{\mathrm{ij}})}{\mathrm{E_{vis}^2}} = \frac{\mathrm{M_{ij}^2}}{\mathrm{E_{vis}^2}}, \tag{3.3}$$

is used as the jet resolution parameter, where, $\mathrm{E_{vis}}$ is the total visible energy in the event and θ_{ij} is the angle between the pair of particles (i,j), of energy $\mathrm{E_i}$, $\mathrm{E_j}$, making an invariant mass, $\mathrm{M_{ij}}$, which is formed between between all possible particle pairs. The pair with the lowest invariant mass are combined to form a pseudo-particle and if $\mathrm{y_{ij}} < \mathrm{y_{cut}}$ the procedure is repeated until no pairs of pseudo-particles satisfy this requirement. A low value of $\mathrm{y_{cut}}$ will therefore result in a large number of very collimated jets, whereas a large value will eventually result in event being divided into two hemispheres.

[c] Tracks in the central detector are extrapolated from the last measured space-point to the electromagnetic calorimeter with multiple scattering in the intermediate material accounted for. If the track is within 150(50) mrad in θ and 80(50) mrad in ϕ for the barrel (endcaps) then the track is said to be associated with the cluster.

In bottom hadron analyses a quantity :

$$x_{\text{min}} = \text{y}_{\text{cut}}\,\text{E}^2_{\text{vis}}, \tag{3.4}$$

is often used rather than y_{cut} to ensure the minimum jet pair resolution is independent of the total visible energy in the event. In this thesis a value of $x_{\text{min}} = 49\,(\text{GeV})^2$ is used.

3.4.2 The Cone Algorithm

The cone jet finder was originally used at $\text{p}\overline{\text{p}}$ collider experiments [58] and more recently has also been used in e^+e^- collider experiments [59]. It has proved to be popular for bottom hadron physics due to its superior resolution of the jet axis direction vector, which is often used to estimate the b hadron direction.

The cone algorithm simply defines a jet as a set of particles that have a total energy greater than a cutoff ε and momentum vectors that lie within a cone of half angle R. The cone axis is described by the vectorial momentum sum of the particles. In this analysis R = 0.65 radians and ε= 5.0 GeV. The value of ε is scaled by the ratio $\text{E}_{\text{vis}}/\text{E}_{\text{cm}}$, where, E_{vis}, E_{cm} are the total visible energy in the event and the centre of mass e^+e^- collision energy respectively. This reduces the sensitivity to inefficiencies in detecting all the visible energy in an event. Otherwise, events with smaller visible energies will be more sensitive to the value of ε. The cone algorithm is described in detail in [59], including procedures to deal with overlapping cones.

3.5 Primary Vertex Determination

The primary vertex position is fitted on an event by event basis with two pseudo-tracks introduced into the fit to provide a constraint to the average beam spot position. The two pseudo-tracks are parallel to the x and y axes respectively and have perpendicular errors given by the beam spot spreads.

The procedure for measuring the beam spots is to collect events in chronological order and make a χ^2 fit to a primary vertex once there are 100 or more good tracks. A weighted average of 30 such contiguous vertices is formed. The procedure can be found in [60].

3.6 Secondary Vertex Finding

A b hadron will travel a mean distance of approximately 3 mm before decaying. Displaced secondary vertices are therefore an excellent signature for b hadrons.

For the analyses in this thesis two different methods are used to group tracks into secondary vertices in the r–ϕ plane only. The two methods are known as 'tear down' and 'build up' vertex finders. Both are described below. More details may be found in [61]. To be considered for either secondary vertex finder, as well as passing the default quality requirements detailed in section 3.3, tracks must also satisfy the following requirements :

- Maximum $\mid d_0 \mid$ with respect to the primary vertex = 1.0 cm,
- Maximum error on $\mid d_0 \mid$ (including error on primary vertex position) = 0.1 cm,
- Maximum momentum = 65 GeV/c,
- Minimum momentum = 0.5 GeV/c.

3.6.1 The 'Tear-down' Vertex Finder

In this algorithm all tracks within a given jet passing the quality requirements are considered in a fit to a secondary vertex in the r-ϕ plane. The fitting technique is the same as that used to reconstruct the primary event vertex. Tracks are discarded if they contribute more than 4 to the vertex χ^2 and the remaining tracks are refitted to a new secondary vertex. This process continues until there are less than two tracks remaining (in which case the vertex finding fails) or no tracks contribute more than four to the vertex χ^2.

This method will tend to resolve a displaced secondary vertex if the b hadron has travelled a significant distance before decaying and is more efficient if the charged track multiplicity from the b hadron decay is large. Figure 3.2 shows tracks measured by the silicon microvertex detector formed into two secondary vertices using this technique.

3.6.2 The 'Build-up' Vertex Finder

This algorithm also works in the r-ϕ plane to fit tracks to displaced secondary vertex, but with a rather different philosophy than the 'tear-down' algorithm. Two well measured tracks (requiring at least one CV axial hit or a silicon microvertex hit) with the most significant separation from the primary event vertex are taken as seed tracks. Precisely measured tracks[d], at least 2.5 standard deviations from the primary vertex, are also taken as seeds. Separated vertex candidates are formed by looping over all possible pairs of seed tracks to form a vertex nucleus. Other tracks are added to this nucleus vertex as long as they match this vertex better than the primary vertex and the vertex probability is >1%. Once associated to a vertex, a track cannot be used again. The decay length is calculated for each vertex from a fit to the primary vertex position and the seed vertex position. The r-ϕ vector momentum sum of the seed vertex tracks is used to constrain the decay length direction. When fitting the decay length the uncertainty from the primary vertex position is usually negligible, with the dominant error arising from uncertainties in the seed vertex position. If there is more than one seed vertex, the best quality one is chosen using the following criteria (in order of importance) :

- The vertex with a decay length between 0 cm and 2 cm.
- The vertex with the greatest number of precisely measured tracks.
- If the number of precisely measured tracks is exactly two, then the vertex with the largest number of tracks in the seed vertex is chosen, irrespective of how well they are measured.
- The vertex with the largest decay length significance from the primary vertex.

[d] In this thesis the only extra requirement on the seed tracks is that the maximum $|d_0|$ allowed is 0.5.

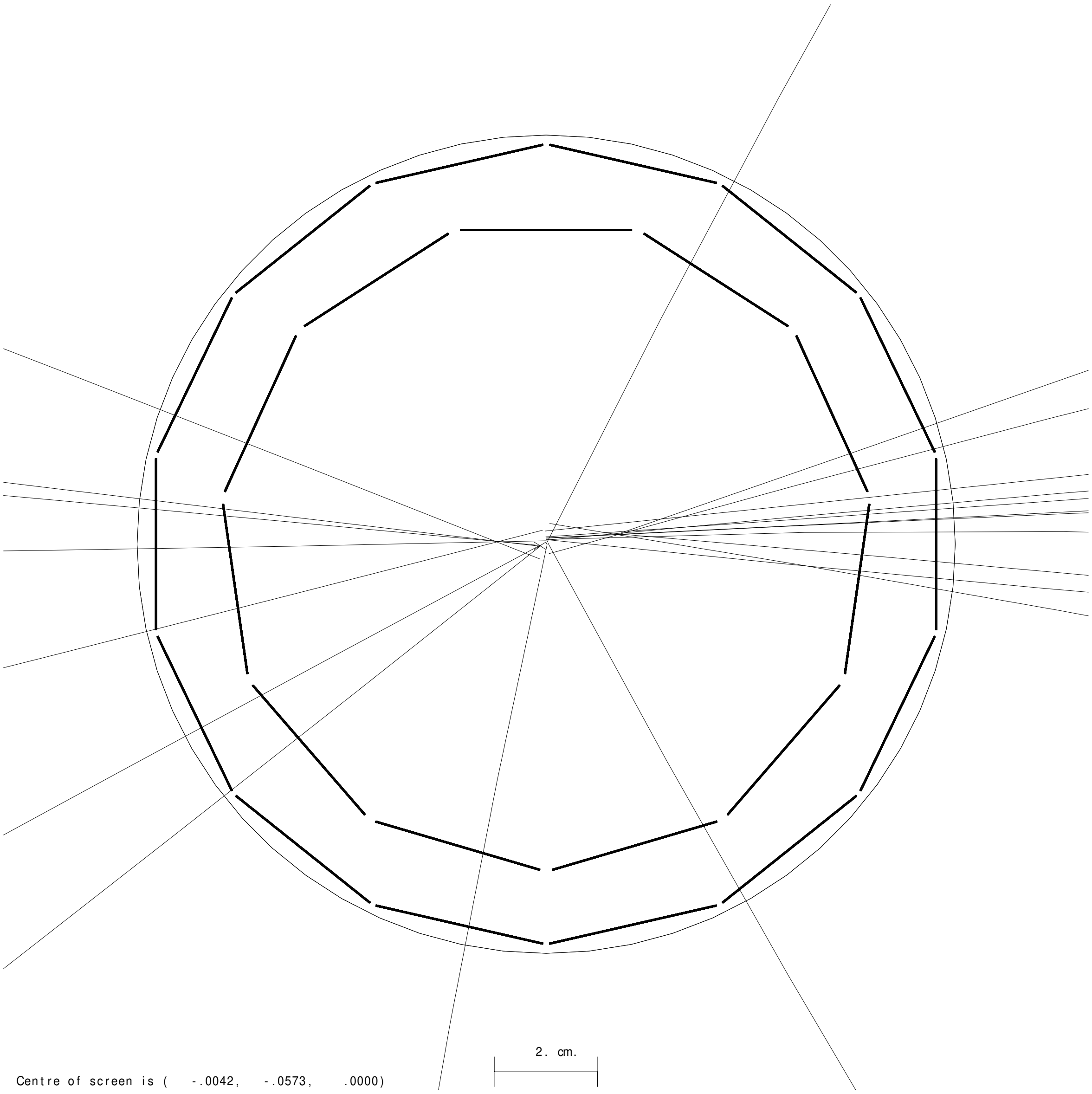

Figure 3.2: A view of the $e^+e^- \rightarrow q\overline{q}$ event shown in figure 3.1 with detail around the production vertex shown. The two concentric layers of the microvertex detector are shown. The tracks have been formed into two secondary vertices which are visible on each side of the event. The lower-most track of the secondary vertex on the left hand side is the muon candidate shown as an arrow in figure 3.1.

This algorithm can reconstruct secondary vertices displaced from the primary vertex even in light quark events. The vertices arising from non-$b\overline{b}$ events are dominantly due to charm hadron decays.

Chapter 4

Mixing Measurement using Jet Charge

4.1 Introduction

Quark mixing is an effect of the weak force which makes it possible for a B^0 hadron to mix into a $\overline{B}^0$ hadron before it decays. The strength of the mixing is measured by the parameter χ as discussed in section 1.2.2. In order to measure χ it is necessary to know the charge of the b quark at production and at decay. It is relatively easy to measure the charge at decay time as when it decays semi-leptonically the decay lepton has the same sign of charge as that of the b quark. When $b\overline{b}$ pairs are produced if you know the charge of one of them then you can deduce the charge of the other. Therefore if in an event you find two leptons from $b(\overline{b})$ decays with the same charge then one of the $b(\overline{b})$ quarks must have mixed. The problem with this approach is that demanding two high momentum and transverse momentum leptons[a] in an event results in a small data set. Another approach is to use a quantity called jet charge to measure the charge of the quarks at production and again use leptons for the charge at decay time. This approach does not suffer from the small statistics of a di-lepton analysis

[a]transverse momentum is the component of the momentum of the lepton perpendicular to the thrust axis. The thrust axis itself is defined as the direction of maximum momentum flow in an event.

however the measurement is degraded by the relatively poor charge estimating power of jet charge. It is also essential to know how well the quark charge is being estimated by this technique.

This chapter will describe a method used to measure χ in the OPAL experiment and then concentrate on my contribution which was the measurement of the charge separation δ_b. The analysis was performed on data recorded between 1992 and 1994 and used all the Monte Carlo datasets described in section 2.2.11.

4.2 Method

This analysis used a single lepton tag to identify the decay of a b-hadron and determine the decay time charge of the b-quark. The production time charge of the b-quark was inferred from a jet charge calculated in the event hemisphere opposite the lepton. The division of each event into two hemispheres was made using the plane perpendicular to the thrust axis and passing through the nominal interaction point. An identified lepton was considered to be a tag for the hemisphere that contained the axis of the lepton's jet. The jet charge, Q_j, was then calculated using:

$$Q_j = \frac{\sum_i |p_{||i}|^\kappa q_i}{\sum_i |p_{||i}|^\kappa} \tag{4.1}$$

where the sum was over all charged tracks in the opposite hemisphere, q_i was the track charge and $p_{||i}$ was the momentum component of track i along the thrust axis. Hence, Q_j was simply a normalised, momentum weighted sum of track charges where the strength of the momentum weighting was determined by the parameter κ, the value of which was chosen to be 0.5, to optimise the measurement. Figure 4.1 illustrates the conventions used.

In direct $b \to l$ decay the sign of the lepton charge is the same as that of b-quark and so gives the decay time quark charge. The jet charge of the opposite hemisphere can be used to deduce the charge of this quark at production. If the b-hadron that decays semi-leptonically has undergone mixing, the value of $Q_j Q_l$ tends to be positive whereas it tends to be negative when mixing does not take place. The mean quantity $\langle Q_j Q_l \rangle$ is therefore sensitive to the probability of mixing and can be related to χ by

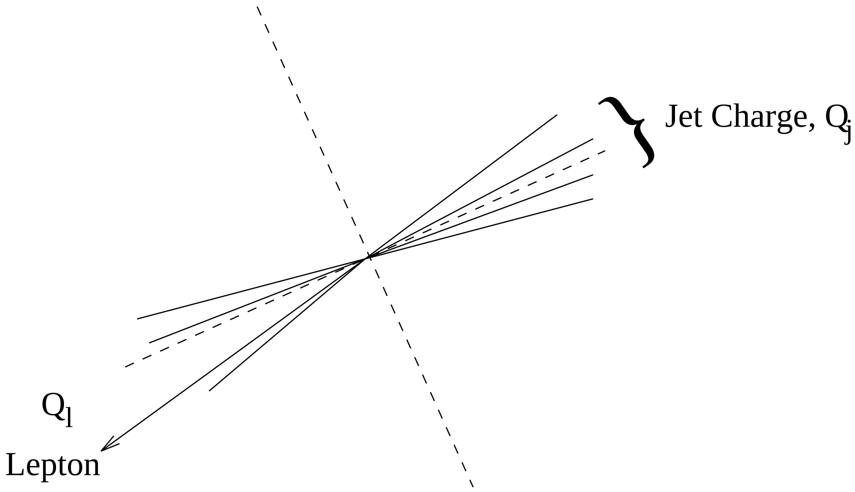

Figure 4.1: Events were divided into hemispheres using the thrust axis and the lepton charge and jet charge in the opposite hemisphere were determined.

the equation (see Appendix A):

$$\langle Q_j Q_l \rangle = \frac{1}{2}(1 - 2\chi)\delta \tag{4.2}$$

where the *charge separation*,

$$\delta = \langle Q_- \rangle - \langle Q_+ \rangle \tag{4.3}$$

where $\langle Q_- \rangle$ and $\langle Q_+ \rangle$ are the mean jet charges for a hemisphere containing a negative primary quark and positive quark respectively. A value for χ can therefore be measured once $\langle Q_j Q_l \rangle$ and δ have been determined for b events. In equation 4.2 it is assumed that Q_j in one hemisphere does not depend on whether the b-hadron in the other hemisphere has mixed or not. This assumption has been verified in Monte Carlo data.

A value for $\langle Q_j Q_l \rangle$ was extracted from data after taking into account the effect of 'cascade' decays such as $b \to c \to l$ and background from non b-decay sources of leptons [63]. In previous measurements of this kind that used a combination of jet charge and lepton tagging the value for δ had been estimated directly from Monte Carlo. This introduced large systematic errors due to modelling uncertainties. In this analysis the dependence on Monte Carlo has been greatly reduced by using a sample of b$\overline{\text{b}}$ events from the data, selected by a vertex tagging technique, in the estimation of δ.

4.3 Event Selection

In order to select multihadronic events the selection described in section 3.3 was used. To ensure that events were well contained within the detector it was required that $|\cos\theta_T| < 0.8$ where θ_T is the polar angle of the thrust axis. In addition, it was required that the thrust value be greater than 0.8 to give a sample of 2-jet events.

4.3.1 Lifetime Tagging

Lifetime tagging was performed by attempting to fit tracks within a jet to a common vertex using the 'tear down' vertex finder as described in section 3.6.1 The two dimensional decay length, L, was calculated from the positions of the secondary vertex and the primary event vertex using the jet axis as a direction constraint. The jet axis was also used to determine the sign of the decay length; $L > 0$ if the secondary vertex was displaced from the primary vertex in the same direction as the jet in the x-y plane, and $L < 0$ otherwise.

Once a secondary vertex had been found it was assigned to the event hemisphere that contained the jet. A hemisphere was considered to be tagged if it contained one or more vertices with a *decay length significance*, defined as the decay length divided by its error, greater than 8. Each vertex was also required to have at least three tracks associated with it and a decay length less than 2 cm.

4.4 Measurement of δ

The charge separation for $b\overline{b}$ events, δ_b, was estimated from the lifetime tagged sample using a technique based on that used in [65]. For a sample of events the charge separation can be calculated using (see Appendix B):

$$\delta^2 = 4\frac{-\langle Q_F Q_B\rangle + \rho[Q_-, Q_+]\sigma^2(Q) + \mu^2(Q)}{1 + \rho[Q_-, Q_+]} \tag{4.4}$$

where $\langle Q_F Q_B\rangle$ is the mean product of jet charges formed in the opposite forward and backward event hemispheres and $\sigma^2(Q)$ and $\mu^2(Q)$ are the variance and mean of the jet charges of all hemispheres. The forward hemisphere is defined as the one containing the positive z axis of OPAL[b]. The correlation coefficient, $\rho[Q_-, Q_+]$, takes into account correlations between the jet charges of opposite hemispheres and is the only quantity that was not taken directly from the event sample and was estimated using Monte Carlo. Hence, the charge separation could be determined largely from the data with little Monte Carlo input.

A lifetime tagged sample of events is dominated by $b\overline{b}$ events but has some contamination from other flavours. When Equation 4.4 is applied to the data sample, the charge separation measured is that of the particular mix of flavours. This is related to the individual charge separations by:

$$\delta = F_b\delta_b + F_c\delta_c + F_s\delta_s + F_u\delta_u + F_d\delta_d \tag{4.5}$$

where the $F_{b...d}$ are the fractions of each event flavour in the tagged sample and $\delta_{b...d}$ are the flavour dependent charge separations. If the fractions $F_{b...d}$ and charge separations $\delta_{c...d}$ are known then δ_b can extracted. Since the sample is dominated by $b\overline{b}$ events relatively little systematic uncertainty is introduced by taking the non-b quark charge separations from Monte Carlo.

4.4.1 Removing the Lifetime Bias

The charge separation extracted in this way is unfortunately biased by the lifetime tagging procedure. The tagging cuts cause a small bias towards certain B hadron decay modes and also favour events with long lived and highly boosted (i.e. fast moving) B hadrons. Of particular concern is that the neutral B mesons in the tagged sample are slightly more likely to have mixed into their charge conjugate state than usual. This is due to the fact that the average longer lifetime of the tagged B^0's means that there is a higher chance of them having mixed. Studies in [66] have clearly shown that lifetime tagging can change the charge separation, although for the cuts used here the biased charge separation is very similar to the unbiased value.

To avoid this problem, the correction procedure described in [66] was used. The unbiased charge separation can be related to the charge separation for events with no

[b]The z axis points along the direction in which the electron beam passes through OPAL.

tags, δ_b^{0t}, events with only one tagged hemisphere, δ_b^{1t}, and events with both hemispheres tagged, δ_b^{2t}, using:

$$\delta_b = \frac{N_b^{0t}}{N_b^{0t}+N_b^{1t}+N_b^{2t}}\delta_b^{0t} + \frac{N_b^{1t}}{N_b^{0t}+N_b^{1t}+N_b^{2t}}\delta_b^{1t} + \frac{N_b^{2t}}{N_b^{0t}+N_b^{1t}+N_b^{2t}}\delta_b^{2t} \tag{4.6}$$

The δ_b^{1t} and δ_b^{2t} can be measured from the data and δ_b^{0t} can be calculated from them as

$$\delta_b^{0t} = 2\delta_b^{1t} - \delta_b^{2t} \tag{4.7}$$

The numbers of each type of event are given by

$$\begin{aligned} N_b^{0t} &= N_b(1-2\varepsilon_b+\varepsilon_b^2\varrho_b) \\ N_b^{1t} &= 2N_b(\varepsilon_b-\varepsilon_b^2\varrho_b) \\ N_b^{2t} &= N_b\varepsilon^2\varrho_b \end{aligned} \tag{4.8}$$

where ε_b is the efficiency for tagging a *hemisphere* of a $\mathrm{b\overline{b}}$ event and ϱ_b is a factor that takes into account correlations between the tagging efficiencies of opposite hemispheres in an event. After substituting these expressions into equation 4.6 we obtain

$$\delta_b = 2(1-\varepsilon_b)\delta_b^{1t} + (2\varepsilon_b - 1)\delta_b^{2t} \tag{4.9}$$

The charge separations δ_b^{1t} and δ_b^{2t} were estimated from data events with only one hemisphere tagged and both hemispheres tagged respectively by measuring δ in each sample using equation 4.4 and then extracting δ_b using equation 4.5. However in order to use equation 4.5 it is necessary to calculate the fractions of each flavour present in both samples. The fractions of each flavour, j, in the single tagged events are given by,

$$F_j^{1t} = \frac{\varepsilon_j(1-\varepsilon_j\varrho_j)\frac{\Gamma_{j\bar{j}}}{\Gamma_{q\bar{q}}}}{\sum_i \varepsilon_i(1-\varepsilon_i\varrho_i)\frac{\Gamma_{i\bar{i}}}{\Gamma_{q\bar{q}}}} \tag{4.10}$$

and the corresponding fractions in the double tagged events are,

$$F_j^{2t} = \frac{\varepsilon_j^2\varrho_j\frac{\Gamma_{j\bar{j}}}{\Gamma_{q\bar{q}}}}{\sum_i \varepsilon_i^2\varrho_i\frac{\Gamma_{i\bar{i}}}{\Gamma_{q\bar{q}}}} \tag{4.11}$$

where ε_i is the hemisphere tagging efficiency for flavour i, ϱ_i is a factor that takes into account correlations between the tagging efficiencies of opposite hemispheres in an event and $\Gamma_{i\bar{i}}/\Gamma_{q\bar{q}}$ are the partial hadronic widths of the Z^0 into quark pairs $i\bar{i}$. The ratios $\Gamma_{b\bar{b}}/\Gamma_{q\bar{q}}$ and $\Gamma_{c\bar{c}}/\Gamma_{q\bar{q}}$ were taken from the average LEP measurements [69] and the $\Gamma_{i\bar{i}}/\Gamma_{q\bar{q}}$ for the lighter quarks were obtained using the program ZFITTER (version 4.8) [68], with $M_Z = 91.187$ GeV/c^2, $M_{\rm top} = 169$ GeV/c^2, $M_{\rm Higgs} = 300$ GeV/c^2, and $\alpha_s = 0.12$ [67]. The values used are shown in table 4.1.

Event Type	Partial Width
$b\bar{b}$	0.2216 ± 0.0017
$c\bar{c}$	0.1543 ± 0.0074
$s\bar{s}$	0.220
$u\bar{u}$	0.172
$d\bar{d}$	0.220

Table 4.1: Partial Widths of the Z^0 used in this analysis. The values predicted by ZFITTER version 4.8 using input parameters as determined in [67] were assumed for the u, d and s partial widths. The b and c partial widths were taken from the average LEP measurements.

The hemisphere tagging efficiencies for b and c quarks were determined mainly from the data using the 'double tagging' method described in [65]. This involves using the number of events that are tagged in one hemisphere and the number that are tagged in both hemispheres. Monte Carlo data was used only to estimate the relatively small light quark tagging efficiencies.

4.4.2 Determination of ϱ_i

The correlation parameter ϱ_i is a measure of the difference between the probability to tag an event in both hemispheres and the square of the probability for tagging one hemisphere for events of quark flavour i. For the cuts applied in this analysis the correlation factors are close to unity. As the b-fraction of the sample is large, even large deviations from unity of ϱ_u, ϱ_d, ϱ_s and ϱ_c do not significantly affect the measurement of δ_b. Hence the effect of hemisphere correlations was only included for b quark events. For small deviations from unity, the correlation factor can be expressed as $\varrho_b = 1+\Delta\varrho_b^{\rm geom}+\Delta\varrho_b^{\rm phys}$, where $\Delta\varrho_b^{\rm geom}$ comes purely from the geometry of the detector and $\Delta\varrho_b^{\rm phys}$ comes from the underlying physics processes. The correlation $\Delta\varrho_b^{\rm geom}$ due to non-uniform tagging efficiency as a function of the thrust direction was calculated from the data. This was done separately for the data taken with the two different versions of the silicon microvertex detector and for each year's data, for which the overall efficiency was different. The two bottom hadrons in a $\rm b\overline{b}$ event are likely to be produced back-to-back and their decay products are therefore likely to strike geometrically opposite parts of the detector. This introduces a correlation if the efficiency of the detector is not completely uniform. This correlation was estimated by measuring the hemisphere tagging probability for the real data in small bins of $|\cos\theta|$ and ϕ of the thrust axis direction.

The correlation $\Delta\varrho_b^{\rm geom}$ was estimated to be 0.0140 ± 0.0012 for the data taken in 1992, 0.0274 ± 0.0015 for the data taken in 1993 and 0.0223 ± 0.0009 for that taken in 1994 where the errors are statistical. The values differ due to known changes in the efficiency of the OPAL tracking system. The large change between 1992 and 1993 was due to the upgrade of the silicon microvertex detector.

Other sources of correlation, represented by the term $\Delta\varrho_b^{\rm phys}$, were investigated using Monte Carlo simulations. Those considered were the momentum-momentum correlation between the two b-hadrons produced from the b and $\rm\overline{b}$ quarks (due to gluons taking away some of the energy of the event and so reducing the momentum of both hadrons), and the negative correlations due to hard gluon radiation (which tends to reduce the back-to-back nature of the event). The correlation factor $\Delta\varrho_b^{\rm phys}$ due to these effects is $\Delta\varrho_b^{\rm phys} = +0.0087 \pm 0.0026$ [70].

4.4.3 δ Results and Systematics

Once all the necessary quantities had been measured equation 4.9 was used to calculate

$$\delta_b = -0.1435 \pm 0.0034 \pm 0.0020$$

where both errors are statistical, the first is due to the data the second to the Monte Carlo. The many sources of systematic errors for δ which have been considered are listed in table 4.2 and are now discussed in detail.

The uncertainties due to the modelling of fragmentation on the u, d, s and c jet charge properties were estimated using Monte Carlo events generated with different fragmentation parameters[c]. For each fragmentation parameter one million events were generated with the parameter set to the edges of the ranges shown in table 4.2 (which are similar to those in [65]). These variations are taken from the errors on the determination of these quantities, either from experimental measurements or from the fitting procedure used by OPAL to optimise the JETSET parameters to reproduce known measurements [49]. Since these events have not been passed through the detector simulation they cannot be directly compared to those values found in the standard Monte Carlo data sample hence one million events were also generated with no changes from the standard values. The quantities that in the analysis are taken from Monte Carlo (i.e. $\delta_{c...d}$ and $\rho[Q_-, Q_+]$) were then measured and the results examined for any evidence of a systematic change in the results. Further sets of one million events were generated at intermediate values of the parameters where necessary. The effect of changing the value of each parameter was then approximated by a straight line. The observed fractional change in value was then used to adjust the $\delta_{c...d}$ and $\rho[Q_-, Q_+]$ values used in the original calculation.

The variation of the b and c quark partial widths of the Z^0 were taken from table 4.1 while a relative uncertainty of 15% was assumed on the u, d and s partial widths as shown in table 4.2.

The effects of incorrect modelling of the track resolutions in r-ϕ and $\cos\theta$ on the quantities taken from Monte Carlo were investigated by smearing the Monte Carlo. The factor rescaling the difference between the true and reconstructed values of the r-ϕ track parameters was varied by 20%, while that of the $\cot\theta$ was increased by 100%, as the z resolution of OPAL is much worse than the r-ϕ resolution.

The determination of δ is also sensitive to the average tagging efficiencies of the various quark flavours. These have to be known in order to determine the fraction of the different flavours in the sample. The charm and bottom tagging efficiencies

[c]These events are not passed through GOPAL, the detector simulation, as this process is very CPU intensive

are determined directly from the data, which makes the measurement insensitive to the modelling of the heavy quark fragmentation and decay. The u, d and s tagging efficiencies were determined from Monte Carlo. The efficiency for tagging a hemisphere in a b-event is found to be 8.6% higher in the data than the Monte Carlo. This could be due to the incorrect b-lifetime value in the Monte Carlo, or else be due to smearing effects in the data that are not well modelled in the Monte Carlo. To account for such a possible effect, the tagging efficiencies for the light quarks were increased by 8.6%, and the resulting change in the measured delta is taken as a systematic uncertainty. Finally the correlation factor ϱ_b has an error due to Monte Carlo statistics. The analysis was repeated with the correlation factor varied accordingly.

The most important contributions to the systematic error come from the fragmentation parameters which are used in the Monte Carlo and those from incorrect modelling of the detector resolution. The total systematic error on δ_b was determined to be 0.0065 as detailed in table 4.2.

4.5 χ Results

The method used to measure the quantity $\langle Q_j Q_l \rangle_b$ is described in [63], and gave a value of:

$$\langle Q_j Q_l \rangle_b = -0.0574 \pm 0.0010 \pm 0.0008$$

where the errors are statistical and systematic. Equation 4.2 was then used to combine this result with the value of δ obtained above to give a value for the time averaged mixing of:

$$\chi = 0.100 \pm 0.012 \pm 0.006 \pm 0.019$$

where the errors are respectively from data statistics, Monte Carlo statistics and systematics.

An OPAL measurement, performed at around the same date as this measurement, of time averaged mixing [71] using leptons obtained the result

$$\chi = 0.1107 \pm 0.0062 \pm 0.0055$$

where the first error is statistical and the second is systematic. The two results are compatible, however it is clear that the precision of this jet charge measurement is worse in comparison. The two results are, however, not strongly correlated and have been combined taking into account any common sources of systematic errors to give $\chi = 0.1097 \pm 0.0080$ [63]. Other measurements of χ are shown in table 4.3. Here it can be seen that both DELPHI and ALEPH also have much larger systematic errors on the jet charge measurements than the di-lepton measurements, while the statistical errors are much the same[d]. This OPAL jet charge analysis has a larger statistical error than the di-lepton analysis because the procedure used to remove any bias in δ_b needs a sample of events with tags in both hemispheres. In analyses where this correction is not made this double tagged sample is not required.

[d] For both collaborations the two analyses shown were measured using roughly the same dataset.

Systematic Errors				
Parameter		Nominal Value	Range	$\Delta\delta_b$
Λ_{QCD},	PARJ(81)	0.29	0.28 — 0.31	∓0.0001
Q_0,	PARJ(82)	1.0	0.7 — 1.8	±0.0017
σ_q,	PARJ(21)	0.37	0.32 — 0.40	±0.0007
γ_s,	PARJ(2)	0.285	0.250 — 0.320	∓0.0006
$[V/(V+S)]_{\mathrm{u,d}}$,	PARJ(11)	0.50	0.30 — 0.75	∓0.0040
$[V/(V+S)]_{\mathrm{s}}$,	PARJ(12)	0.60	0.50 — 0.75	∓0.0010
$[V/(V+S)]_{\mathrm{c,b}}$,	PARJ(13)	0.75	0.65 — 0.80	∓0.0007
ϵ_b,	PARJ(55)	0.0055	0.0025 — 0.0095	±0.0003
ϵ_c,	PARJ(54)	0.05	0.03 — 0.07	±0.0009
direct baryon rate,	PARJ(1)	0.1	0.08 — 0.12	∓0.0003
popcorn parameter,	PARJ(5)	1	0 — 2	±0.0004
mixing $\begin{smallmatrix} x_d \\ x_s \end{smallmatrix}$	*PARJ*(76) *PARJ*(77)	0.7 ∞	0–0.7 0–∞	∓0.0003
Fragmentation				±0.0047
$\Gamma_{\mathrm{b\overline{b}}}/\Gamma_{\mathrm{q\overline{q}}}$		0.2216	±0.0017	∓0.0001
$\Gamma_{\mathrm{c\overline{c}}}/\Gamma_{\mathrm{q\overline{q}}}$		0.1543	±0.0074	∓0.0001
$\Gamma_{\mathrm{s\overline{s}}}/\Gamma_{\mathrm{q\overline{q}}}$		0.220	±0.033	∓0.0002
$\Gamma_{\mathrm{u\overline{u}}}/\Gamma_{\mathrm{q\overline{q}}}$		0.172	±0.026	±0.0007
$\Gamma_{\mathrm{d\overline{d}}}/\Gamma_{\mathrm{q\overline{q}}}$		0.220	±0.033	∓0.0005
Standard Model				±0.0009
r-ϕ smearing factors			±0.2	∓0.0025
$cot\theta$ smearing factor			1 — 2	±0.0035
Detector				±0.0043
u, d and s efficiency			100 — 109%	∓0.0005
efficiency correlation factor			±0.009	±0.0001
Sample Composition				±0.0005
Total Systematic				±0.0065

Table 4.2: The sources of systematic errors on the measurement of δ (PARJ parameters are the specific parameters changed in JETSET).

	Method	Result
ALEPH	jet charge	$0.113 \pm 0.018 \pm 0.027$ [72]
ALEPH	di-lepton	$0.114 \pm 0.014 \pm 0.008$ [73]
DELPHI	jet charge	$0.144 \pm 0.014^{+0.017}_{-0.011}$ [74]
DELPHI	di-lepton	$0.121 \pm 0.016 \pm 0.006$ [75]
L3	di-lepton	$0.123 \pm 0.012 \pm 0.008$ [76]
World Average	–	0.126 ± 0.008 [14]

Table 4.3: Other Measurements of χ. The errors are statistical and systematic respectively.

Chapter 5

B^{**} Reconstruction

5.1 Introduction

The resonant P-wave states B^{**} and B_s^{**} can decay via the strong interaction to give $B^{(*)}\pi$ or $B^{(*)}K$ combinations respectively where $B^{(*)}$ indicates either a B or a B^* state. As this decay is via the strong interaction the resultant π or K will emerge from the primary vertex. Hence B^{**} and B_s^{**} states are studied by combining b hadron candidates with a π or K from the primary vertex. Previous work on this topic has been reported by ALEPH [77], DELPHI [78], and OPAL [79]. All three experiments have found a large excess of $B^{(*)}\pi$ combinations due to B^{**} production. DELPHI [80] and OPAL [79] have also found evidence for B_s^{**} production.

This analysis was derived from the initial OPAL work [79] and was carried out with two main aims. Firstly to increase the efficiency of the selection by removing a vertex charge determination used in the previous analysis and loosening other cuts in the analysis. Secondly to maintain a good mass resolution which would, in particular, be sufficient to resolve the two B_s^{**} peaks reported by DELPHI [80]. In this analysis events with a reconstructed secondary vertex well separated from the primary vertex are selected, and the direction and energy of the weakly decaying b hadron is estimated. The mass of this b hadron combined with any π or K candidates coming from the primary vertex is then calculated. The presence of P-wave states gives rise to narrow structures in the invariant mass distribution of the above combinations.

5.2 Data Selection

The selection cuts used in this analysis were studied and optimised using four million multihadronic and one million $b\bar{b}$ Monte Carlo events generated by the JETSET 7.4 program (see section 2.2.11). The B^{**} and B_s^{**} states present in the Monte Carlo are shown in table 5.1. Data was taken from the entire LEP 1 dataset requiring that the

State	Mass (GeV)	Width (GeV)
	B^{**}	
B_1	5.725	0.020
B_2^*	5.737	0.025
B_1^*	5.770	0.300
B_0^*	5.750	0.300
	B_s^{**}	
B_s1	5.874	0.001
B_s^*2	5.886	0.001
B_s^*1	5.854	0.025
B_s^*0	5.834	0.05

Table 5.1: The B^{**} and B_s^{**} states present in the Monte Carlo.

silicon microvertex detector be fully operational to ensure good vertexing. In order to select good quality multihadronic events the selection described in section 3.3 was applied.

Candidate $b\bar{b}$ events were selected by searching for secondary vertices. After the 'build up' vertex finder (section 3.6.2) had been applied, secondary vertices were accepted if they contained at least 3 tracks and if the output from a neural network [81] designed to reject non-b background was acceptable[a]. The primary vertex position was then redetermined excluding the tracks assigned to the secondary vertex from the fit.

[a]The network has 7 input parameters the most important of which are the decay length from the primary to the secondary , the uncertainty in the decay length, the number of tracks in the secondary vertex and their impact parameters.

An efficiency for $b\overline{b}$ events of $\sim$44% was achieved with a purity of $\sim$90%.

5.3 Inclusive B Reconstruction

5.3.1 Introduction

In order to reconstruct B hadrons a vertex weight method was used. This involves forming weighted sums over all the tracks in a jet with an associated secondary vertex. The weights used, ω_i, are the probability that track i with momentum $\vec{p}_i$ came from the secondary vertex. An estimate of the charged component of the B momentum vector can then be given as

$$\vec{p}_{vtx} = \sum_{i=1}^{N_{jet}} \omega_i \vec{p}_i \tag{5.1}$$

Neutral particles are not assigned a weight and so have to be accounted for separately. In this analysis the electromagnetic clusters within 0.4 radians of $\vec{p}_{vtx}$ are summed together to form $\vec{p}_{EM}$, which can then be combined with the weighted sum as required.

The direction from the primary to the secondary vertex is also available and is used in the determination of the ϕ direction of the B momentum as the vertexing is performed only in the $r\phi$ plane.

In this analysis two ways of calculating ω were used. The first method uses the impact parameters of each track with respect to the primary and secondary vertices to produce the weights for an estimated B direction[b]. The angle of each track to this estimated B direction is then used as one of the inputs into a neural network which has been trained to reject non b-decay tracks. The output of this neural net is then used as the basis of the second ω used. This final ω is then used to perform the final reconstruction of the energy and direction of the B.

[b]The energy of the B did not need to be calculated at this point

5.3.2 Impact Parameter weight

In this method a first estimate of the weight is given by:

$$\omega' = \frac{R\left(\frac{b}{\eta}\right)}{R\left(\frac{b}{\eta}\right) + R\left(\frac{d}{\sigma}\right)} \tag{5.2}$$

where R is a symmetric function describing the distribution of impact parameter significance with respect to a fitted vertex, b and η are the impact parameter and associated uncertainty in the $r - \phi$ plane with respect to the secondary vertex, and d and σ are the same quantities with respect to the primary vertex. The probability, ω, that a track with a given ω' came from the secondary vertex is determined by studying Monte Carlo events. Tracks are divided into bins of ω' and for each bin the number of tracks from the secondary vertex is divided by the total number of tracks. It is found that the value of ω as a function of ω' depends strongly on the momentum of the track and so the calculation of ω is performed in 5 bins of momentum. For each of the momentum bins the function:

$$\omega = \alpha\ \omega'^{\ \beta} + \gamma\ \omega'^{\ \delta} \tag{5.3}$$

is used and the parameters α, β, ω and δ are determined from the fit. Once the value of ω has been calculated, for each track, the sums $\vec{p}_{vtx}$ and $\vec{p}_{EM}$ are then constructed as described earlier. The vector $\vec{p}_{IP}$ is then defined as:

$$\vec{p}_{IP} = \vec{p}_{vtx} + 0.7\vec{p}_{EM} \tag{5.4}$$

The $\vec{p}_{EM}$ term is scaled by a constant in order to optimise the B direction estimate. The scaling factor of 0.7 used here is taken from the previous OPAL measurement [79]. As the ϕ direction determination from the vertexing is much more accurate than that given by $\vec{p}_{IP}$ the direction of the b hadron ($\vec{p}_{\mathrm{B}}^{\,est}$) is estimated using the ϕ angle defined by the vector from the primary vertex to the secondary vertex and the θ angle from the vector $\vec{p}_{IP}$.

5.3.3 NN weight

In this improved method the initial weight ω' is the output of an artificial neural net (NN) trained to differentiate between tracks coming from a secondary vertex and those from the primary vertex [83]. The inputs to the neural net for each track are:

- The impact parameter divided by its associated uncertainty in the $r-\phi$ plane with respect to the secondary vertex.
- The impact parameter divided by its associated uncertainty in the $r-\phi$ plane with respect to the primary vertex.
- The momentum of the track.
- The cosine of the angle between the track and an estimate of the B decay direction ($\vec{p}_{\mathrm{B}}^{\,est}$).

The correspondence between ω' and the probability, ω that the track came from the secondary vertex is fairly independent of momentum and so the calculation of ω is performed in one momentum bin. The distribution of the output of the neural net has narrow peaks in it that cause a discontinuity in the function describing the probability that a track came from a secondary vertex (see figure 5.1). Hence the calculation of ω is performed in 6 bins of the weight ω'. The calculation is performed using polynomials[c] fitted to each section of the function.

Again the vector sums $\vec{p}_{vtx}$ and $\vec{p}_{EM}$ are formed and the vector $\vec{p}_{NN}$ is then defined as:

$$\vec{p}_{NN} = \epsilon\ \vec{p}_{vtx} + \zeta\ \vec{p}_{EM} \tag{5.5}$$

As this direction is used in producing the $\mathrm{B}^{**}_{(\mathrm{s})}$ mass plots the scaling factors ϵ and ζ were determined by looking at the resolution curve for the mass of $\mathrm{B}\pi(\mathrm{K})$ combinations in the Monte Carlo. Optimal values were chosen that minimised the root mean square error (RMS) and full width of the distributions while also keeping the position of the mean and peak as near to zero as possible. This procedure yielded values of $\epsilon = 1.0$ and $\zeta = 0.7$.

[c] The order of the polynomial depended on the complexity of the region to be fitted.

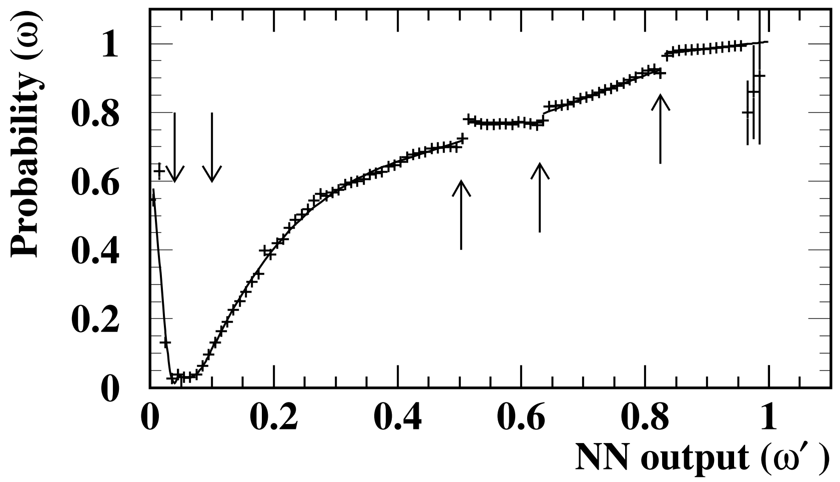

Figure 5.1: The probability that a track came from the secondary vertex as a function of the NN output. The arrows mark the edges of the 6 fitted sections.

5.3.4 B direction reconstruction

The available information for the B direction reconstruction consists of the ϕ angle from the vertexing (ϕ_{vertex}) and the θ and ϕ angles from $\vec{p}_{NN}$ (θ_{NN}, ϕ_{NN}). As two versions of ϕ are available a method to gauge the relative accuracy of the two angles is needed.

The error on ϕ_{vertex} calculated only from the vertex positions and covariances, $\sigma(\phi_{vertex})_{cov}$, does not assess the possible errors from having the wrong tracks placed in the vertex or excluding the correct tracks. Hence $\sigma(\phi_{vertex})_{cov}$ will under estimate the error on ϕ_{vertex}. To give a more representative error, $\sigma(\phi_{vertex})$, Monte Carlo data is used to take the ratio of the RMS of the ϕ_{vertex} resolution curve and the average $\sigma(\phi_{vertex})_{cov}$. This factor, which was measured to be 2.22, is then used to scale up the error i.e. $\sigma(\phi_{vertex}) = 2.22\sigma(\phi_{vertex})_{cov}$.

The accuracy of $\vec{p}_{vtx}$ in reproducing the ϕ angle of the B is assessed using the estimated RMS of the ϕ angle

$$\sigma(\vec{p}_{vtx})_\phi = \sqrt{\sum_{i=1}^{N_{jet}}(1-\omega_i)[\Delta\phi_i]^2 + \omega_i\left[(1-\omega_i)\frac{\Delta\phi_i}{\omega_i}\right]^2} \tag{5.6}$$

where $\Delta\phi_i$ is the change in the ϕ angle of $\vec{p}_{vtx}$ when the effect of track i is removed from $\vec{p}_{vtx}$. The first term is the probability that track i didn't come from the secondary vertex multiplied by the square of the error this inclusion caused i.e. $\Delta\phi_i^2$. The second term is the probability that this track did come from the secondary vertex multiplied by the square of an estimate of the error caused by only including ω_i of this track in $\vec{p}_{vtx}$. This estimate of the error is made by assuming a linear dependence of the error on the weight with which the track enters the sum. Since ϕ_{NN} is calculated from $\vec{p}_{vtx}$ and $\vec{p}_{EM}$ and this error only reflects the error on $\vec{p}_{vtx}$ the error on ϕ_{NN} has a strong dependence on the ratio $|\vec{p}_{vtx}|/|\vec{p}_{NN}|$ as well as on $\sigma(\vec{p}_{vtx})_\phi$ so $\sigma(\phi_{NN})$ is estimated as

$$\sigma(\phi_{NN}) = \kappa_\phi(|\vec{p}_{vtx}|/|\vec{p}_{NN}|)\sigma(\vec{p}_{vtx})_\phi \tag{5.7}$$

The function κ_ϕ is found by studying Monte Carlo data in bins of $|\vec{p}_{vtx}|/|\vec{p}_{NN}|$ and taking the RMS of the ϕ_{NN} resolution curve and dividing it by the average $\sigma(\vec{p}_{vtx})_\phi$. A polynomial is then fitted to the distribution (see Figure 5.2a) reproducing the shape quite well.

Having now obtained errors for the two ϕ values that have been measured a weighted mean is taken of the two

$$\phi_{comb} = \frac{\dfrac{\phi_{NN}}{\sigma(\phi_{NN})^2} + \dfrac{\phi_{vertex}}{\sigma(\phi_{vertex})^2}}{\dfrac{1}{\sigma(\phi_{NN})^2} + \dfrac{1}{\sigma(\phi_{vertex})^2}} \tag{5.8}$$

with an error given by

$$\sigma(\phi_{comb}) = \sqrt{\frac{1}{\dfrac{1}{\sigma(\phi_{NN})^2} + \dfrac{1}{\sigma(\phi_{vertex})^2}}} \tag{5.9}$$

The resolution curves obtained in the Monte Carlo for ϕ_{vertex}, ϕ_{NN} and ϕ_{comb} (with no cuts on $\sigma(\phi_{vertex})$, $\sigma(\phi_{NN})$ or $\sigma(\phi_{comb})$) are shown in Figure 5.3. These show that while the ϕ_{vertex} resolution is visibly narrower in the peak it has a larger RMS (due to tails) than the the ϕ_{NN} resolution, the ϕ_{comb} resolution has both a relatively narrow peak and a smaller RMS than both the input ϕ's.

In the same way as for ϕ_{NN} the error on θ_{NN} is calculated from the estimated RMS for the θ given by $\vec{p}_{vtx}$ and the ratio $|\vec{p}_{vtx}|/|\vec{p}_{NN}|$

$$\sigma(\theta_{NN}) = \kappa_\theta(|\vec{p}_{vtx}|/|\vec{p}_{NN}|)\sigma(\vec{p}_{vtx})_\theta \tag{5.10}$$

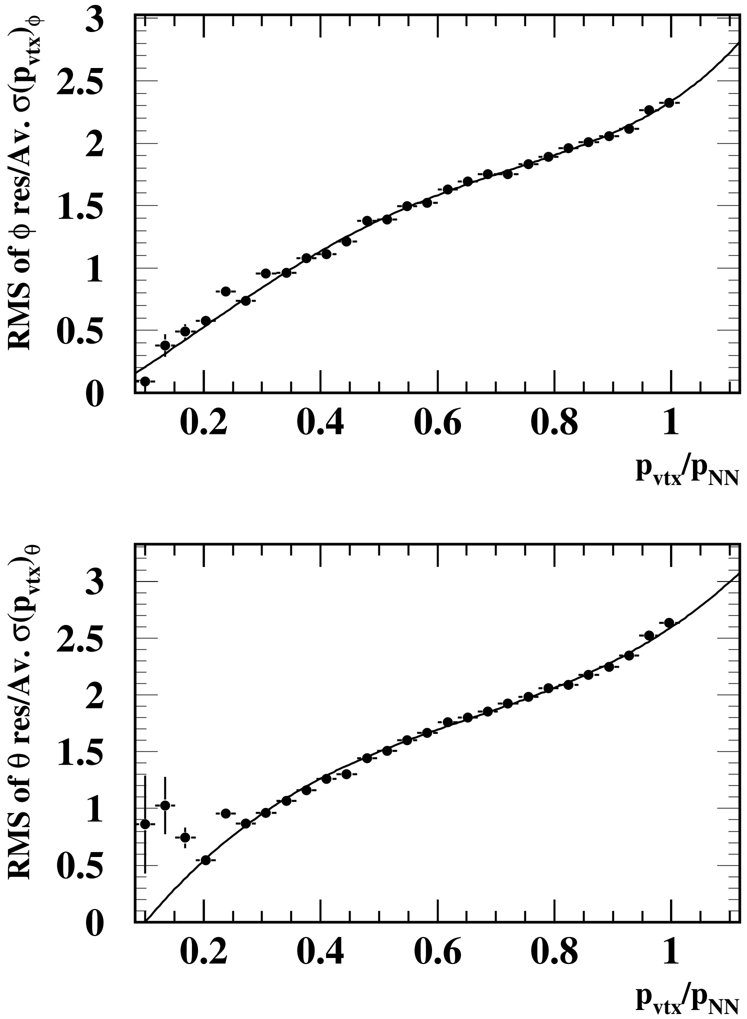

Figure 5.2: a) The function κ_ϕ used in determining $\sigma(\phi_{NN})$. b) The function κ_θ used in determining $\sigma(\theta_{NN})$.

where

$$\sigma(\vec{p}_{vtx})_\theta = \sqrt{\sum_{i=1}^{N_{jet}} (1-\omega_i)[\Delta\theta_i]^2 + \omega_i \left[(1-\omega_i)\frac{\Delta\theta_i}{\omega_i}\right]^2} \tag{5.11}$$

and $\Delta\theta_i$ is the change in the θ angle of $\vec{p}_{vtx}$ when the effect of track i is removed from $\vec{p}_{vtx}$. The fitted function κ_θ is shown in figure 5.2b the agreement is quite good apart from the first few bins which have relatively few events in. The resolution curve for θ_{NN} with no cut on $\sigma(\theta_{NN})$ is shown in figure 5.4. This shows that the resolution for θ_{NN} is poorer than that for ϕ_{NN} (figure 5.3b), which is due to the fact that only r-ϕ information is used from the silicon microvertex detector in this analysis.

5.3.5 B Energy determination

An initial estimate of the B energy can be obtained by forming the quantities E_{vtx} and E_{EM}. E_{vtx} is given by the sum

$$E_{vtx} = \sum_{i=1}^{N_{jet}} \omega_i \sqrt{p_i^2 + m_\pi^2} \tag{5.12}$$

where ω_i and p_i are respectively the secondary vertex weight and momentum of track i. E_{EM} is the sum of the energy of all the EM clusters within 0.4 radians of p_{vtx}. The energy estimate provided by combining E_{vtx} and E_{EM} can be improved by using the centre of mass energy, E_{CM}, and the recoil mass of the rest of the event, m_{rec}, to give an estimated total energy for the jet, E_{jet}^{tot}, and then subtracting an estimate of the fragmentation energy in the jet, E_{frag}.

$$E_B = E_{jet}^{tot} - E_{frag} \tag{5.13}$$

from two body decay kinematics E_{jet}^{tot} is given by

$$E_{jet}^{tot} = \frac{E_{CM}^2 - m_{rec}^2 + m_{jet}^2}{2E_{CM}} \tag{5.14}$$

where m_{jet} is set to the B mass. E_{frag} is estimated by

$$E_{frag} = E_{jet}^{vis} - cE_{vtx} - dE_{EM} \tag{5.15}$$

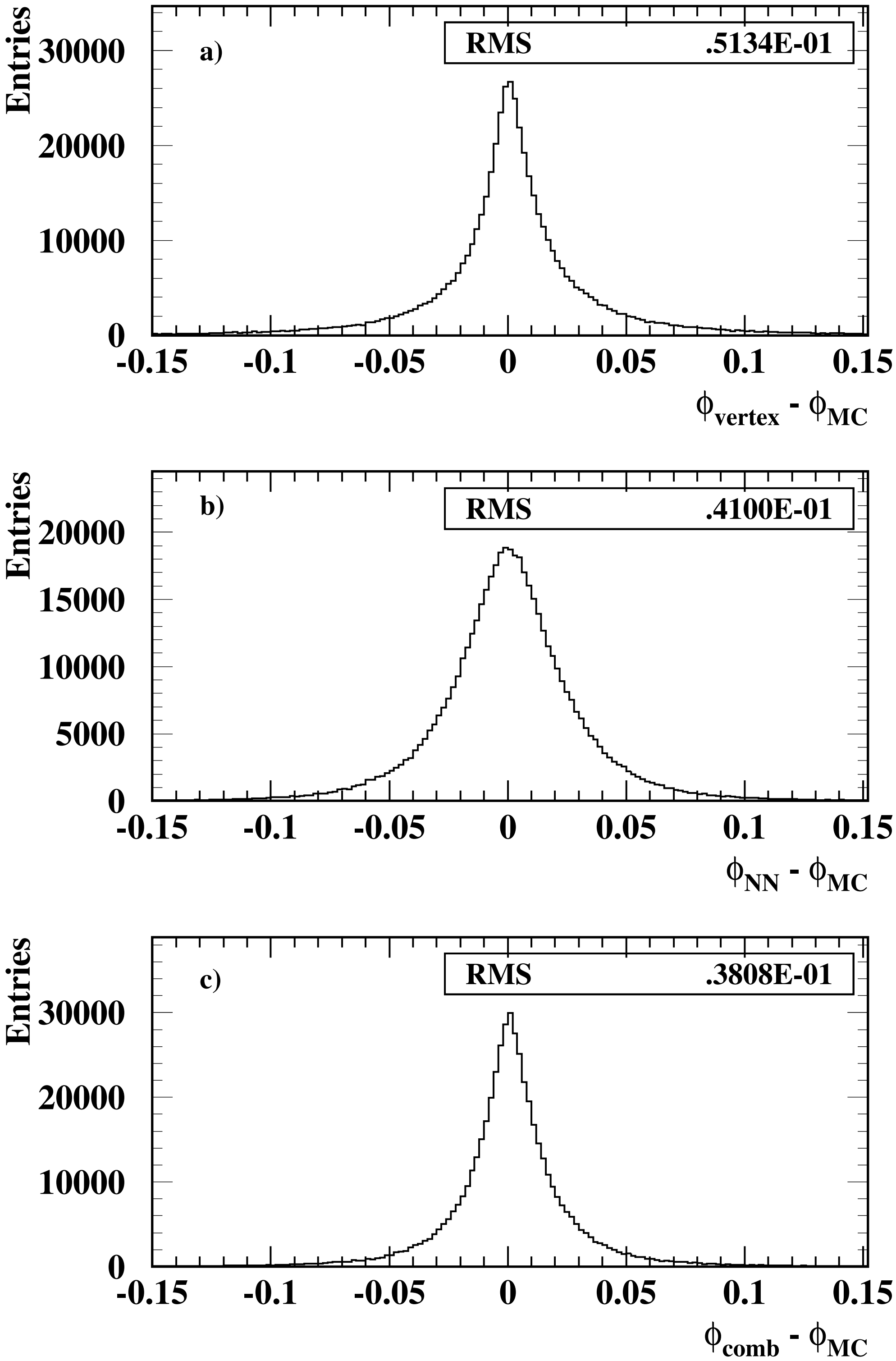

Figure 5.3: The ϕ resolution in the Monte Carlo on the reconstructed B direction using a) ϕ_{vertex} b) ϕ_{NN} and c) ϕ_{comb}

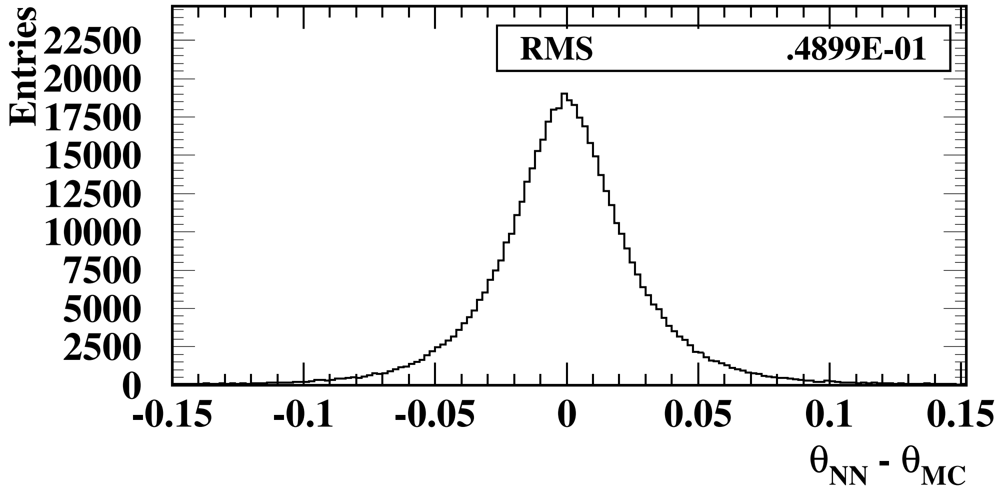

Figure 5.4: The θ resolution in the Monte Carlo on the reconstructed B direction using θ_{NN}

where E_{jet}^{vis} is the sum over all charged tracks and unassociated electromagnetic clusters in the jet. The optimal values of the constants c and d were determined by looking at the E_B resolution for Monte Carlo data. The values were chosen so as to give the smallest RMS while keeping the mean at zero yielding $c = 0.93$ and $d = 0.83$. Figure 5.5 shows the resolution obtained using these values. The peak of the distribution is offset from zero because the distribution has a large positive tail and the constants were chosen to minimise the mean.

After reconstruction of the B energy some badly reconstructed B candidates are removed by requiring that the reconstructed energy is more than 65% of the charged energy and also more than 15 GeV. Most of the B candidates that are reconstructed have an energy well above these cuts.

5.4 Selecting $\mathrm{B}_{(\mathrm{s})}^{**}$ Candidates

The quantity which is most accessible experimentally to measure the B^{**} mass peaks is the Q-value of the decay:

$$Q = m(\mathrm{B}\pi) - m(\mathrm{B}) - m(\pi) \tag{5.16}$$

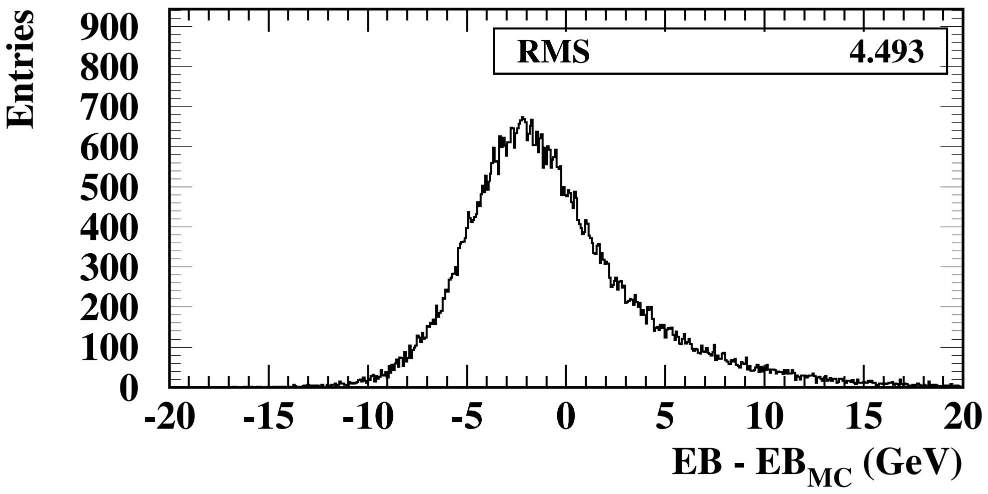

Figure 5.5: The B energy resolution measured in the Monte Carlo using the constants $c = 0.93$ and $d = 0.83$.

where m(Bπ), the invariant mass, is calculated as:

$$m(\mathrm{B}\pi) = \sqrt{m_{\mathrm{B}}^2 + m_\pi^2 + 2E_{\mathrm{B}}E_\pi - 2\vec{p}_{\mathrm{B}} \cdot \vec{p}_\pi} \tag{5.17}$$

with m_{B} fixed to 5.279 GeV. The Q-value for the B_s^{**} decay is calculated in a similar way using the kaon instead of the pion.

The studies of B** reconstruction were performed using a Monte Carlo with the B** masses shown in Figure 5.6a. This shape is formed from 2 degenerate sets[d] of two narrow and two wide resonances with very similar masses. The B** may decay via a B* followed by the decay $\mathrm{B}^* \to \mathrm{B} + \gamma$ with the γ being unmeasured. This means that the Q distribution shown in figure 5.6b has two peaks, the lower one being due to the loss of energy caused by the loss of the photon. The input B_s^{**} masses are shown in figure 5.6c. This shape consists of two narrow resonances and two wide resonances. The wide resonances are lower in mass than the two narrow ones. In this case the lower narrow input resonance decays entirely via B* and this means that only three peaks appear in the Q distribution shown in figure 5.6d.

The cuts used in this analysis are in general optimised by placing them at a point where further gains in purity are limited and would cause large losses of efficiency.

[d] One set for B$^{**\pm}$ and the other for B^{**0}.

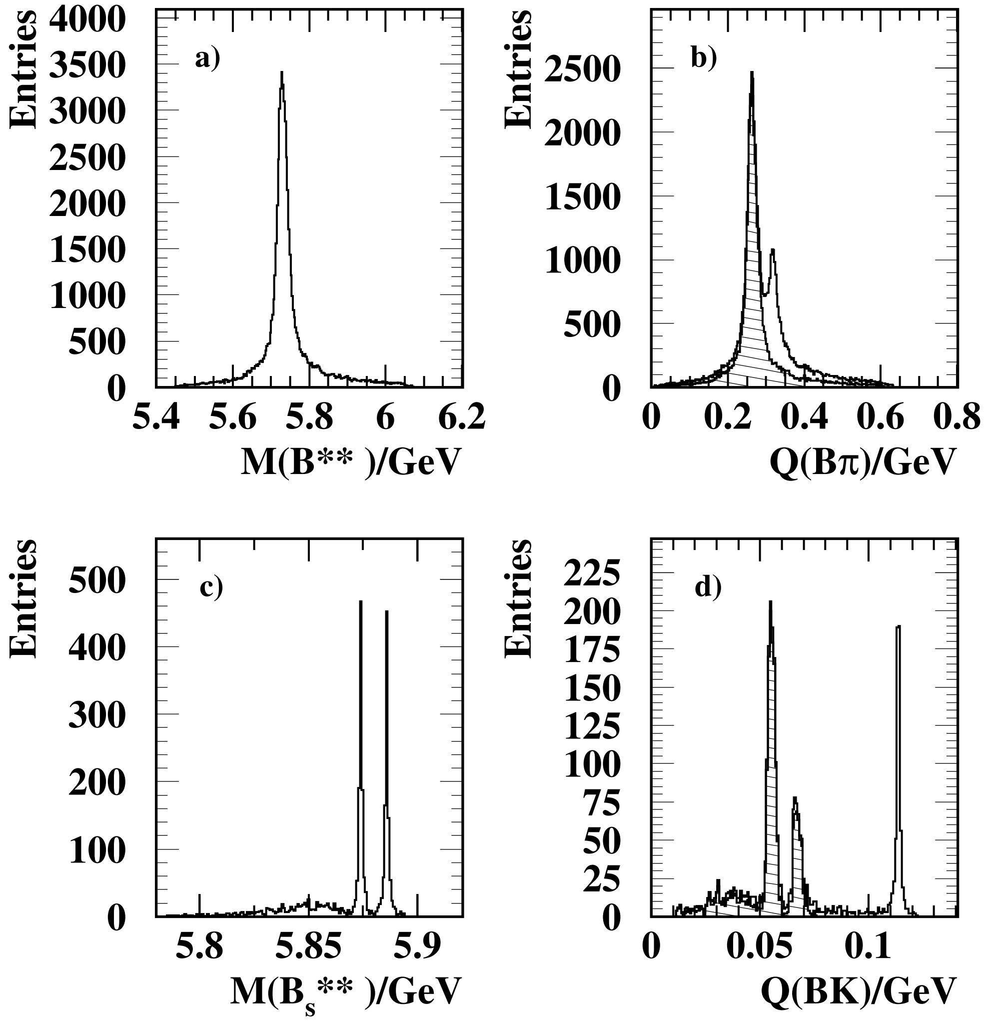

Figure 5.6: a) Mass of B^{**}'s in the Monte Carlo, b) Q-value distribution of $B\pi$ combinations, in the Monte Carlo, coming from B^{**}'s (hatched area is due to $B^{**}\to B^{*}\pi$), c) mass of B_s^{**}'s in the Monte Carlo and d) Q-value distribution of BK combinations, in the Monte Carlo, coming from B_s^{**}'s (hatched area is due to $B_s^{**}\to B^{*}K$)

5.4.1 B** Selection

Having already obtained an estimate of the B direction and momentum it is now necessary to try and find signal pions. These should be emerging from the primary vertex. Hence the pion selection was designed to select pion candidates from the primary vertex. The selection was also designed to ensure only well measured tracks were used. The requirement that the track be well measured is already satisfied in r-ϕ as the basic track selection (section 3.3) requires more than 20 hits in the CJ detector. To give a good z measurement tracks were required to have more than three hits in the CZ chambers or to be constrained to an endpoint in the CJ detector[e].

To provide a sample which mainly consists of pions the probability that a pion would give rise to the measured dE/dx of a track in the CJ detector was required to be more than 0.3%. A plot of how the B** purity[f] changes with the efficiency for different values of this cut is shown in figure 5.7. The position of the cut is indicated by the arrow on the plot.

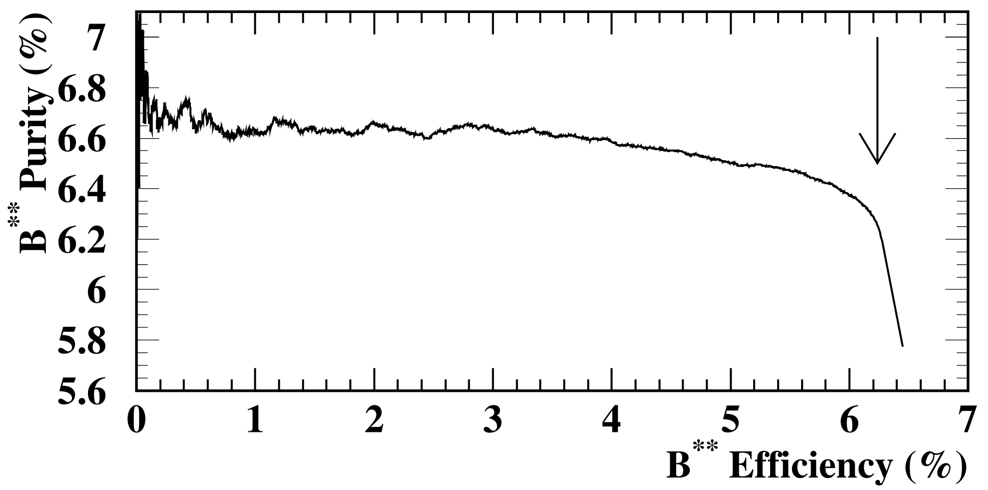

Figure 5.7: The effect of cutting on the minimum pion dE/dx weight on the efficiency and purity for B**'s after all other cuts.

---

[e]An endpoint was used where the track is at such a θ that it passes through the end of the CJ detector missing the CZ detector. The last wire with hits from the track provides a good measurement of where it left the CJ detector.

[f]Purity was measured in the Q range 0.–0.6 GeV.

In order to select candidate tracks from the primary vertex a cut was placed on the secondary vertex weight, ω, of each track requiring it to be less than 0.55. A plot of the signal purity versus efficiency for different values of this cut is shown in figure 5.8. Here it can be seen that cutting hard on *omega* causes the purity to go down again.

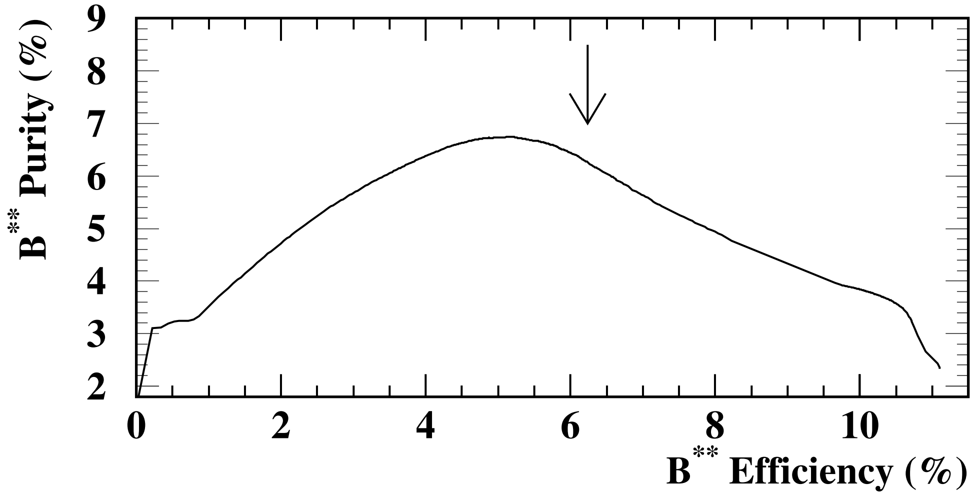

Figure 5.8: The effect of cutting on the probability that a track came from the secondary vertex on the efficiency and purity for B^{**}'s after all other cuts.

The momentum of the tracks was also examined to see if cuts could be applied to improve the signal purity. Figure 5.9 shows the distribution of track momenta for signal and background tracks, it can be seen that the momentum of signal tracks extends over the same range as the background although the spectrum has a different shape. No cut has been applied on the momentum since in order to have any effect a large amount of signal would be removed, and this would bias the mass spectrum.

After all cuts the selected sample consisted of 91% π, 5.5%K, 2.4% μ/e and 1.3% protons.

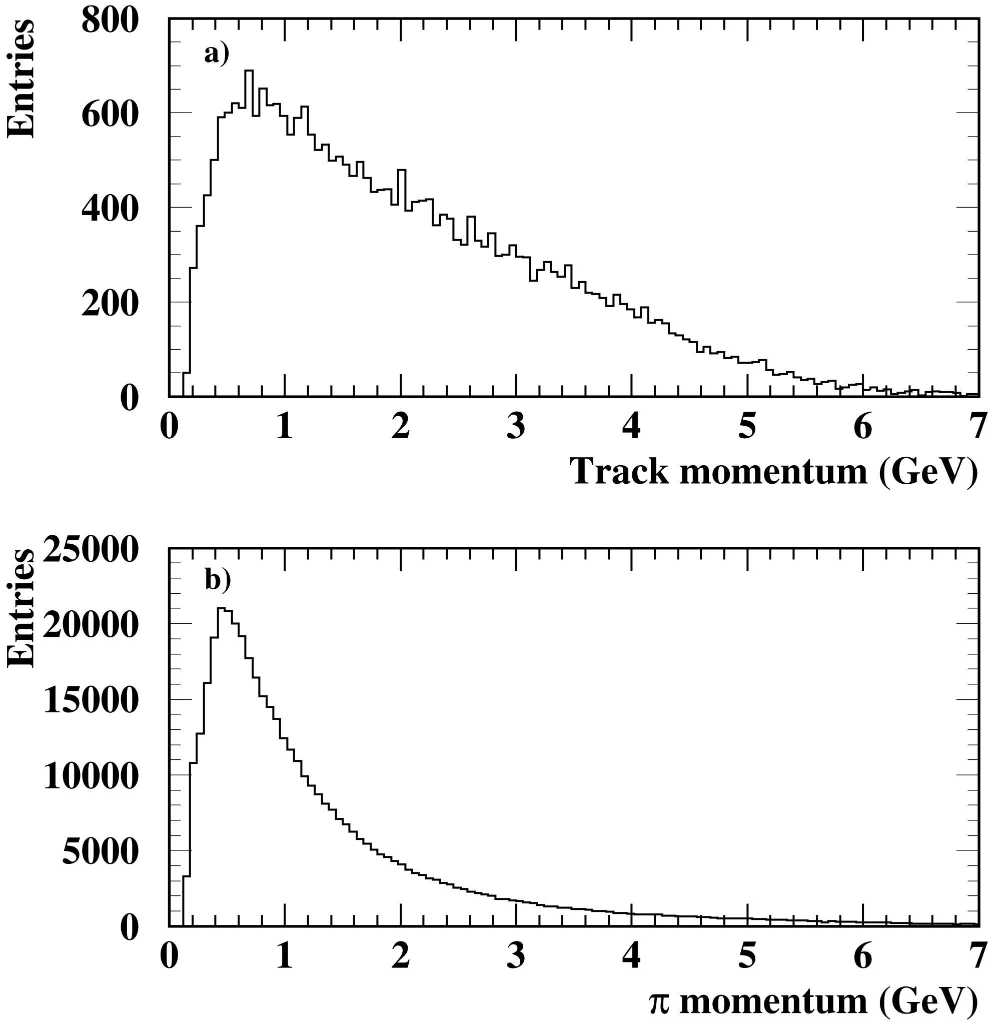

Figure 5.9: The distribution of track momentum for a) π's from B^{**}'s and b) all tracks not from B^{**}'s after all other cuts.

5.4.2 B_s^{**}Selection

The kaon selection needed to fulfil a similar purpose to the pion selection, of selecting well measured candidate kaons from the primary vertex but the selection of kaons is more complicated than that of the pions due to the production rate of kaons being significantly lower than that of pions. As for the pions well measured tracks were selected by requiring that all tracks have more than three hits in CZ or an endpoint in CJ.

In order to provide a good separation between pions and kaons using the measured dE/dx in the CJ detector it was necessary to select only tracks with a momentum greater than 2.0 GeV (Figure 2.6 shows that the expected dE/dx for kaons and pions are similar for momenta below 2.0 GeV). In order to select kaons the probability that a kaon would give rise to the measured dE/dx was required to be more than 0.5%. A plot of how the B_s^{**} purity[g] changes with the efficiency for different values of this cut is shown in figure 5.10.

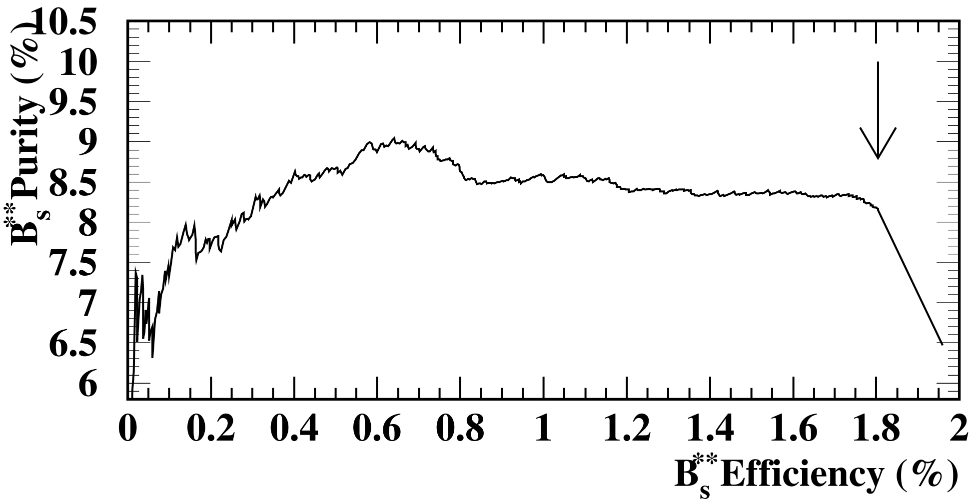

Figure 5.10: The effect of cutting on the minimum kaon dE/dx weight on the efficiency and purity for B_s^{**}'s after all other cuts.

In order to reject pions the probability that a pion would give rise to the measured dE/dx was required to be less than 4.0%. A plot of how the pion background changes

[g]Purity was measured in the Q range 0.–0.4 GeV.

for different values of this cut is shown in figure 5.11a. The cut was positioned in order to reduce the pion background to approximately 10%. A plot of how the B_s^{**} purity changes with the efficiency for different values of this cut is shown in figure 5.11b and shows that any further gains in B_s^{**} purity from this cut are limited.

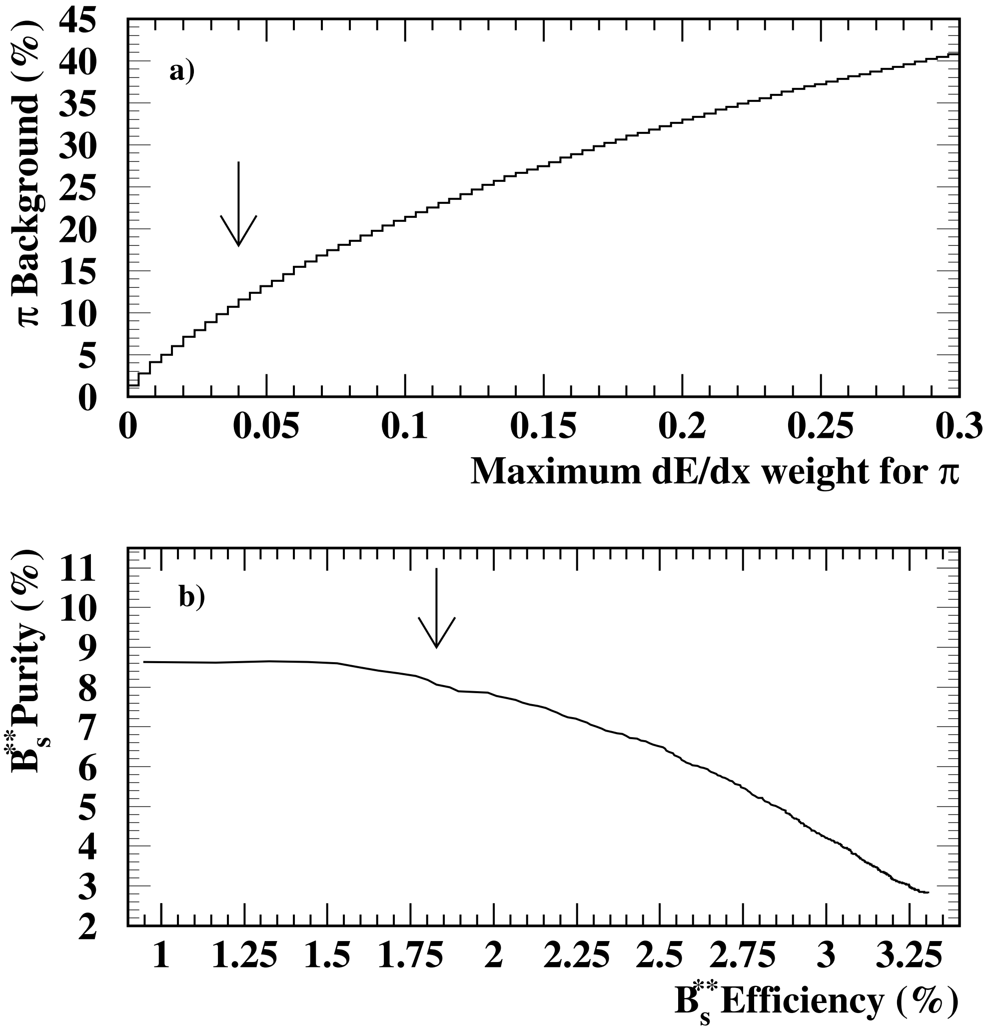

Figure 5.11: The effect of cutting on the maximum pion dE/dx weight on a) the amount of π's in the K Sample after all other cuts and b) the efficiency and purity for B_s^{**}'s.

To select candidate tracks from the primary vertex the secondary vertex weight, ω, was required to be less than 0.68. A plot of how the B_s^{**} purity changes with the efficiency for different values of this cut is shown in figure 5.12.

The momentum distributions for both signal and background tracks are shown in

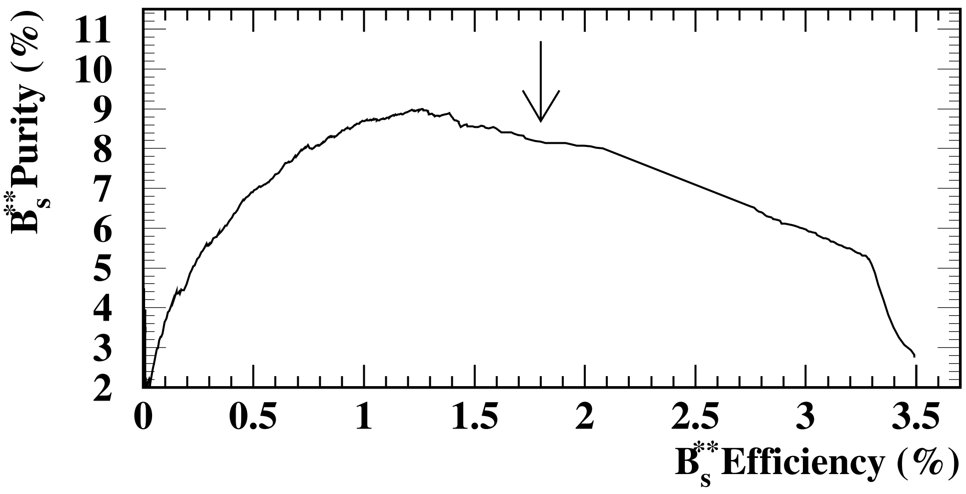

Figure 5.12: The effect of, after all other cuts, cutting on the probability that a track came from the secondary vertex on the efficiency and purity for B_s^{**}'s.

figure 5.13 showing the cut on minimum momentum at 2.0 GeV imposed in order to use dE/dx to separate pions and kaons. It can also be seen that the momentum of signal tracks are mainly less than 5.5 GeV while the background continues beyond this point, hence a cut was placed requiring track momenta to be less than 5.5 GeV. Plots of how the B_s^{**} purity changes with the efficiency for different values of the minimum and maximum momentum cuts is shown in figure 5.14. In both cases there would have been little gain in purity available by increasing the severity of the cuts.

After these cuts the sample consisted of 66.5% K, 22.8% protons and 10.7% π.

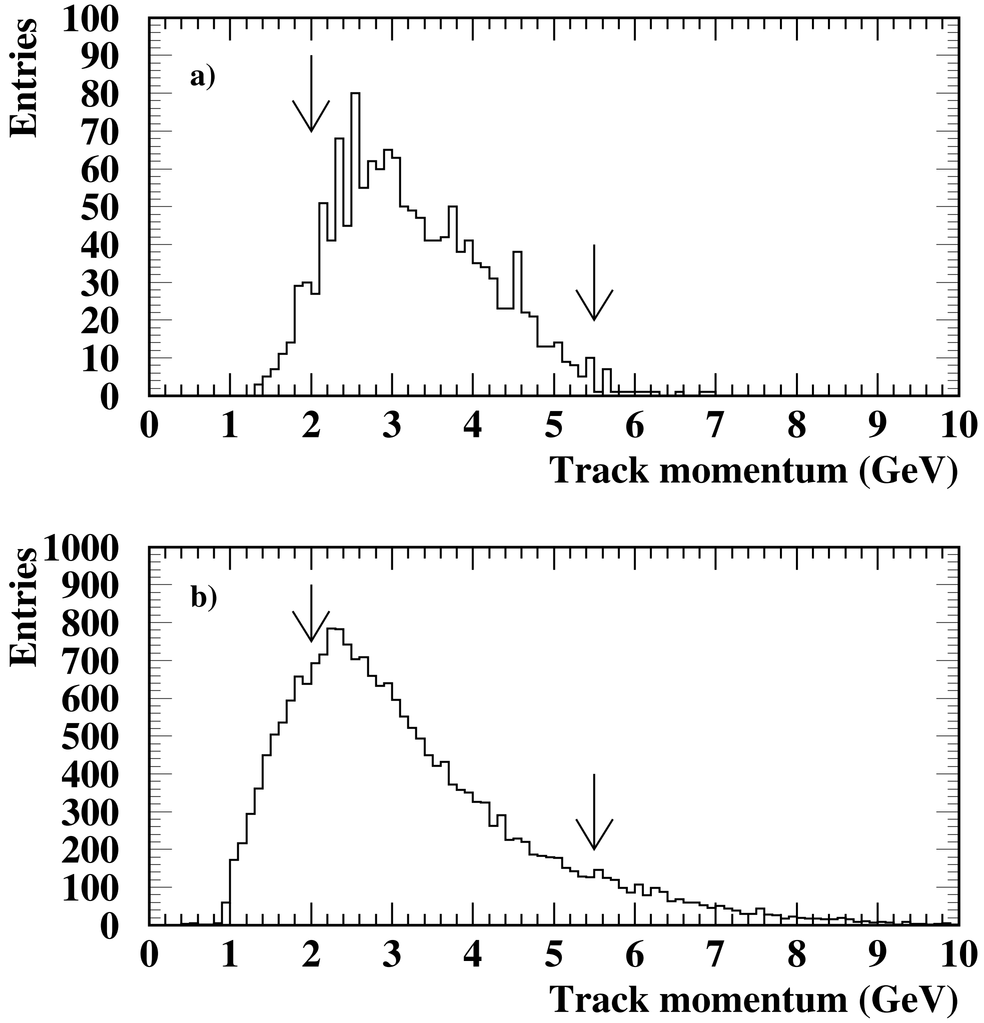

Figure 5.13: The distribution, after all other cuts, of momentum for K's a) from B_s^{**}'s and b) not from B_s^{**}'s.

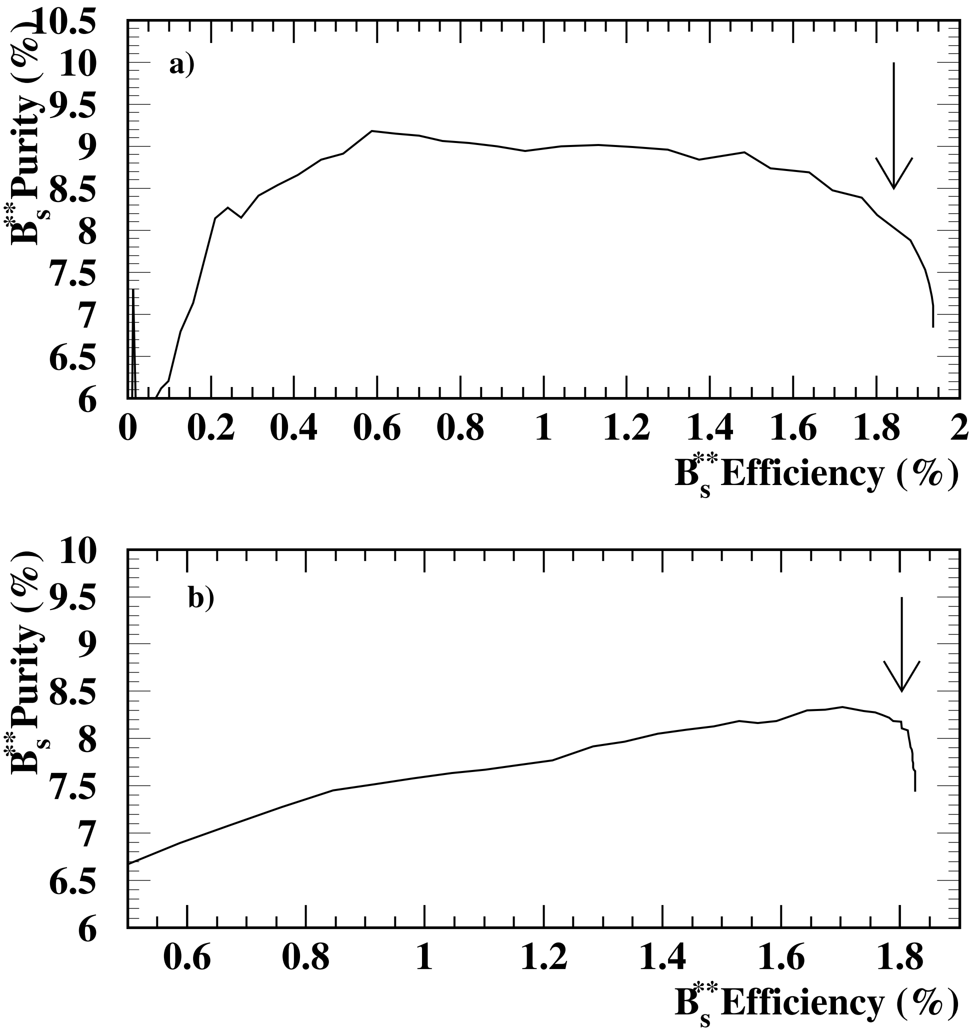

Figure 5.14: The effect of cutting, after all other cuts, on the a) the minimum and b) the maximum track momentum on the efficiency and purity for B_s^{**}'s.

5.5 Mass Resolution

Now that the sample of candidates has been selected the final mass resolution can be examined. In section 5.3.4 errors were calculated for the determination of the θ ($\sigma(\theta_{NN})$) and ϕ ($\sigma(\phi_{comb})$) directions of the B. The mass resolution will depend on any cut which is applied to these quantities. Three sets of cuts were chosen which gave the best mass resolution in the Monte Carlo for a fixed signal efficiency. Figure 5.15 shows the mass resolution measured in the Monte Carlo for no cuts and for the three choices of cuts. Table 5.2 shows the efficiency for B** along with the full width at half maximum (FWHM) and RMS of the mass resolution for these four cut choices. The cuts have little effect on the FWHM but do cause the RMS to change.

max $\sigma(\phi_{comb})$	max $\sigma(\theta_{NN})$	Efficiency	FWHM	RMS
no cut	no cut	6.4%	0.0831	0.0779
0.070	0.056	5.8%	0.0826	0.0647
0.039	0.031	3.8%	0.0822	0.0562
0.026	0.021	1.8%	0.0693	0.0474

Table 5.2: The effects of cutting on $\sigma(\phi_{comb})$ and $\sigma(\theta_{NN})$ on the B** efficiency and on the RMS and full width at half maximum (FWHM) of the resolution.

The resolution obtained with the weakest set of cuts ($\sigma(\phi_{comb}) < 0.07$ and $\sigma(\theta_{NN}) < 0.056$) has been examined further in figure 5.16. In this figure the resolutions obtained when taking all apart from one component of the analysis from the Monte Carlo input information are shown. The plots show little variation in full width however the the largest contributors to the RMS are the determination of the energy of the B and the θ of the B direction. The smallest contribution to the RMS comes from the measurement of the π momentum.

The same cuts on the errors have been applied to the BK combinations and the corresponding resolutions are shown in figure 5.17 and summarised in table 5.3. As for the Bπ combinations the contributions to the resolution for the loosest error cuts are shown in figure 5.18. In this case the largest contributions to the RMS come from the

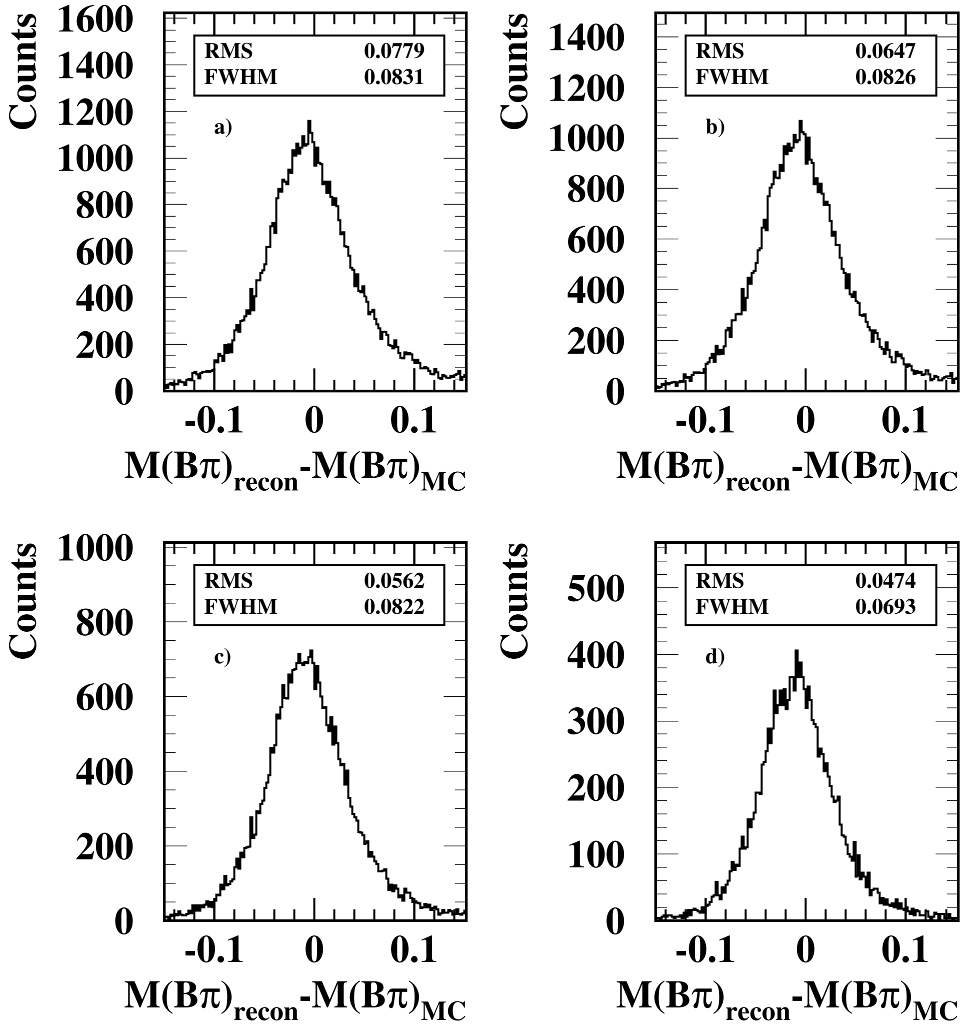

Figure 5.15: The resolutions measured in the Monte Carlo for Bπ combinations with a) no cuts on $\sigma(\phi_{comb})$ and $\sigma(\theta_{NN})$ b) $\sigma(\phi_{comb}) < 0.07$ and $\sigma(\theta_{NN}) < 0.056$ c) $\sigma(\phi_{comb}) < 0.039$ and $\sigma(\theta_{NN}) < 0.0312$ d) $\sigma(\phi_{comb}) < 0.026$ and $\sigma(\theta_{NN}) < 0.0208$.

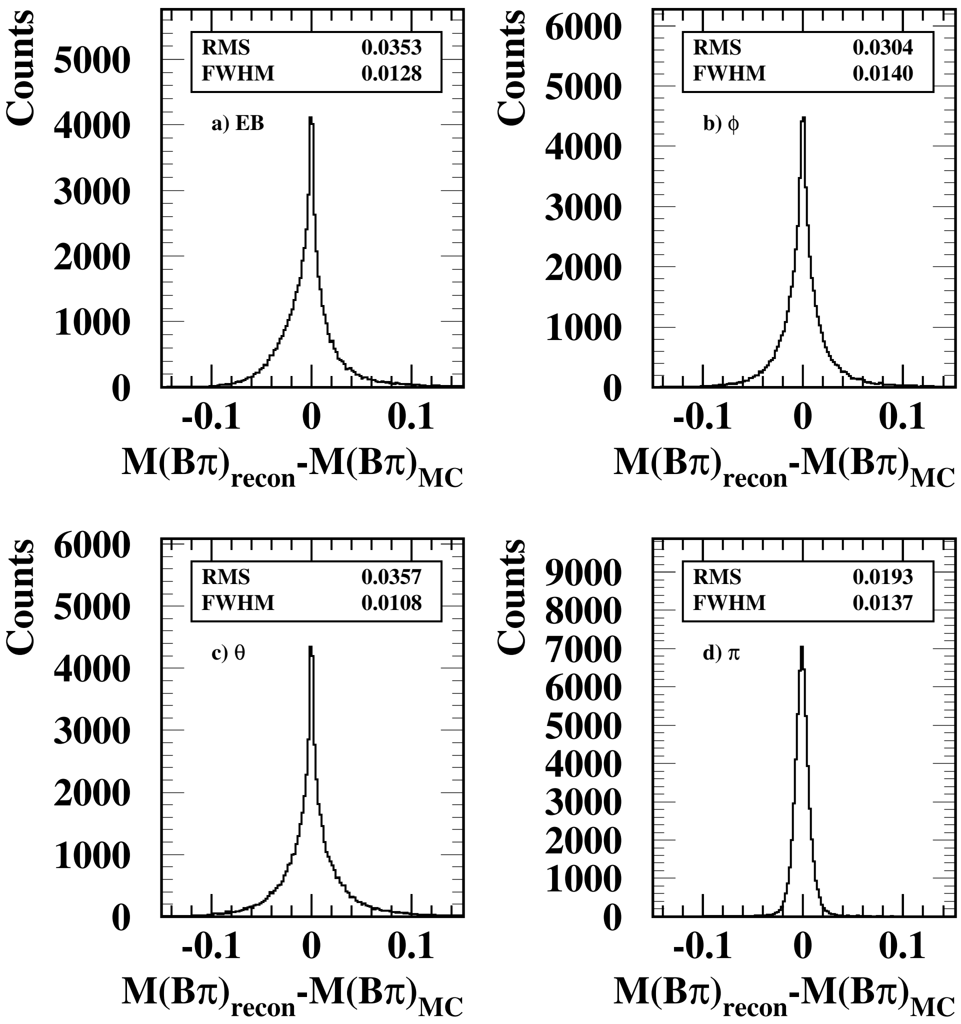

Figure 5.16: The resolution for Bπ combinations with $\sigma(\phi_{comb}) < 0.07$ and $\sigma(\theta_{NN}) < 0.056$ taking the following items from the reconstruction and the rest from MC a) Energy of the B b) The ϕ direction of the B c) the θ direction of the Band d) The π momentum.

determination of the θ and ϕ directions of the B.

max $\sigma(\phi_{comb})$	max $\sigma(\theta_{NN})$	Efficiency	FWHM	RMS
no cut	no cut	2.0%	0.0453	0.0434
0.070	0.056	1.8%	0.0441	0.0395
0.039	0.031	1.3%	0.0436	0.0335
0.026	0.021	0.7%	0.0358	0.0295

Table 5.3: The effects of cutting on $\sigma(\phi_{comb})$ and $\sigma(\theta_{NN})$ on the B_s^{**} efficiency and on the RMS and full width at half maximum (FWHM) of the resolution.

For comparison the selection efficiency of the previous OPAL work was estimated to be 0.4% for B^{**}'s and 0.2% for B_s^{**}'s so this analysis (tables 5.2 and 5.3) has a significantly higher efficiency even with the strongest set of cuts applied.

The results from DELPHI [80] in the B_s^{**} system have two peaks separated by 72 MeV. As this analysis produced a BK combination resolution with a full width in the range 36–45 MeV it should be possible to resolve these peaks in this analysis. As one aim of this analysis has been to increase the selection efficiency the weakest set of cuts listed above was chosen for use in the main analysis (i.e. $\sigma(\phi_{comb}) < 0.070$ and $\sigma(\theta_{NN}) < 0.056$).

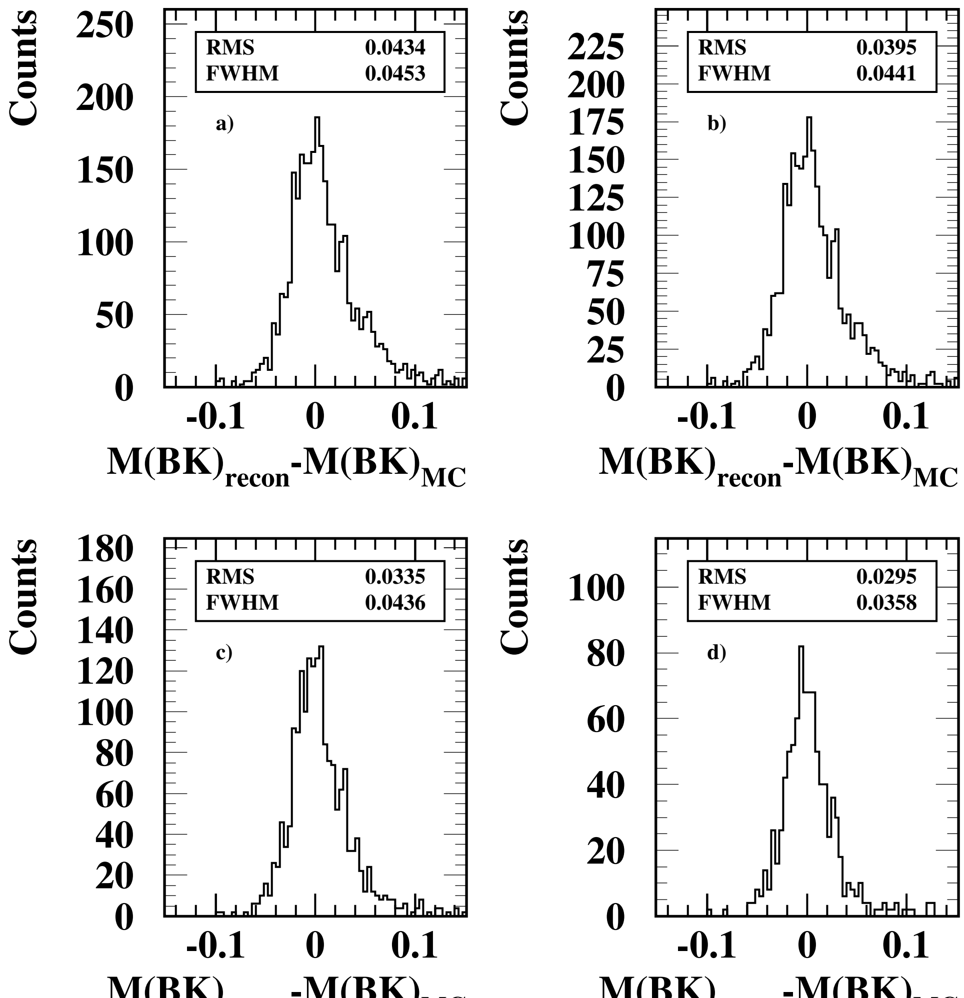

Figure 5.17: The resolutions measured in the Monte Carlo for BK combinations with a) no cuts on $\sigma(\phi_{comb})$ and $\sigma(\theta_{NN})$ b) $\sigma(\phi_{comb}) < 0.07$ and $\sigma(\theta_{NN}) < 0.056$ c) $\sigma(\phi_{comb}) < 0.039$ and $\sigma(\theta_{NN}) < 0.0312$ d) $\sigma(\phi_{comb}) < 0.026$ and $\sigma(\theta_{NN}) < 0.0208$.

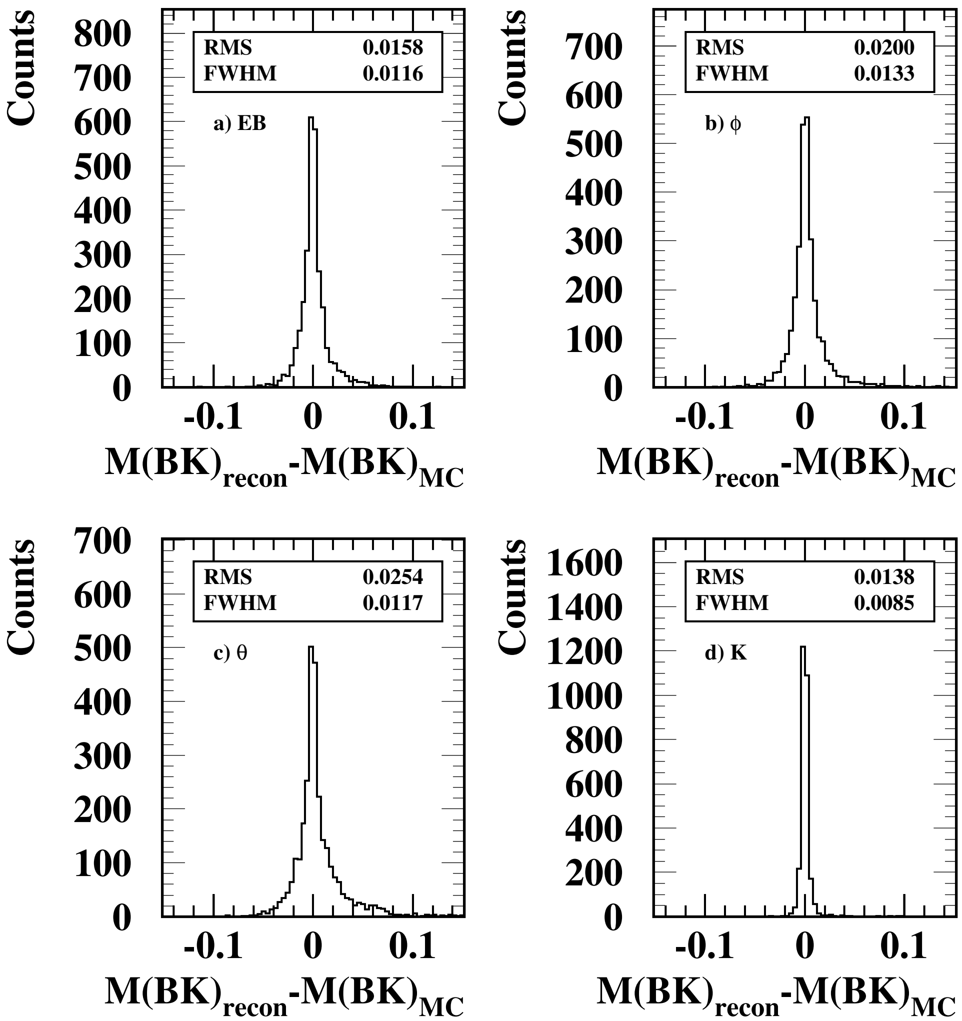

Figure 5.18: The resolution for BK combinations with $\sigma(\phi_{comb}) < 0.07$ and $\sigma(\theta_{NN}) < 0.056$ taking the following items from the reconstruction and the rest from MC a) Energy of the B b) The ϕ direction of the B c) the θ direction of the Band d) The K momentum.

Chapter 6

$B^{**}_{(s)}$ Signal Extraction

6.1 Introduction

In this chapter several background determination techniques are evaluated using Monte Carlo data. The methods which produce the best background estimate are then applied to the data to give signal peaks for both B^{**} and B^{**}_s. These signal peaks are then fitted to signal functions convoluted with the experimental resolution.

6.2 Background Determination

The main background present in this analysis is combinatorial, where the wrong π/K is selected. The shape of the background is such that it peaks near the signal peak, making it crucial that an accurate shape is obtained in order to extract reliable $B^{**}_{(s)}$ parameters.

The previous analysis by OPAL [79] used a vertex charge determination to produce a high purity sample of $B^{**}_{(s)}$. Monte Carlo was then used to subtract the remaining background. The shape of the background predicted by the Monte Carlo was checked by taking samples from the data and Monte Carlo with low signal purities and comparing them. This meant the analysis had less dependence on the Monte Carlo than other publications [77] [80] which had much lower signal purities and relied on Monte Carlo to provide the background estimate. For this analysis three different methods of obtaining a background from the data are studied. The techniques are all evaluated using Monte Carlo datasets and the most successful method for each channel is then applied to extract the signal from the data.

6.2.1 The Basic Methods

In the first method the B reconstruction is performed as normal however the tracks which are then added to the B candidate to form a possible B^{**} are taken from the other jets[a] in the event. The tracks are rotated about the primary vertex in such a way that they are at the same $\Delta\theta$ and $\Delta\phi$ to the candidate B jet as they were to their original jet.

The second method is similar to the first except that the tracks that are combined with the B are taken from other jets that passed the B selection (these tracks may therefore come from either the same or different events). This method has an advantage over method 1 in that any systematic differences between the momentum spectrum of tracks in b-tagged and untagged jets will not affect it.

The third method is taken from a recent OPAL paper on B^* production [84]. In this approach an anti b-tag is applied by reversing the cut on the output of the neural net used to select B events. This yields a sample with a lower B purity and in particular a lower B^{**} purity. The main analysis is then performed on this sample of anti-tagged jets.

6.2.2 Evaluation and Development

All the methods are evaluated using Monte Carlo samples (279x & 2776[b]). The Q-value distributions ($Q = m_{\mathrm{B}^{**}} - m_{\mathrm{B}} - m_{\pi/\mathrm{K}}$) for the estimated background produced by each method are compared to the real background predicted by the Monte Carlo. The real background is obtained by removing from the analysis any pions(kaons) that actually came from a $B^{**}(B_s^{**})$. Unless otherwise noted normalisation of the backgrounds has

[a] There may be more than two jets in an event

[b] see section 2.2.11)

been performed in the tails of the distributions. For the B^{**} study the range used was $0.7 < Q < 1.5$, while for the B_s^{**} study the range $0.4 < Q < 1.5$ was used.

6.2.2.1 Method 1

The reconstructed Q distribution of the π(K)B combinations are shown in figure 6.1, with the contributions from signal and background indicated. The estimated background shape, indicated by the points is much flatter than the real background, giving rise to a large disagreement in both channels. This difference is probably due to differences in the momentum spectrum of tracks in b-tagged and untagged jets. Due to the very poor agreement this method was not taken any further.

6.2.2.2 Method 2

Figure 6.2 shows the background estimates produced by using this method for both the B^{**} and B_s^{**} analyses. It can be seen that there is a major improvement over method 1 for both the B^{**} and B_s^{**} background, but the background is now over estimated in the signal region. This was found to be due to the fact that π(K) tracks from a $B_{(s)}^{**}$ in the other jet still form a mass peak when combined with the new B candidate. If these tracks were removed the agreement was much improved. In order to reduce the correlations between the momentum of a track and its angle to the B the candidate tracks to be combined with the B are smeared in both θ and ϕ[c]. This smearing caused the agreement between the estimated and real backgrounds to become very bad with a much flatter estimated shape. To improve the agreement the distributions of the smeared candidate track's polar and azimuthal angles to the B (θ_{B} and ϕ_{B}) are independently reweighted to the distribution found before any background method is applied[d]. This results in the estimated backgrounds shown in Figure 6.3. The agreement for the B_s^{**} analysis is now much improved, however the B^{**} case still has a very poor agreement with a much flatter shape than the real background.

In a further attempt to improve the background estimate the smearing and re-

[c] standard OPAL coordinates
[d] i.e. this includes both signal and background.

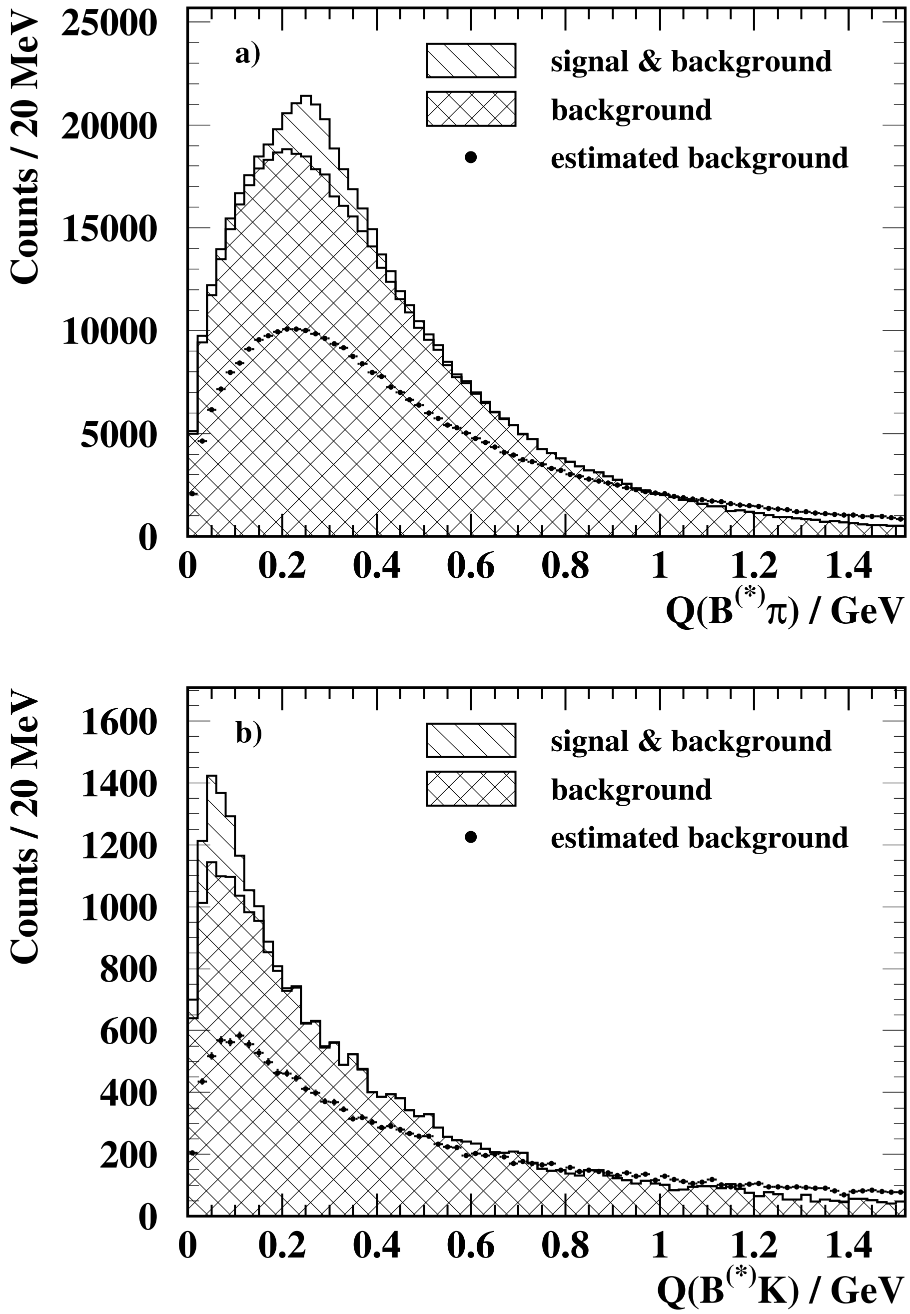

Figure 6.1: Comparison of the real Background in Monte Carlo and the estimated background given by method 1 for a) B^{**} and b) B_s^{**}.

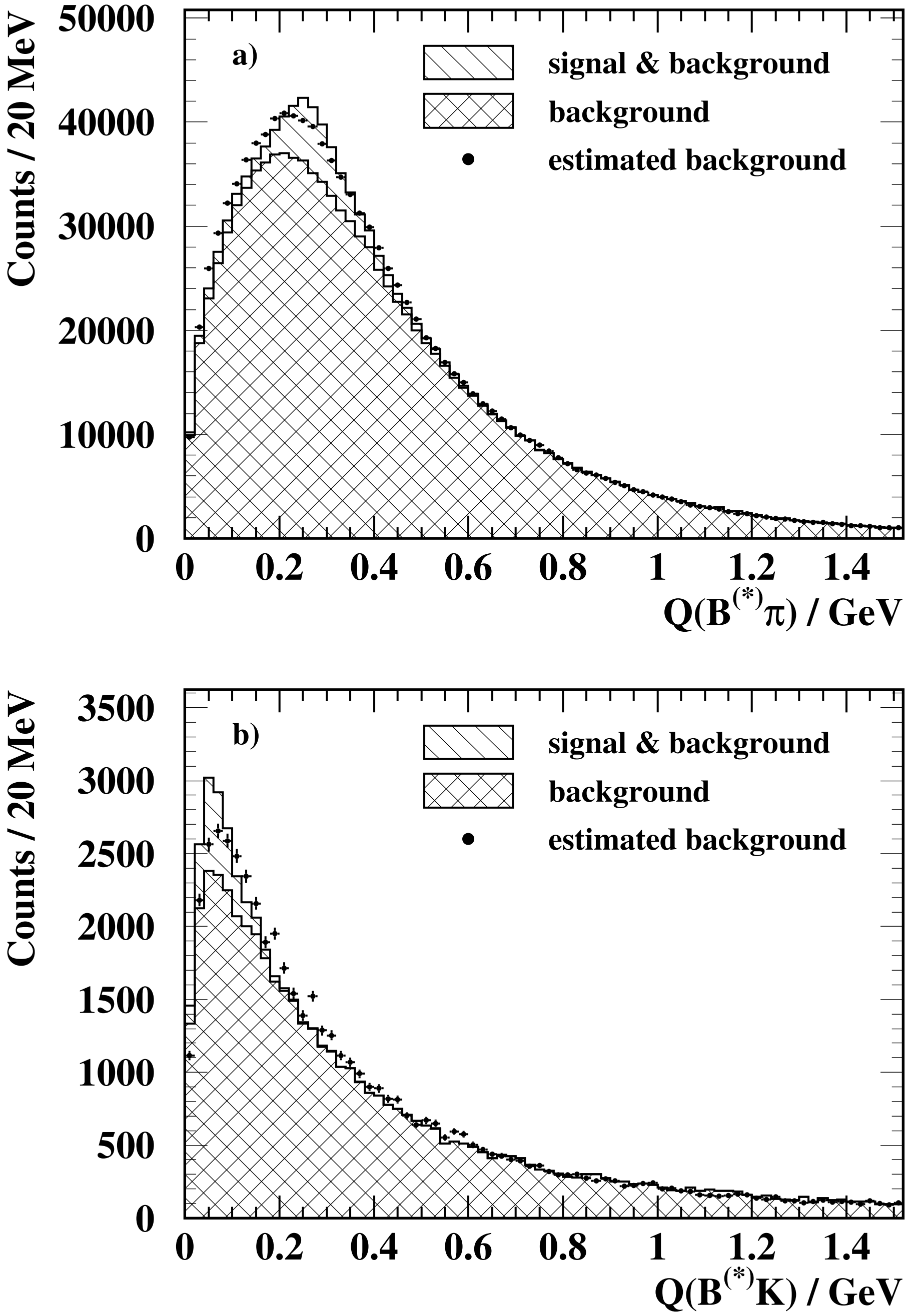

Figure 6.2: Comparison of the real Background in Monte Carlo and the estimated background given by method 2 for a) B^{**} and b) B_s^{**}.

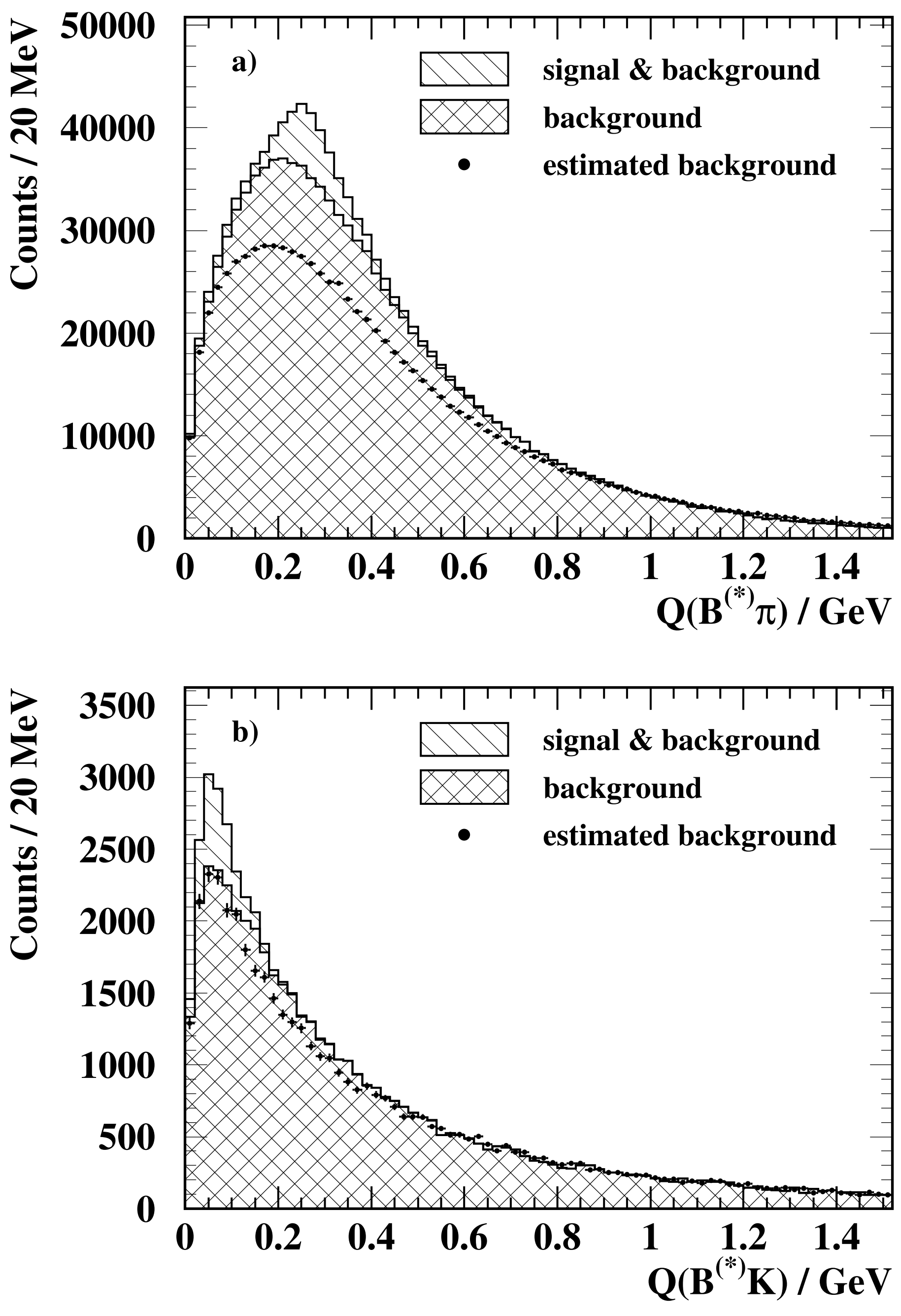

Figure 6.3: Comparison of the real Background in Monte Carlo and the estimated background given by smeared and reweighted method 2 for a) B^{**} and b) B_s^{**}.

weighting is tried using the variables $P\theta$ and $P\phi$ (P is the track momentum) which are more closely related to the final B** mass. The smearing used is

$$\begin{aligned} P\theta_{new} &= P\theta_{old} + 0.1\overline{P}x_1 \\ P\phi_{new} &= P\phi_{old} + 0.1\overline{P}x_2 \end{aligned} \tag{6.1}$$

where x_1 and x_2 are independent random numbers with a Gaussian distribution, with a mean of zero and a width of one. $\overline{P}$ (average track momentum) was measured to be 1.5 for the pion selection and 3.2 for the kaon selection. Figure 6.4 shows the background estimates obtained by using this method. As before the B** background distribution is in poor agreement with the real background while the B$_s^{**}$ distributions appear slightly improved when compared to that obtained when smearing on just θ and ϕ (figure 6.3). This can be seen more easily in Figure 6.5, which shows the ratio of the real to the estimated background for the two different smearing methods. The second version produces a flatter distribution particularly in the range $0.1 < Q < 0.4$.

In an attempt to see why this method works well for B$_s^{**}$ and not B** the distributions of θ_B, ϕ_B and the spatial angle to the B have been examined. The θ_B and ϕ_B distributions showed good agreement with the real values after the smearing and reweighting (on $P\theta$ and $P\phi$) has been performed. However the distribution of the spatial angle to the B shown in figure 6.6 shows good agreement for the B$_s^{**}$ but large differences for the B** case. The distribution of the angle in the real background shows a step at 0.65 which is caused by the cone jet algorithm[e], however neither the smeared nor reweighted distributions show this step.

The effects of taking a distribution with a cut-off in it and then smearing and reweighting two variables related to the original has been investigated in a simple Monte Carlo study. Two Gaussian distributed random numbers x and y were generated and the quantity $r = \sqrt{x^2 + y^2}$ formed. This r was then required to be less than a variable cut-off point, $r_{\max}$. The variables x and y were then smeared and reweighted and the resulting r distribution is shown in figure 6.7 for three values of $r_{\max}$. It can be seen that, as $r_{\max}$ is reduced, large problems are found around the cut-off value, and

[e]The cone algorithm was used with a maximum allowed jet half angle of 0.65.

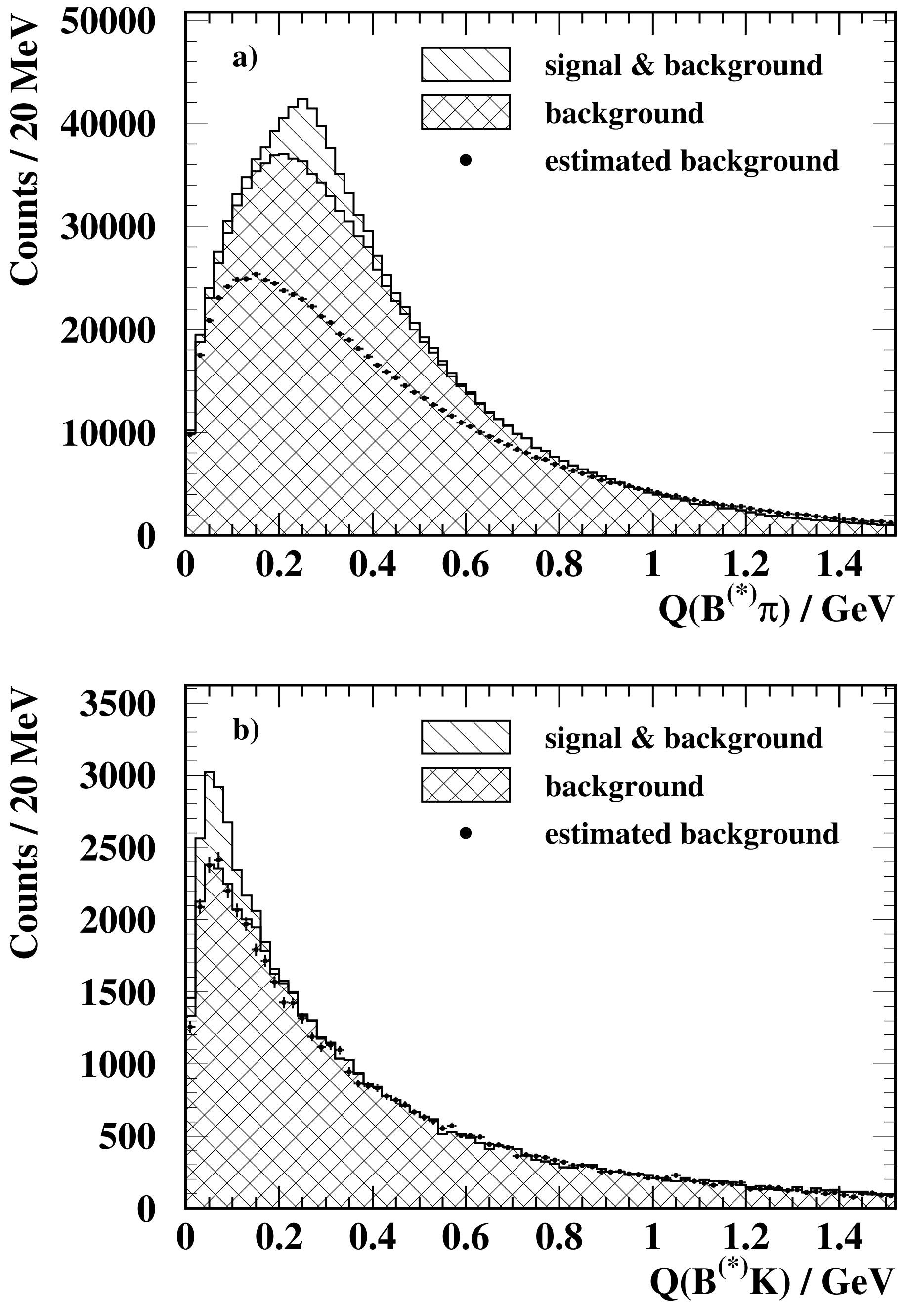

Figure 6.4: Comparison of the real Background in Monte Carlo and the estimated background given by smeared and reweighted (inc p) method 2 for a) B^{**} and b) B_s^{**}.

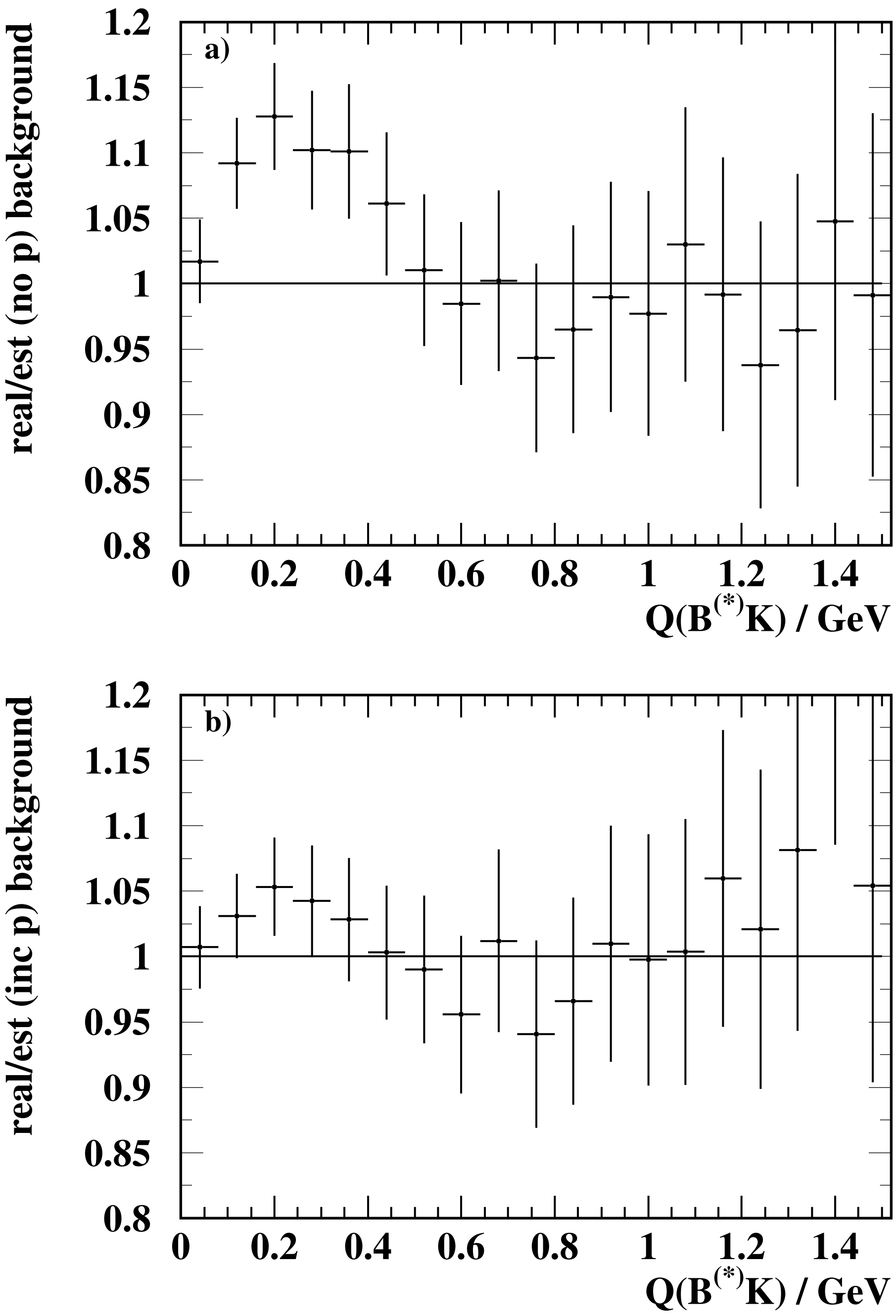

Figure 6.5: Comparing the backgrounds obtained when the smearing and reweight is performed a) without momentum and b) including momentum.

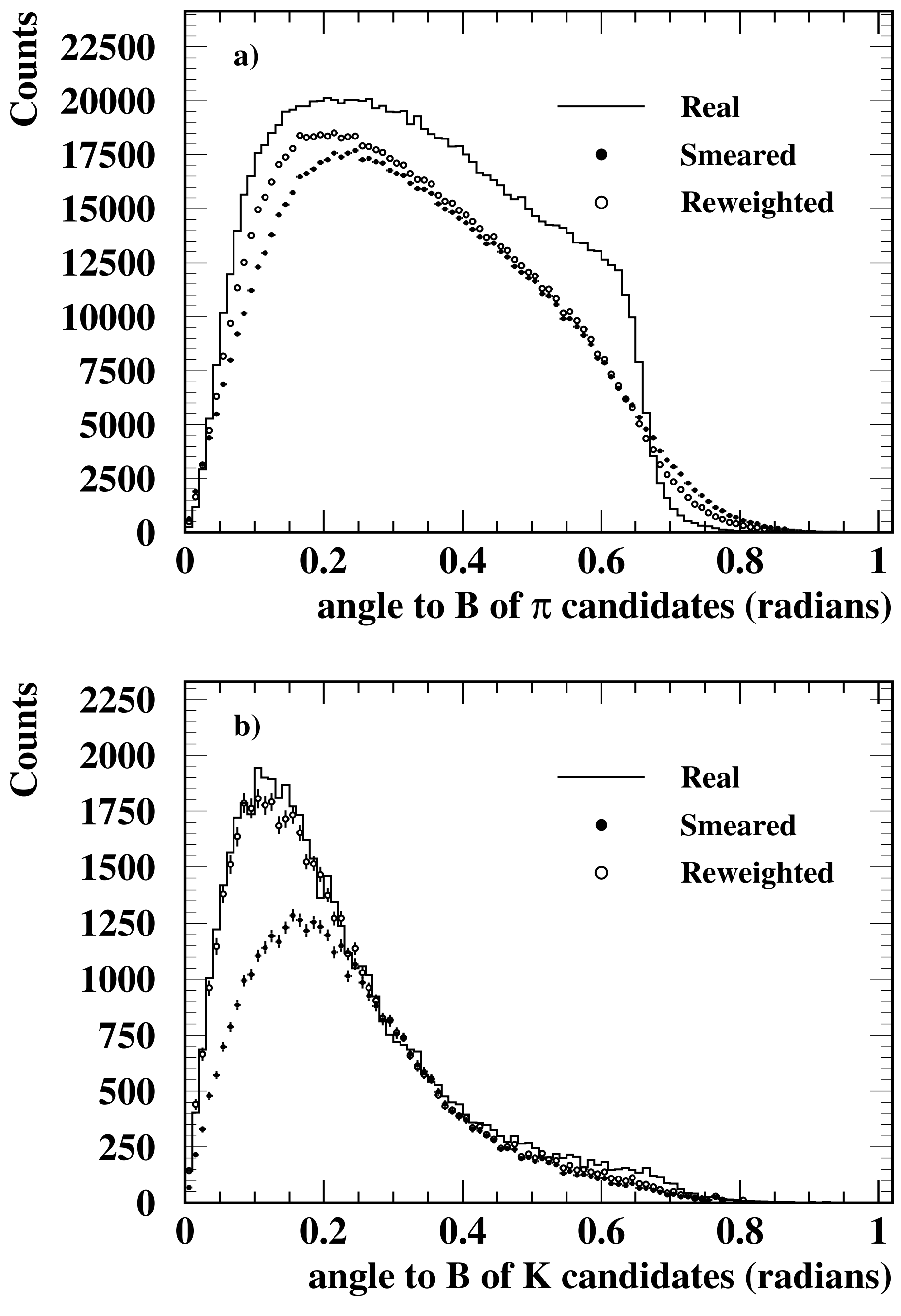

Figure 6.6: Comparison of the distribution of the spatial angle of the π(K) to the B for the real background and that found using Method 2 after smearing and then after reweighting (inc p) for a) B^{**} and b) B_s^{**}. These plots are normalised using the standard regions of the related Q distributions.

discrepancies at small r are also observed.

Method two provides a good background estimate for the B_s^{**} analysis because the distribution of the angle of the K to the B is concentrated at smaller angles than that of the π to the B in B^{**} events and is largely unaffected by the cone jet algorithm cut at 0.65 radians.

6.2.2.3 Method 3

This method is aimed at reducing the number of B^{**} in the background estimate, by reducing the b purity of the sample. The reversal of the b-selection neural network cut causes the number of tracks in the sample that originate from b-events to fall from $\simeq 90\%$ to $\simeq 45\%$. This still relatively high b purity is due to the requirement that a secondary vertex is found in the jet before the anti-tag selection is made. However the reduction in the $B_{(s)}^{**}$ contribution is significant and is shown as a function of Q value in figure 6.8[f], for both B^{**} and B_s^{**}.

The backgrounds obtained using method three are shown in figure 6.9. It can be seen that there is relatively good agreement for the B^{**} with a slight excess in the signal region. Very poor agreement is seen for the B_s^{**} background with a large excess at low Q.

The distribution of the spatial angle between the π(K) and the B for both the real and estimated background has been studied and is shown in figure 6.10. The agreement between the real and estimated background for the B^{**} is much better than that found using method 2 (figure 6.6) and it reproduces quite well the step in the distribution at 0.65. The agreement for the B_s^{**} is clearly poor, having a large excess at low angles, the cause of which is not properly understood.

Reweighting the distribution of the spatial angle of the π(K) to the B was found to give no significant improvement to the background estimates, so a further attempt was made to improve these by reweighting the distribution of the quantity (momentum of track)$\times$(angle to the B) to that found for the real background and signal[g]. The

[f]Note that the lower peak ($Q < 0.15$) on figure 6.8 is due to the decay $B^{**} \to B\pi\pi$

[g]it is necessary to include the signal as this procedure will need to be performed on the data sample.

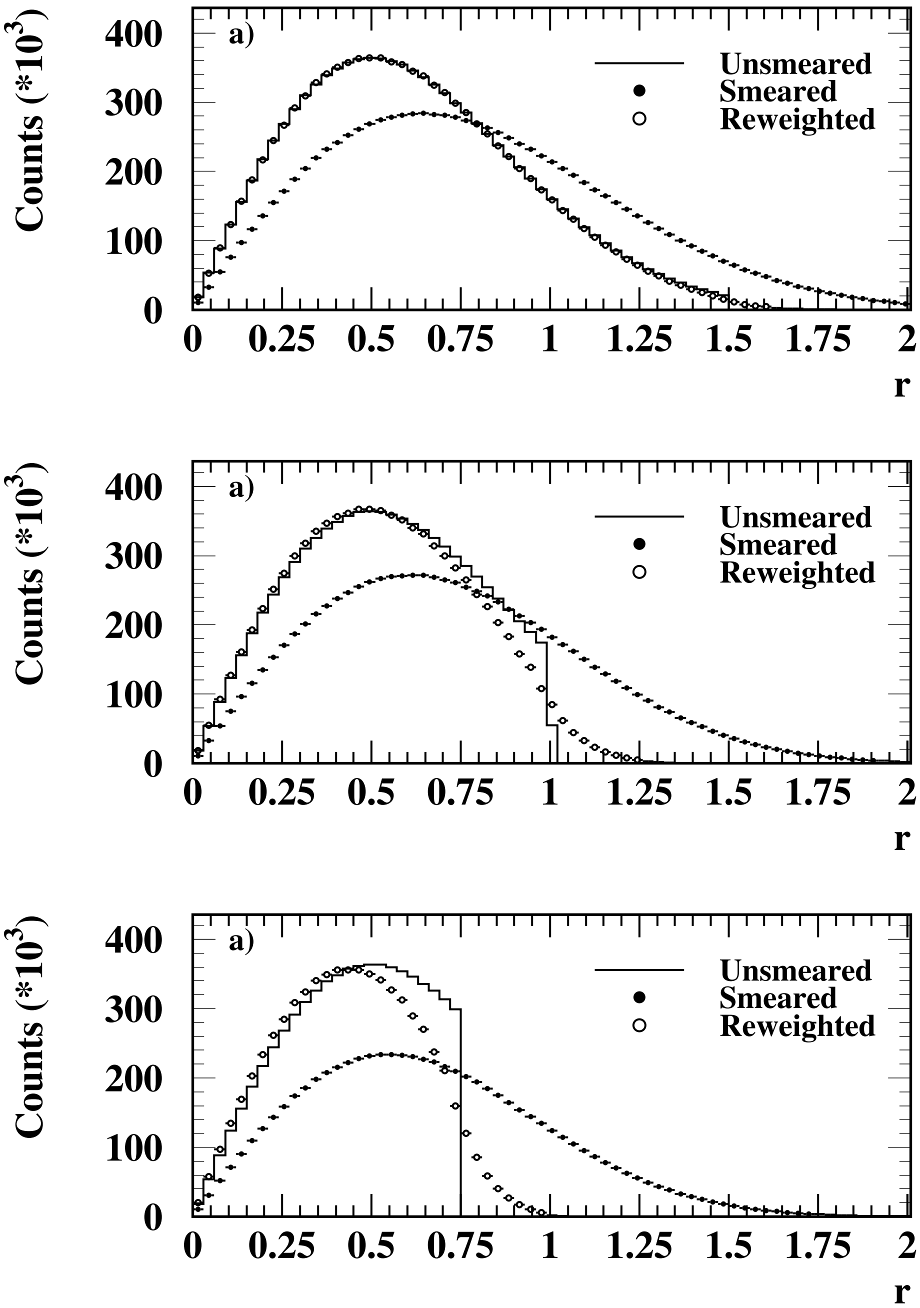

Figure 6.7: The effects of smearing and reweighting x and y on the r distribution for a) $r_{\max} < 1.5$ a) $r_{\max} < 1.0$ and c) $r_{\max} < 0.75$

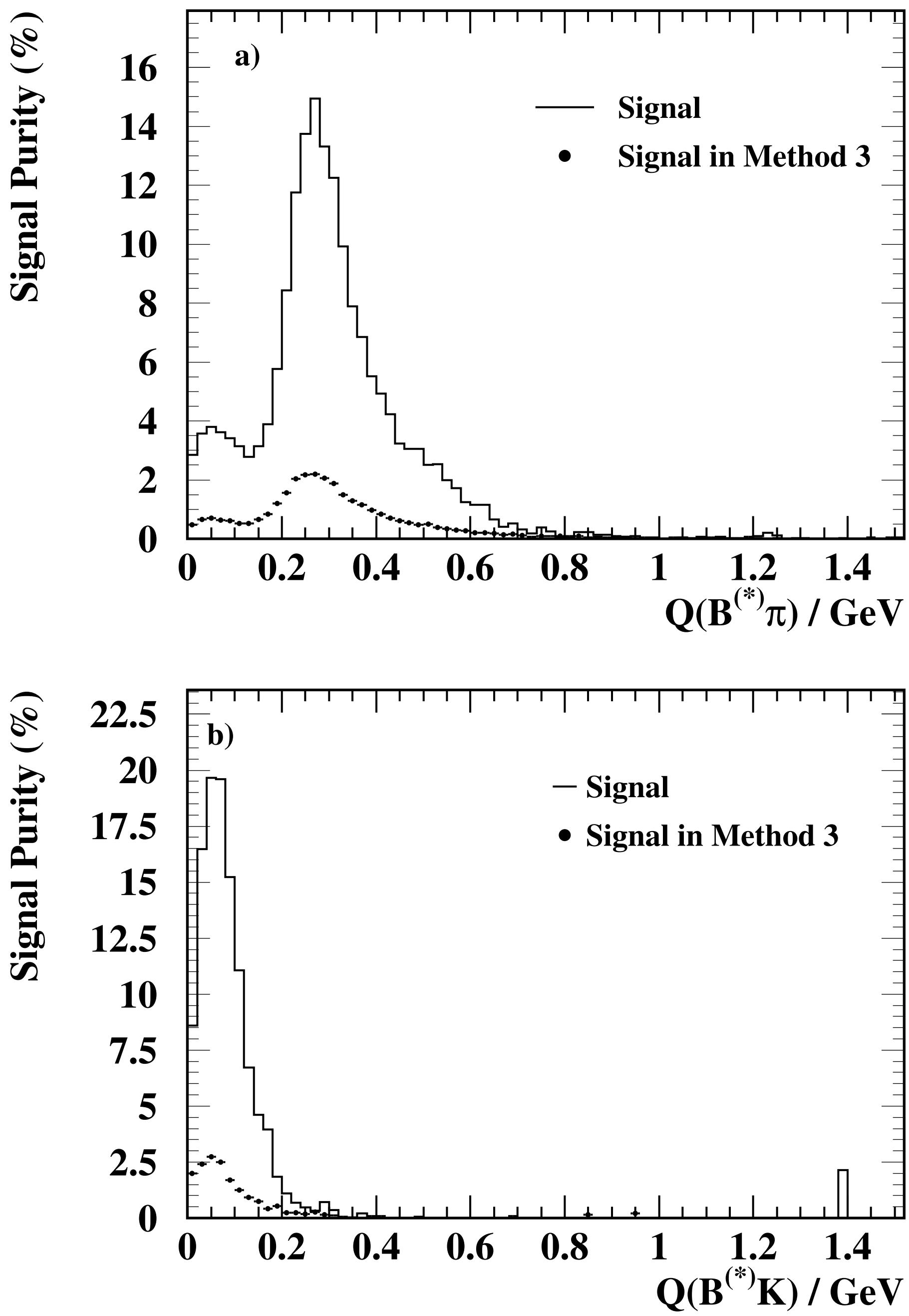

Figure 6.8: The reduction in signal purity given by method 3 for a) B^{**} and b) B_s^{**}.

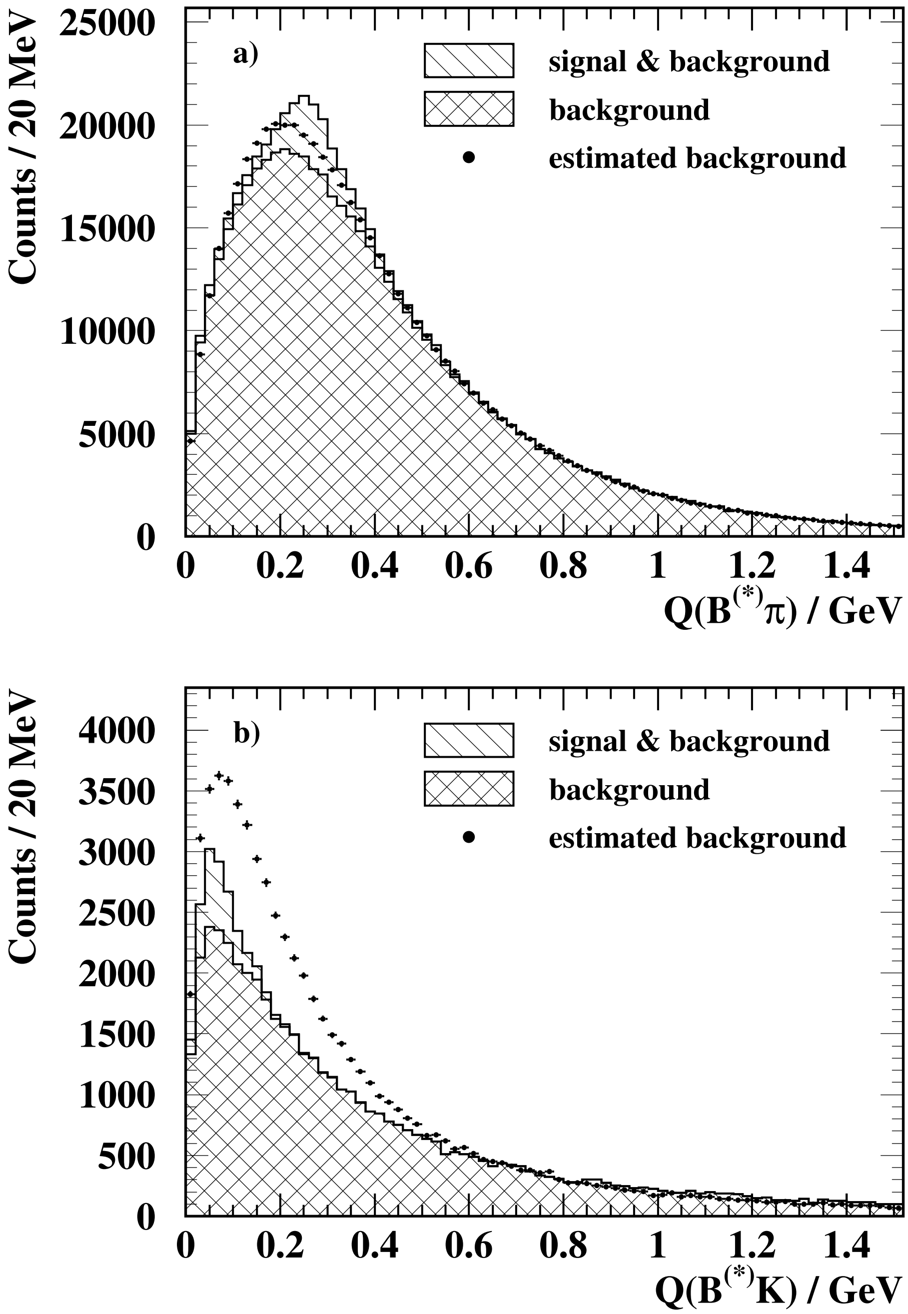

Figure 6.9: Comparison of the real Background in Monte Carlo and the estimated background given by method 3 for a) B^{**} and b) B_s^{**}.

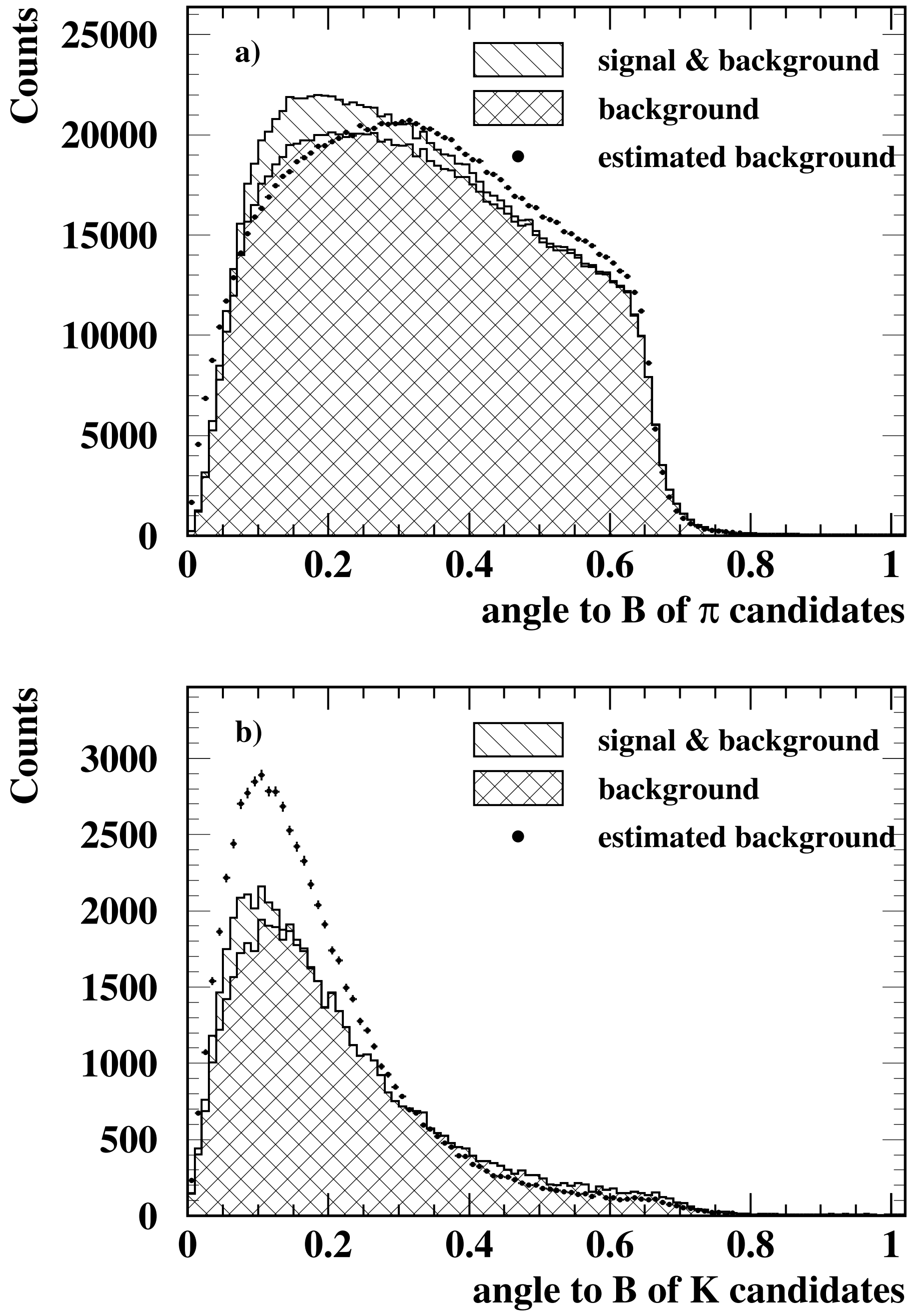

Figure 6.10: Comparison of the distribution of the spatial angle of the π(K) to the B for the real background and signal and that found using Method 3 for a) B^{**} and b) B_s^{**}. The normalisation used is the same as that used for figure 6.9.

background distributions produced with this reweighting are shown in figure 6.11. It can be seen that the B_s^{**} background estimate while improved still has a large excess in the signal region. The B^{**} background estimate has improved significantly although it is now slightly low in the signal region. This improvement can be seen more easily in figure 6.12, which shows the ratio of the real to the estimated background for the unweighted and reweighted background estimates. The reweighted version produces a flatter distribution although there is still disagreement at the level of a few percent.

6.2.2.4 Choice of Method

The best backgrounds are obtained by using method 3 (with reweighting) for the B^{**} analysis and method 2 (with smearing and re-weighting of $P_K\theta$ and $P_K\phi$) for the B_s^{**} analysis. However as the agreement between the real and estimated backgrounds is not perfect in the Monte Carlo a bin by bin correction factor is also determined by taking the ratio of the real and estimated backgrounds. These fairly small correction factors which are shown in figure 6.13 are the only input that will be taken from the MC when the backgrounds are determined from the data. These correction factors for the B^{**} background show a possible problem in the two lowest Q bins where a relatively large correction factor is needed, however this Q region contains only $B\pi$ candidates which are from the decay $B^{**} \to B\pi\pi$ well away from the B^{**} mass peak. The correction factors for the B_s^{**} background show no large deviations from unity over the Q range of the signal region.

6.2.3 Fitting the Background Shapes

Since the background shapes are expected to be smooth a function is fitted to the background and this is then subtracted from the data. The function used has the form

$$Bg(Q) = \frac{aQ^b(1 + c\exp{(dQ^e)})}{\exp{(fQ^g)}} \tag{6.2}$$

where $a - g$ are free parameters. Figure 6.14 shows how well the fits reproduce the real background[h] shapes found in the Monte Carlo. The B^{**} background shape is very well

[h]The real background is used as when the correction factors have been applied to the backgrounds calculated from the Monte Carlo they exactly match the real background.

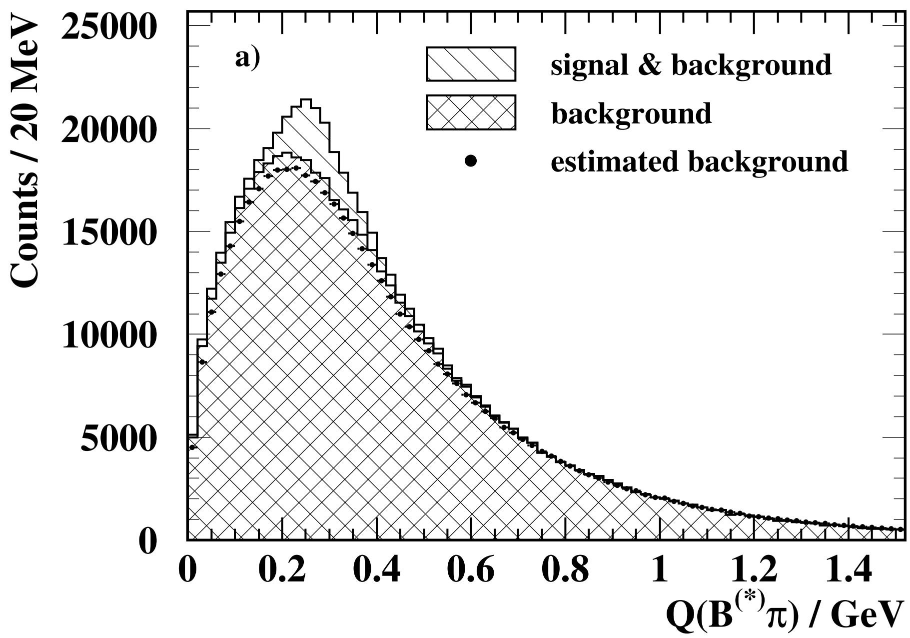

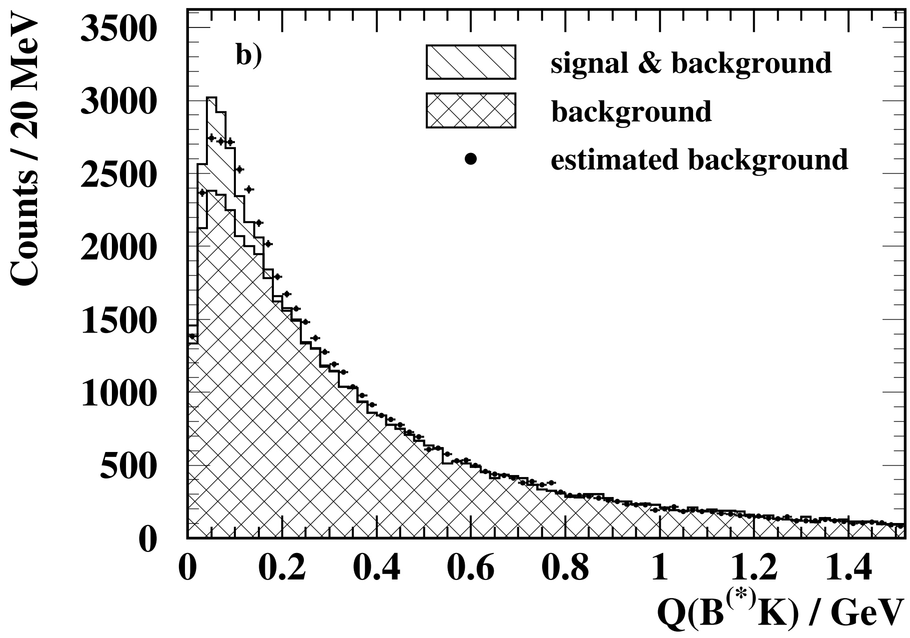

Figure 6.11: Comparison of the real Background in Monte Carlo and the estimated background given by method 3 and then reweighting the distribution of momentum*(spatial angle to the B) for a) B^{**} and b) B_s^{**}.

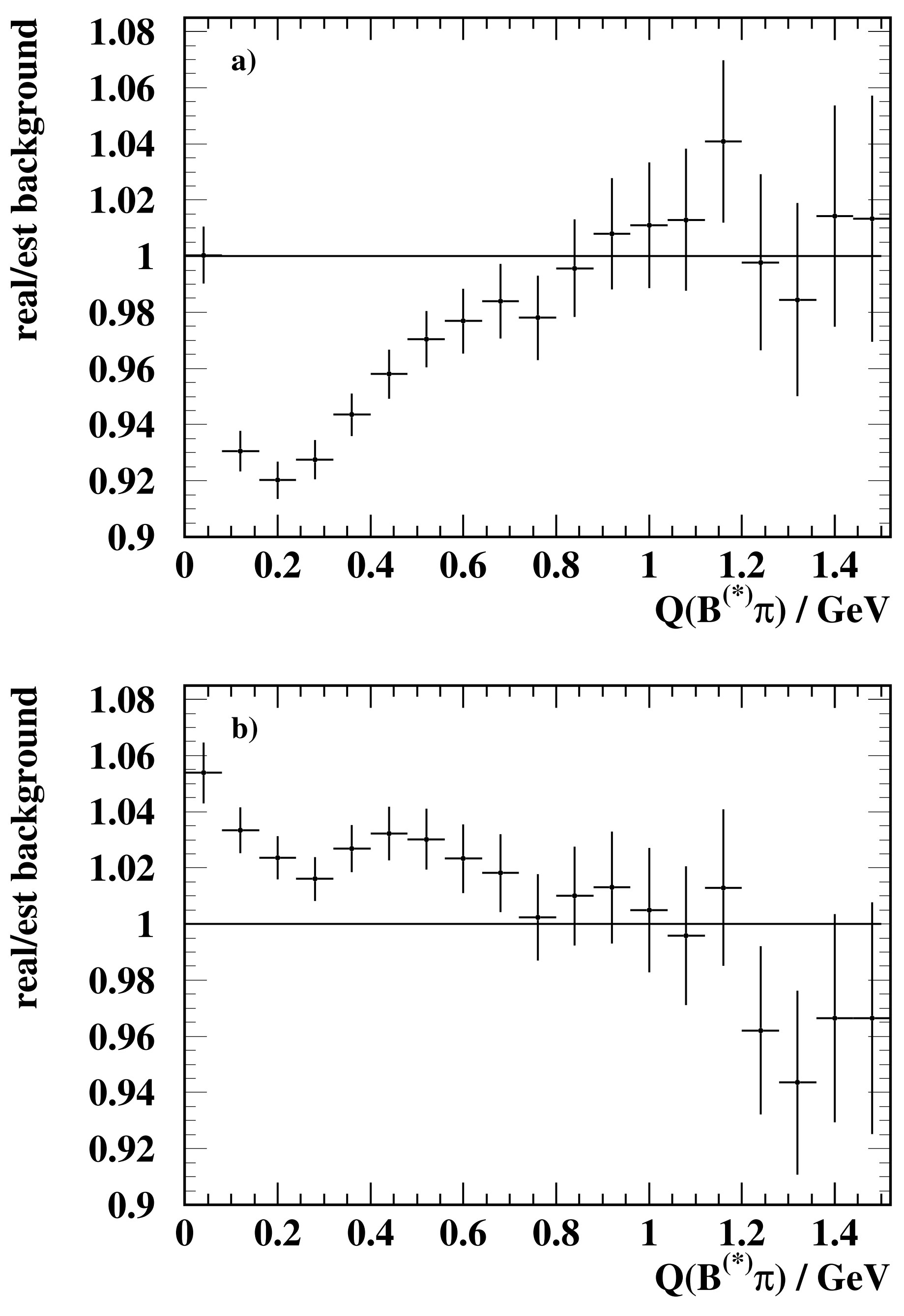

Figure 6.12: Comparing the backgrounds obtained when reweighting is a) not performed and b) performed.

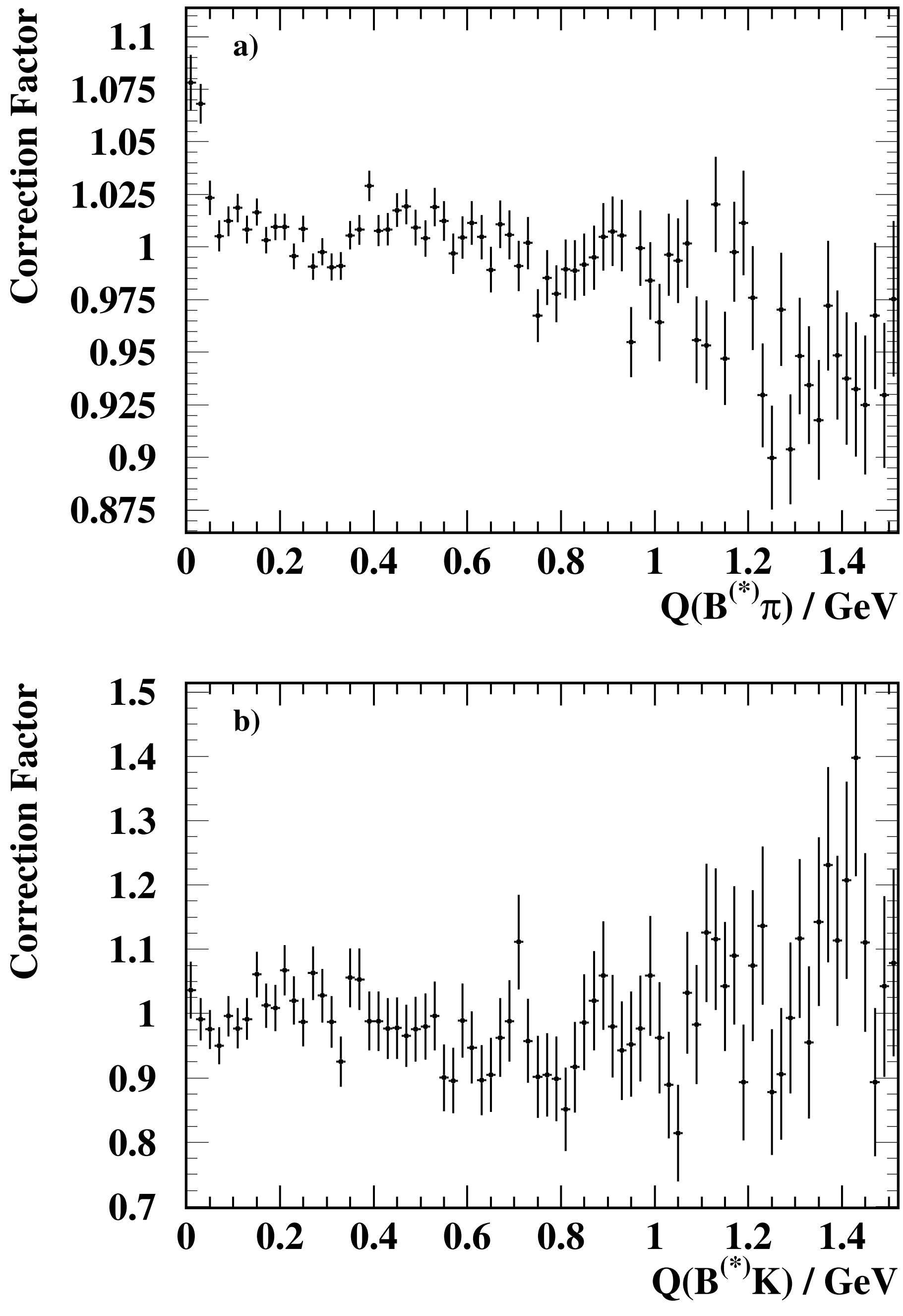

Figure 6.13: The Correction factors obtained by dividing the real background in the Monte Carlo by the estimated background in the Monte Carlo for a) B^{**} and b) B_s^{**}.

reproduced by this fit. The B_s^{**} background gives a reasonable description but there are small differences at the peak of the distribution. The results of the fits are shown in table 6.1.

Fit Parameter	B^{**} MC Fit	B^{**} Data Fit	B_s^{**} MC Fit	B_s^{**} Data Fit
a	526	1890	14.7	7.9
b	0.877	0.89	0.09	0.064
c	-0.753	-0.75	-0.983	-0.94
d	-12.9	-13.2	-7.4	-11
e	1.79	1.84	0.91	1.03
f	6.94	6.85	5.62	5.2
g	0.553	0.564	0.340	0.36
χ^2/ndf	0.92	0.96	1.05	1.04

Table 6.1: Results from fitting the background shapes found in both Monte Carlo and Data.

As a further check that this background fitting procedure is not distorting the extracted signal shape, the fitted shape for the backgrounds have been applied to the Monte Carlo. The extracted shape after background subtraction and the real signal shape are compared for B^{**} and B_s^{**} in figures 6.15 and 6.16 respectively. It can be seen that there is very good agreement between the extracted and real resonant peaks for both B^{**}[i] and B_s^{**}.

6.2.4 Background subtraction of the data

Having chosen method 3 to evaluate the B^{**} background and method 2 to evaluate the B_s^{**} background from Monte Carlo studies these methods have been applied to all OPAL data taken between 1991 and 1995 with good detector status. The background found from these data and the corresponding fits for each analysis are shown in figure 6.17. In each case the fitted curve reproduces the data well and the results of the fits are shown in table 6.1. When the parameters from the fit to the data derived background are compared to those from the fits to the Monte Carlo background it can be seen that they are quite similar (apart from parameter a which is just the normalisation of the

[i]It should be noted that the shoulder at Q values below ~ 0.15 is due to the decay $B^{**} \to B^{(*)}\pi\pi$

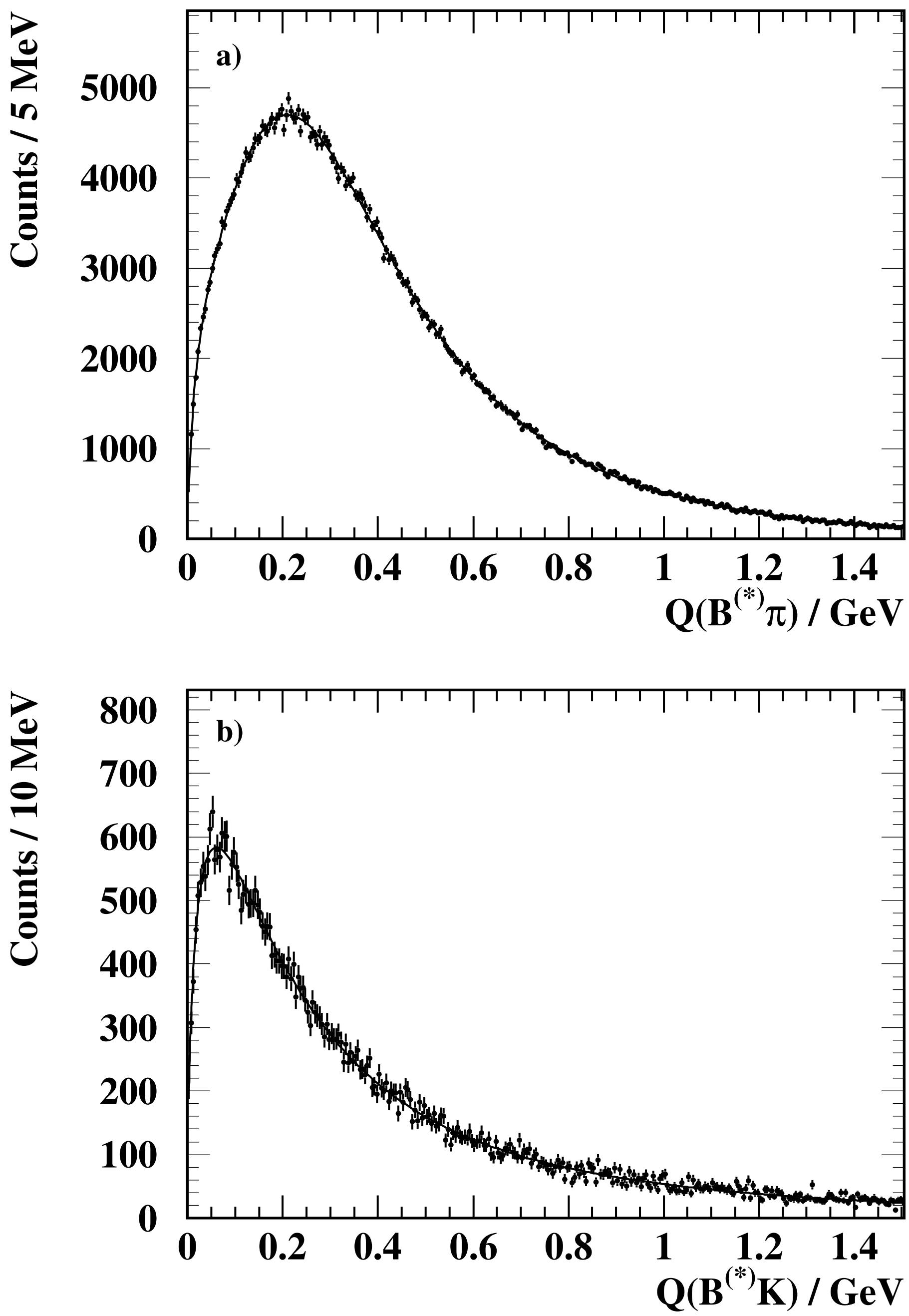

Figure 6.14: The fit to the real background shape from Monte Carlo for a) B^{**} and b) B_s^{**}.

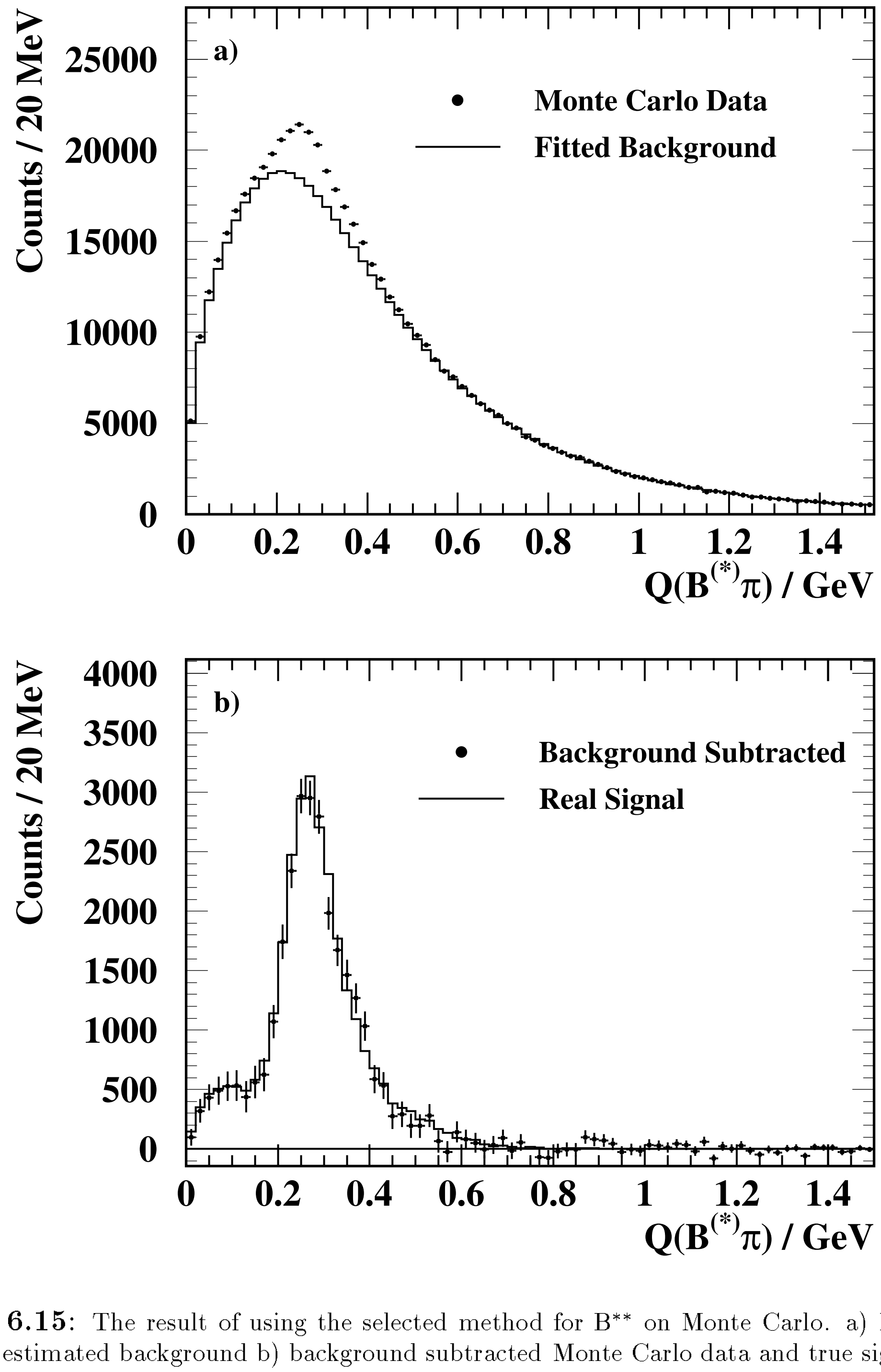

Figure 6.15: The result of using the selected method for B^{**} on Monte Carlo. a) Monte Carlo data and estimated background b) background subtracted Monte Carlo data and true signal

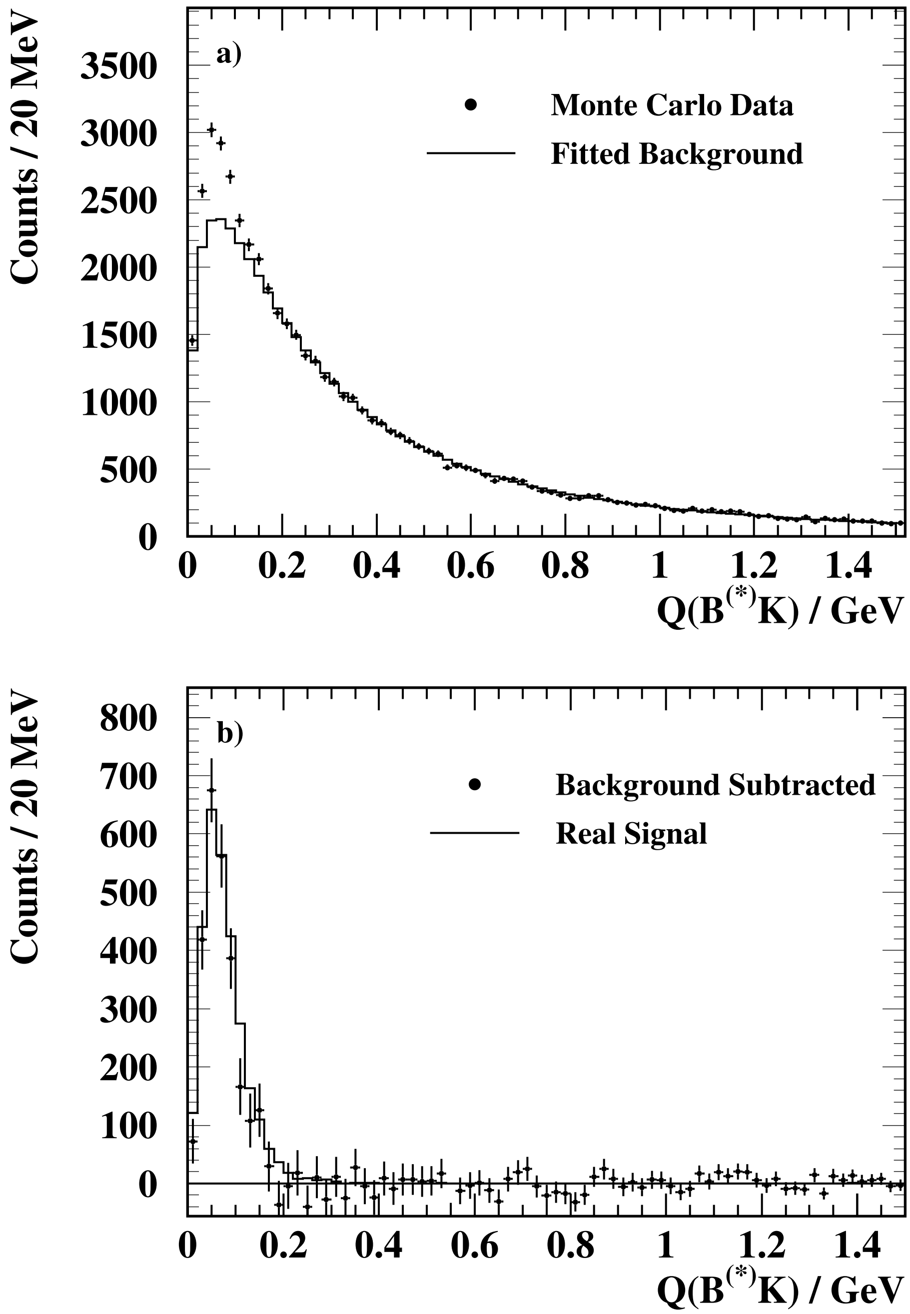

Figure 6.16: The result of using the selected method for B_s^{**} on Monte Carlo. a) Monte Carlo data and estimated background b) background subtracted Monte Carlo data and true signal

function). Now these optimised backgrounds determined from the data are used to extract the B^{**} and B_s^{**} signals from the data.

The Q distributions for the data are shown for B^{**} and B_s^{**} in figures 6.18(a) and 6.19(a) respectively along with the estimated backgrounds. These backgrounds are then applied to the data to extract the background subtracted signals shown in figures 6.18(b) and 6.19(b). The B^{**} signal is seen clearly as a large peak centred at $Q = 0.3$ with a smaller peak due to $B^{**} \rightarrow B\pi\pi$ decays also visible at $Q < 0.15$. The B_s^{**} signal is seen to be very close to threshold with a tail out to a Q of 0.25.

In order to study the stability of the extracted signal to the background estimate the fitted background from the Monte Carlo has also been applied to the data. The results of this different background subtraction are shown in figures 6.20 and 6.21. The resulting background subtracted plot for B_s^{**} (figure 6.21(b)) is very similar to that given by using the background taken from data (figure 6.19(b)). In the case of the B^{**} analysis the resulting background subtracted plot (figure 6.20(b)) shows a considerable difference to that obtained when using the background extracted from data (figure 6.18(b)). While the position of the peak is unchanged the size is much reduced, which seems to be due to the Monte Carlo predicting a lower tail to the background distribution where the normalisation is calculated ($0.7 < Q < 1.5$). This has been investigated by changing the normalisation to give a signal peak of the same height as that found when subtracting the data estimated background. The resulting background subtracted signal is shown in figure 6.22, this shows a peak which now has a very similar position and width to that found when using the data estimated background (figure 6.18(b)).

6.2.5 Background Summary

After examining three methods of obtaining background distributions from the data, working methods have been found for both B^{**} and B_s^{**}. The methods used for each case are however very different. A different sample of events is used to estimate the B^{**} background and for the B_s^{**} estimate tracks are moved from one jet to another in b-tagged events. The reasons why the methods do not both work for B^{**} and B_s^{**} are

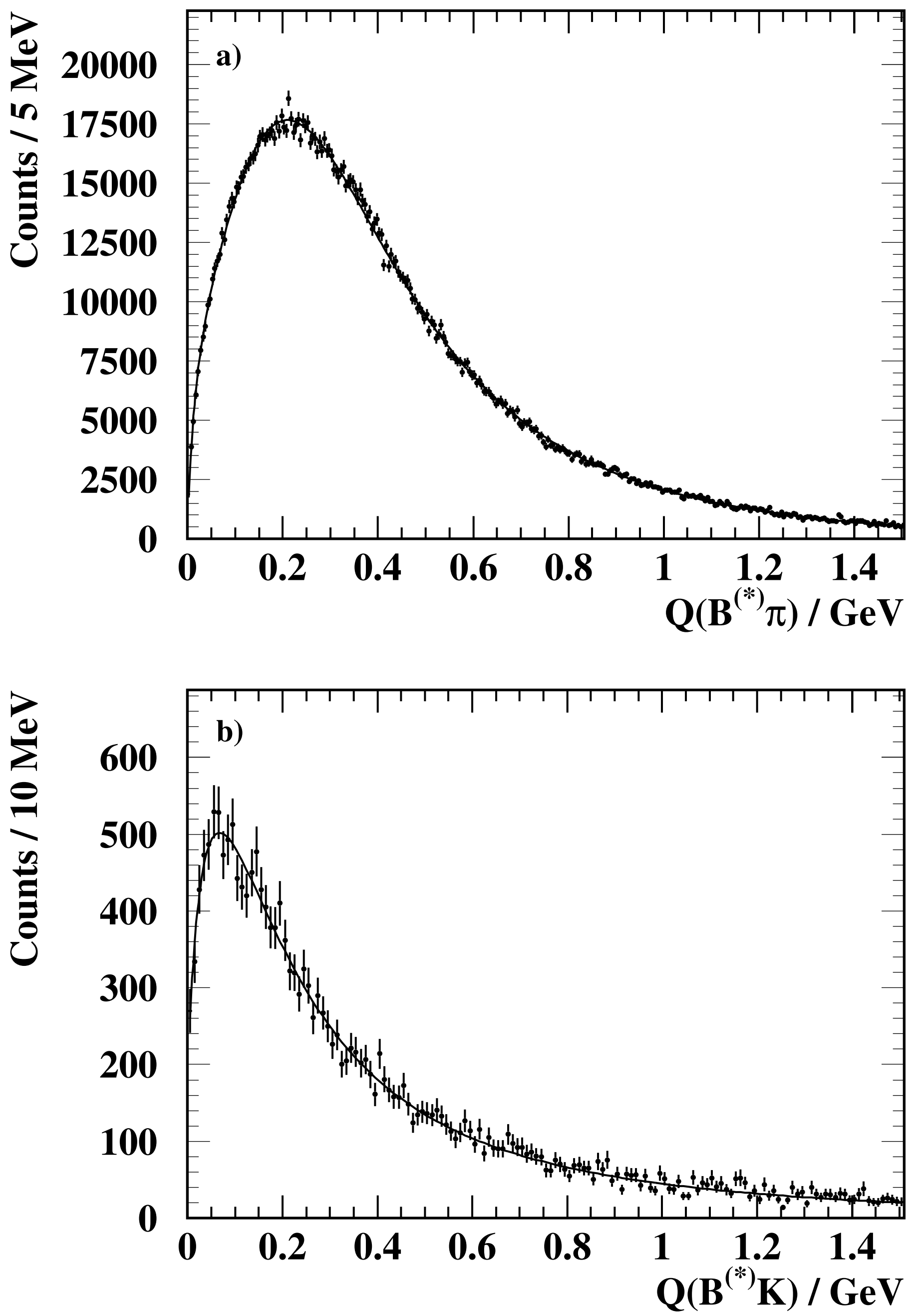

Figure 6.17: The fit to the background shape estimated from data for a) B^{**} and b) B_s^{**}.

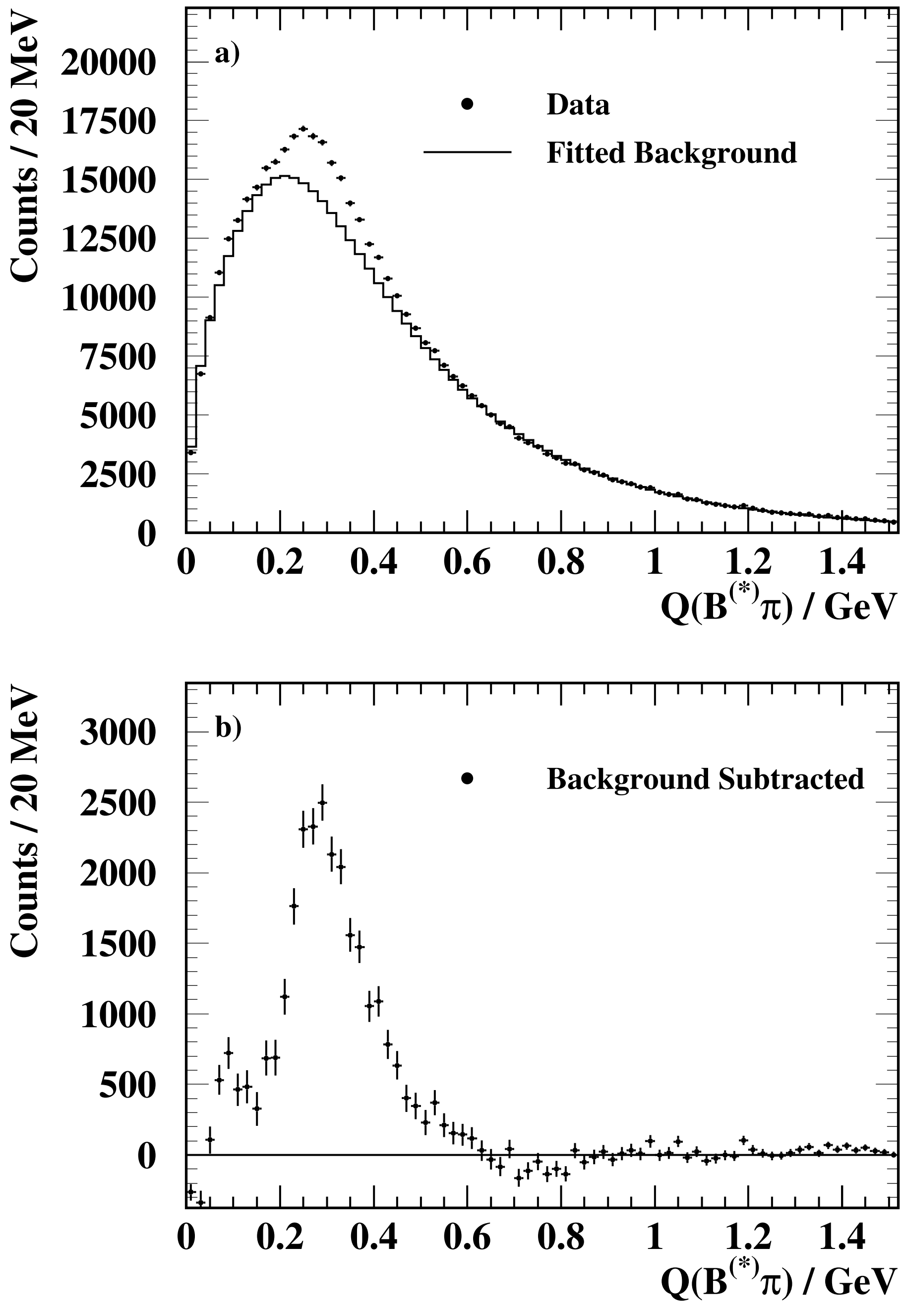

Figure 6.18: The result of using the selected method for B^{**} a) data and estimated background b) background subtracted data

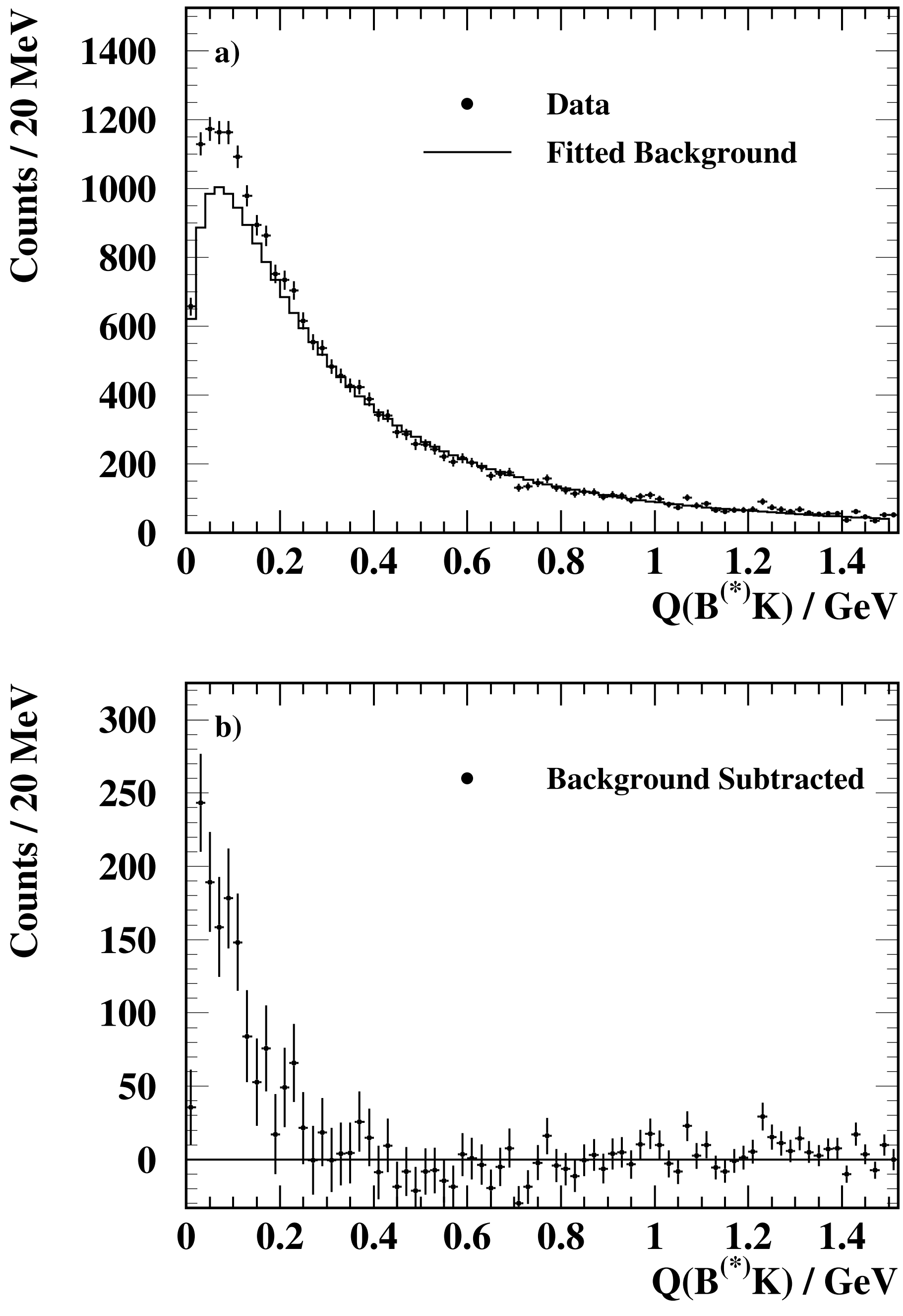

Figure 6.19: The result of using the selected method for B_s^{**} a) data and estimated background b) background subtracted data

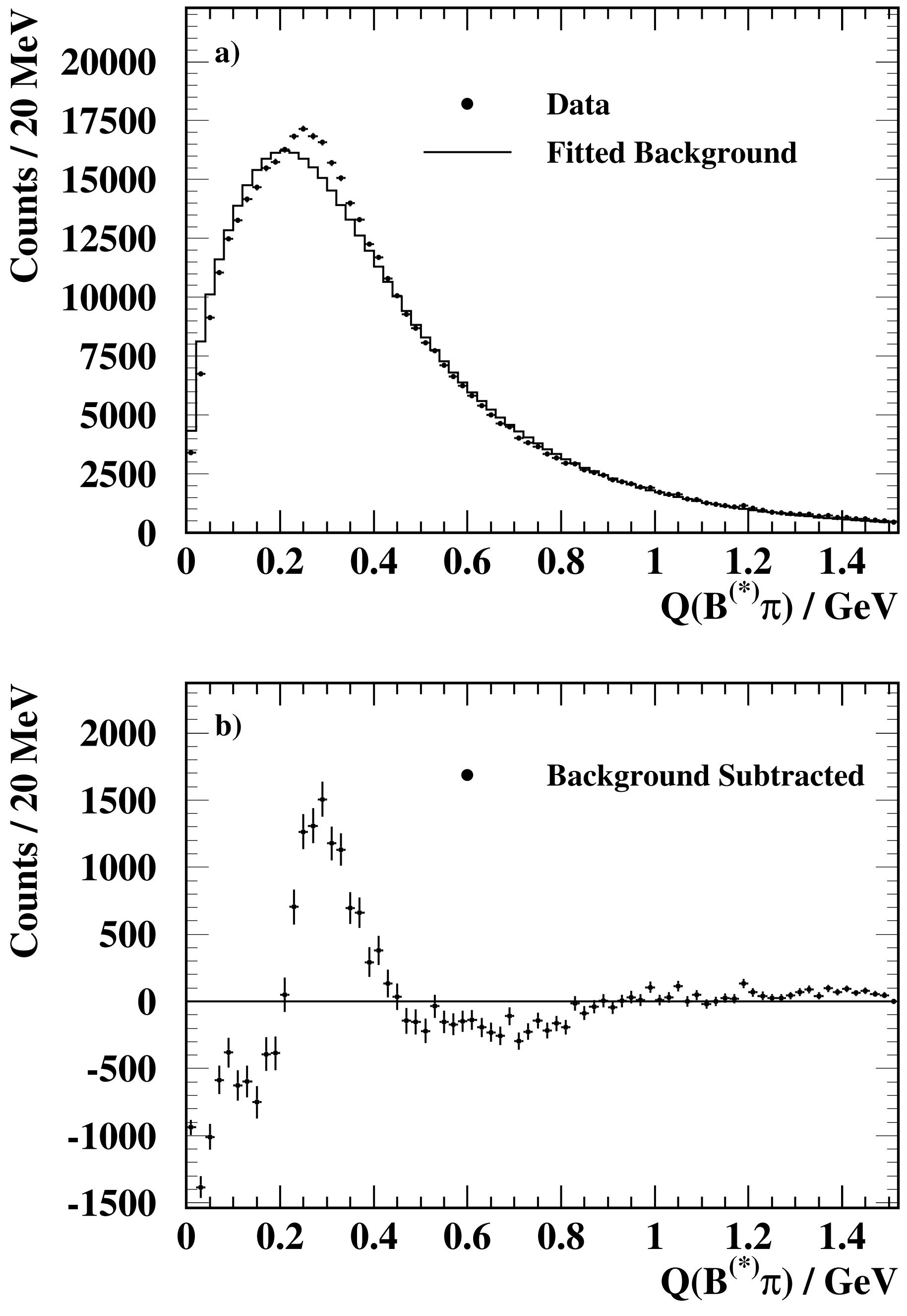

Figure 6.20: The result of using the fitted MC background shape for B^{**} a) data and estimated background b) background subtracted data

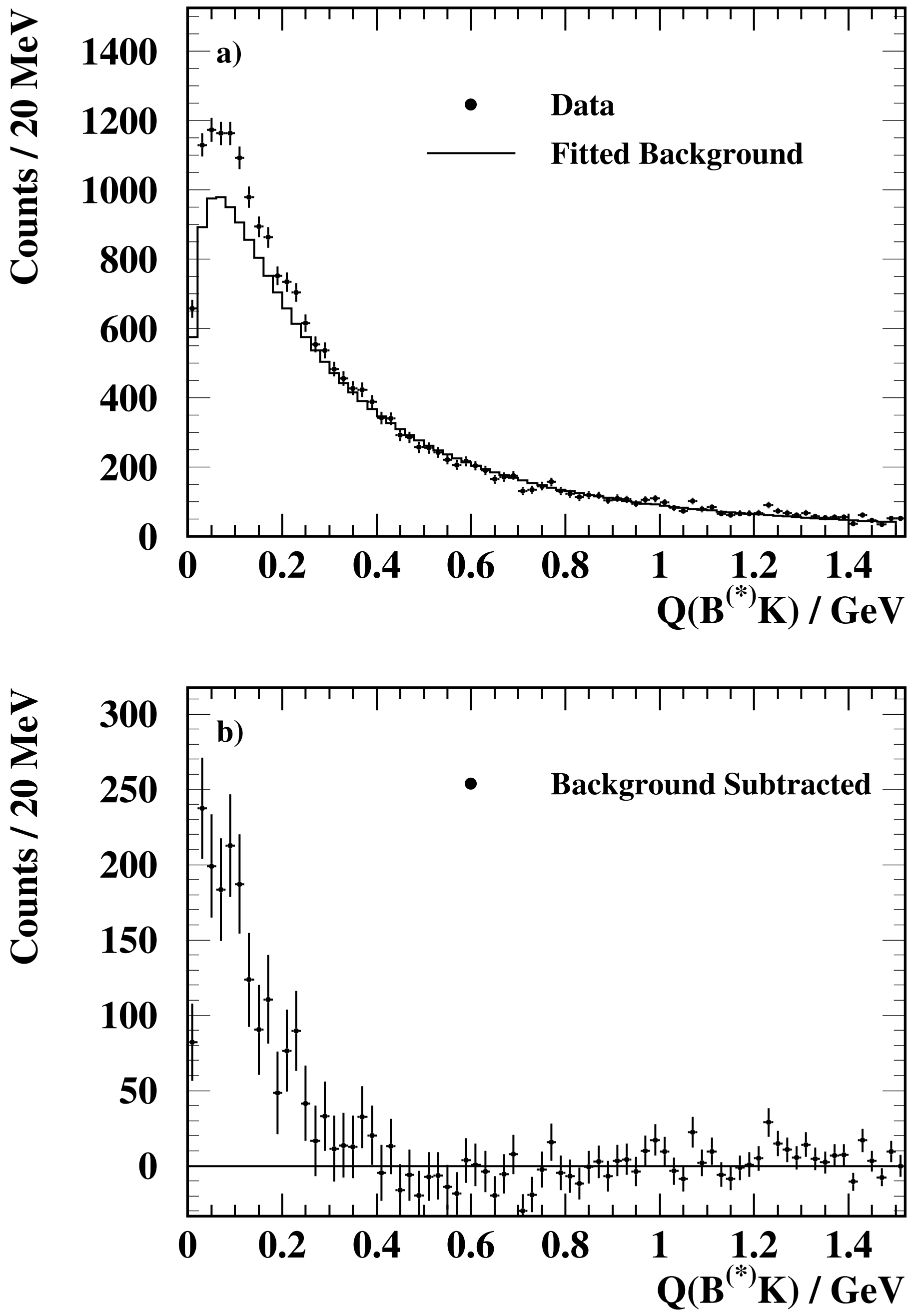

Figure 6.21: The result of using the fitted MC background shape for B_s^{**} a) data and estimated background b) background subtracted data

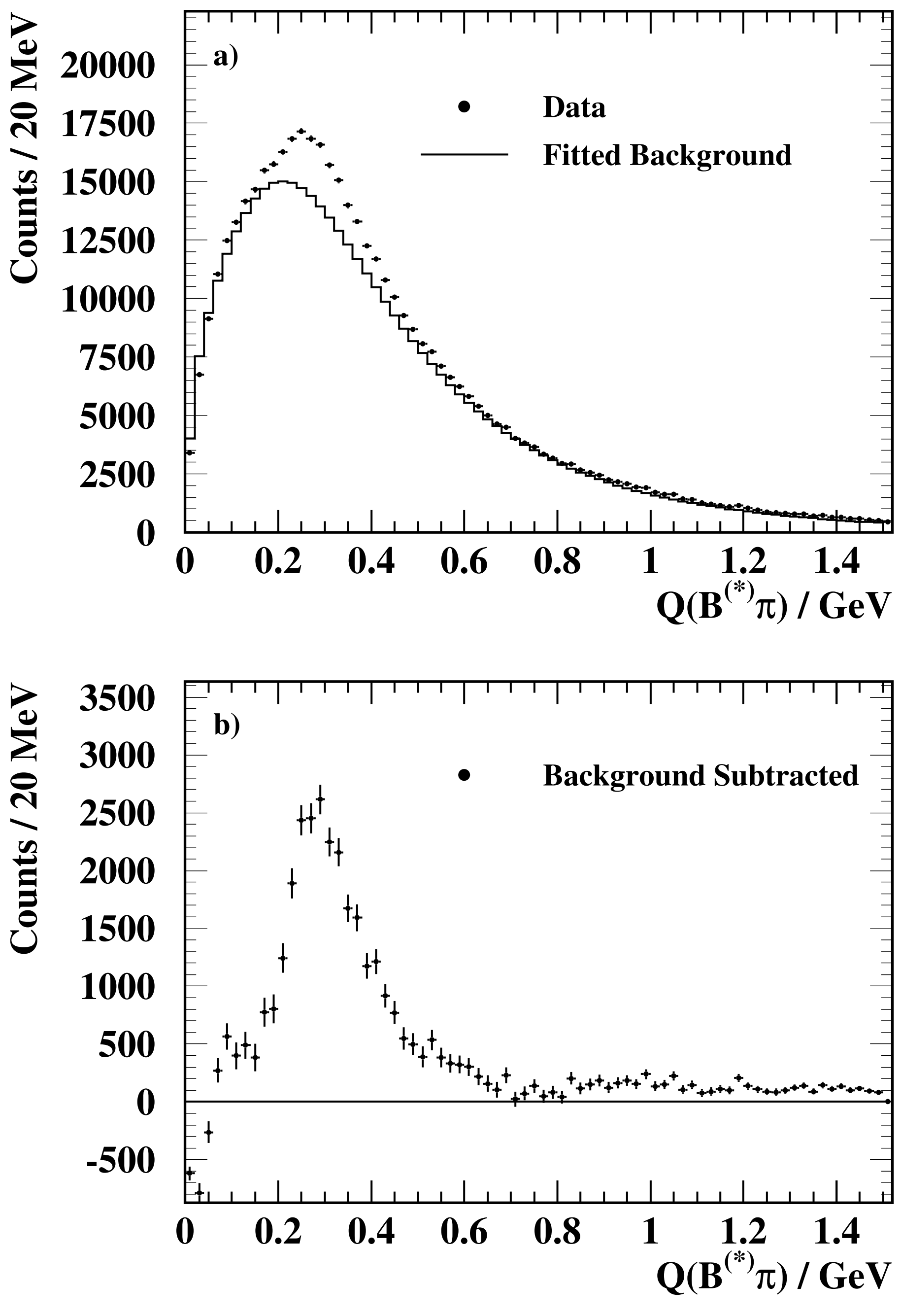

Figure 6.22: The result of using the fitted MC background shape for B^{**} on Data with the normalisation adjusted to give the same peak height as that given when the background derived from data is used a) data and estimated background b) background subtracted data

not fully understood but the step in the angular distribution caused by the cone jet algorithm is responsible for the failure of method 2 when applied to B**. Both methods are essentially derived from data, although they do have a small contribution, in the form of the final correction factors, from Monte Carlo.

6.3 Fitting the Signal

6.3.1 Monte Carlo

In order to fit the signal shapes found in the data it is necessary to have a description of the Q resolution as a function of the real Q value. This was obtained by fitting the difference between the real and reconstructed Q value in Monte Carlo data using an unbinned maximum likelihood method. The best results were obtained by using, for the resolution, a combination of an asymmetric Gaussian[j] and a symmetric Gaussian with their parameters having a linear dependence on the real Q. The resolution measured in the Monte Carlo has been compared to the resolution predicted by the fitted function in three bins of real Q where the bins were chosen to give approximately equal numbers in each. The results are shown in figure 6.23 for B^{**} and figure 6.24 for the B_s^{**}. The fitted function models the resolution quite well particularly for the higher statistics B^{**} sample. As a further check the distribution of real Q was convoluted with the resolution function and compared to the reconstructed Q distribution for B^{**} and B_s^{**}(Figure 6.25). In both cases the reconstructed Q distribution is reasonably well reproduced by this convolution.

In order to test the fitting procedure to be used on the data to extract the real Q distribution from the reconstructed Q distribution, the method is first applied to the Monte Carlo signal. The B^{**} and B_s^{**} signal in the Monte Carlo consists of a combination of narrow and wide Breit Wigners. If a resonance decays via B^* as well

[j] The asymmetric Gaussian is a Gaussian bifurcated at the peak position. It thus has the form

$$f(x) = \frac{2}{(\sigma_1 + \sigma_2)\sqrt{2\pi}} \begin{cases} e^{-(x-x_0)^2/2{\sigma_1}^2} & \text{for } x < x_0, \\ e^{-(x-x_0)^2/2{\sigma_2}^2} & \text{for } x \geq x_0 \end{cases}$$

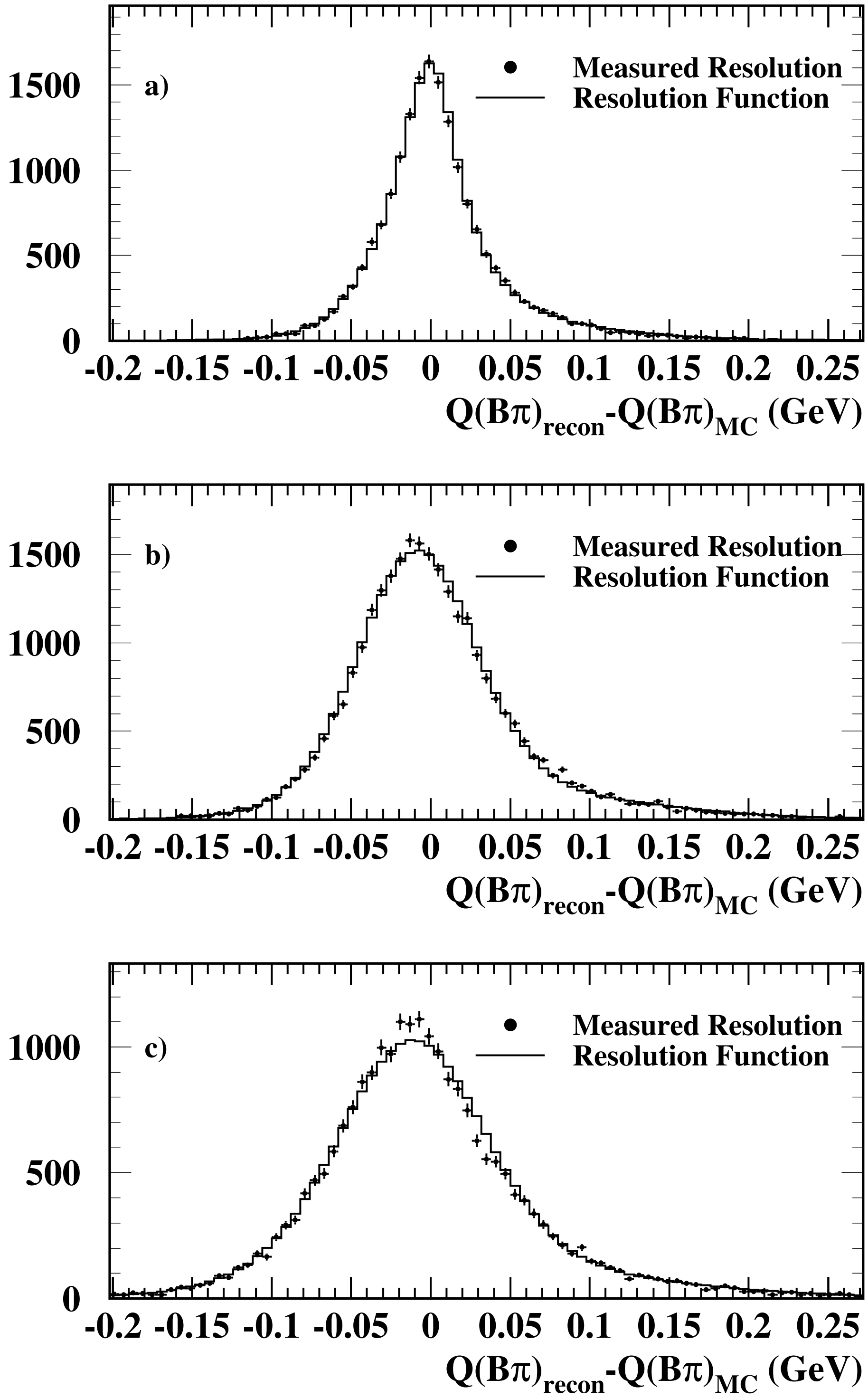

Figure 6.23: Comparing the B^{**} mass resolution measured in the Monte Carlo with that predicted by the fitted resolution function in bins of real Q a) $Q < 0.25$ b) $0.25 < Q < 0.3$ and c) $Q > 0.3$.

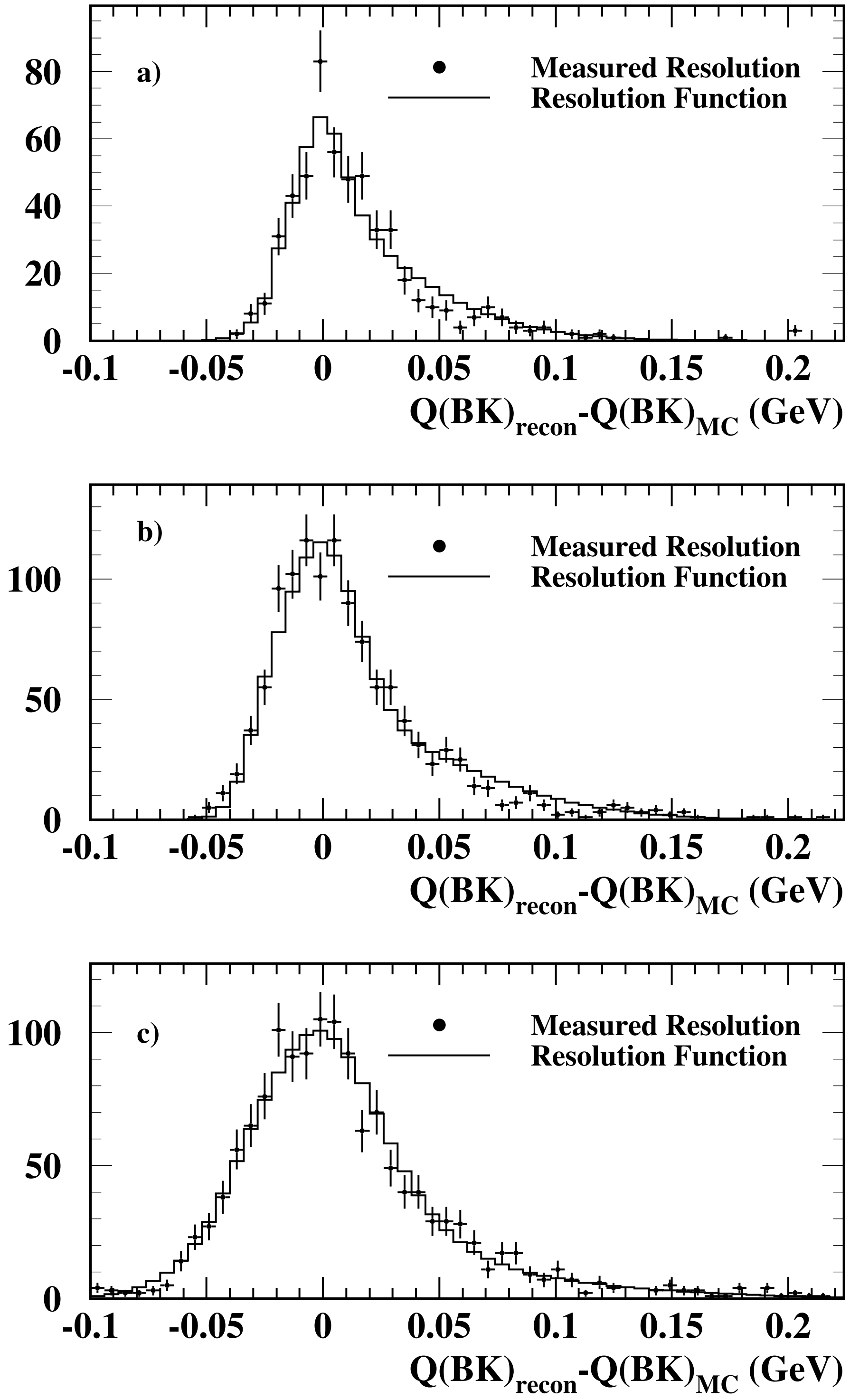

Figure 6.24: Comparing the B_s^{**} mass resolution measured in the Monte Carlo with that predicted by the fitted resolution function in bins of real Q a) $Q < 0.05$ b) $0.05 < Q < 0.06$ and c) $Q > 0.06$.

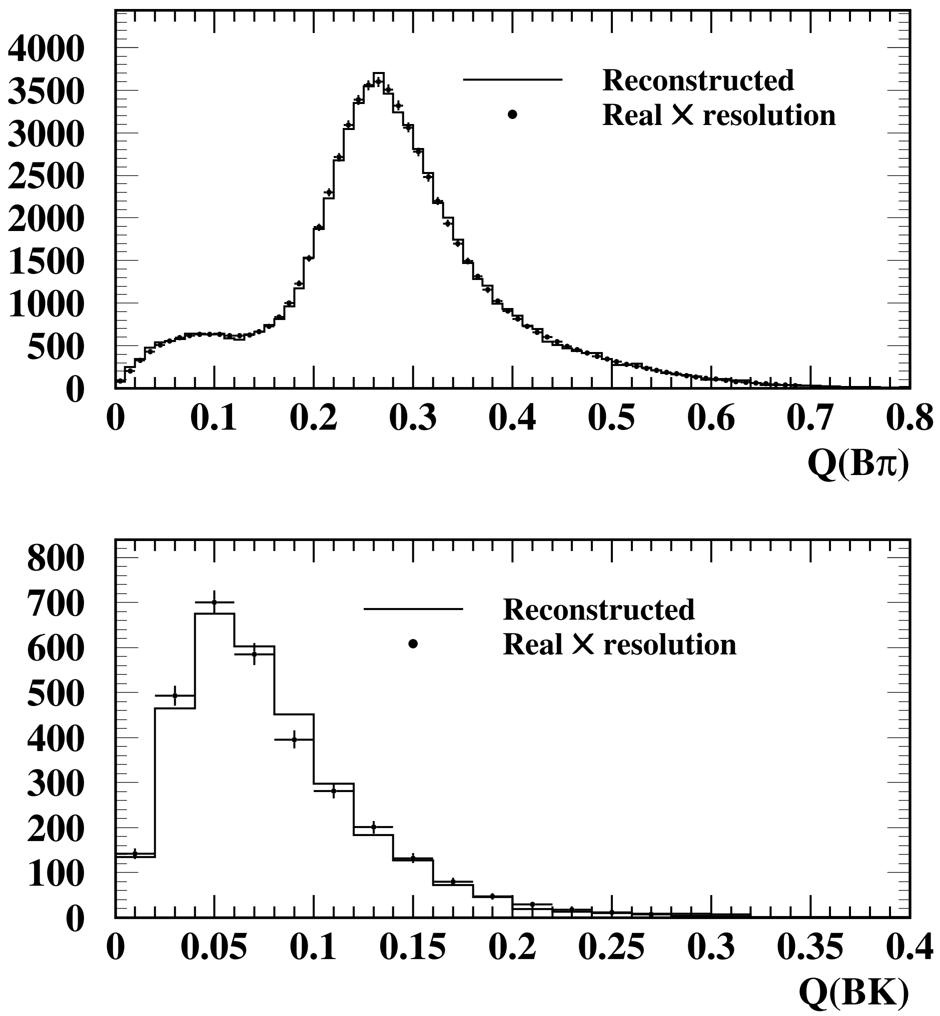

Figure 6.25: Comparing the real Q distribution convoluted with the resolution function with the reconstructed Q distribution a) for $B^{**}$and b) for B_s^{**}.

as directly to B then two peaks will appear in the Q distribution separated by the B* – B mass difference ($\sim$ 46MeV). The B** signal in the Monte Carlo (see figure 6.26(b)) consists of two narrow and two wide resonances. The two narrow resonances are nearly degenerate and only give rise to two peaks in the Q distribution separated by the B* – B mass difference for the reasons discussed above. The two narrow peaks are represented in the fit by two narrow Breit Wigners with widths of 0.02 GeV, which is consistent with theoretical expectations and well below the experimental resolution. Since the two wide Breit Wigners are not significantly separated they are represented in the fit by a single wide Breit Wigner with the width constrained to be more than 0.25 GeV. The presence of events at very low Q values due to the decay B$^{**} \rightarrow$ B$\pi\pi$ is accounted for by fitting their real Q distribution to a Gaussian and then including this in the fit with only its normalisation allowed to vary. In order to reduce the sensitivity to this contribution the fit is made to the region above $Q = 0.1$. The B$^*\pi$ reconstructed Q distribution for Monte Carlo data is shown in figure 6.26(a) and the corresponding true Q distribution is shown in figure 6.26(b). The results of a χ^2 fit to the reconstructed distribution using the resolution function discussed earlier is shown as a solid line on figure 6.26(a). This reproduces the distribution well and the corresponding extracted true Q distribution is shown as a solid line on figure 6.26(b). The χ^2/ndf of the fit is 1.16 and the agreement between the fitted function and the real signal shape is reasonable with the narrow peaks having approximately the correct masses and separations. The values of the fitted fit parameters are shown in table 6.2.

The B$_s^{**}$ signal in the Monte Carlo also consists of two narrow and two wide resonances. Unlike the B** case the two narrow resonances are not degenerate leading to potentially four peaks in the Q distribution (due to possible decay via B*). However the narrow resonance at lower Q has a branching ratio for B* decay of 100% so the signal shown in figure 6.27(b)) shows only three peaks. The wide resonances supply a small contribution predominantly at low Q. Due to the finite resolution and the lower statistics in this channel, the two lower peaks due to the decay via B* are represented in the fit by just a single narrow Breit Wigner. The fit includes one other narrow Breit Wigner and also a wide Breit Wigner. The widths of the narrow Breit Wigners are

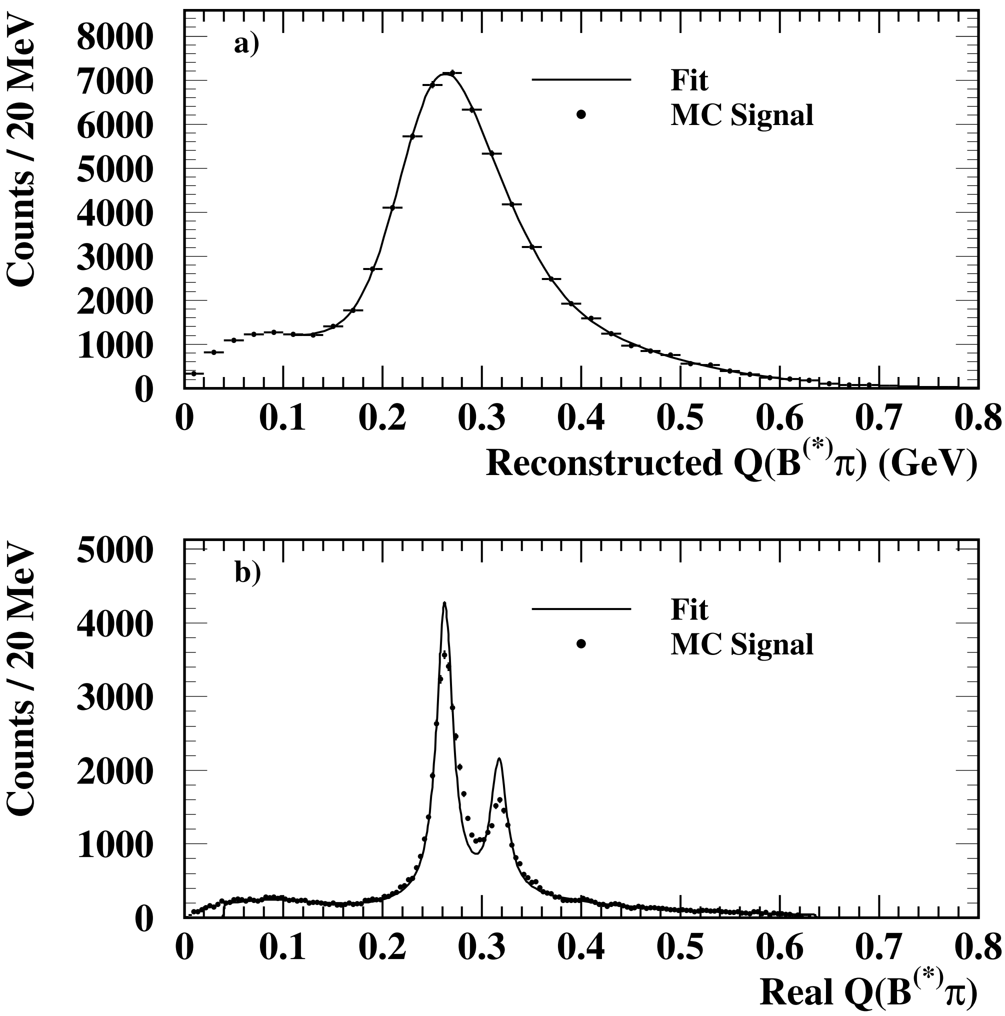

Figure 6.26: Comparing the fitted and true B^{**} signal in the Monte Carlo. a) The reconstructed Q distributions. b) The real Q distribution.

Parameter	Value
$B\pi\pi$ Normalisation	5950 ± 770
$B\pi$ Normalisation	70100 ± 1200
Fraction (1)	0.344 ± 0.033
Central value (1)	0.331 ± 0.016 GeV
Width (1)	0.270 ± 0.025 GeV
Fraction (2)	0.691 ± 0.048
Central Value (2)	0.2625 ± 0.0026 GeV
Separation (2 – 3)	0.0547 ± 0.0035 GeV
χ^2/ndf	1.16

Table 6.2: The results of fitting the B^{**} signal in the Monte Carlo. (1) refers to the wide Breit Wigner which contains fraction(1) of the total normalisation. Fraction (2) is the fraction of the normalisation remaining after the wide Breit Wigner has been subtracted that is in the narrow Breit Wigner at the lowest Q value.

fixed at 0.002 GeV, which is consistent with theoretical expectations and well below the experimental resolution. The wide Breit Wigner is constrained such that its width is greater than 0.03 GeV. The $B^{(*)}K$ reconstructed Q distribution for Monte Carlo data is shown in figure 6.27(a) and the corresponding true Q in figure 6.27(b). The results of a χ^2 fit to the reconstructed distribution using the resolution function discussed earlier is also shown as a solid line on figure 6.27(a). This reproduces the distribution well and the extracted true Q distribution is shown in figure 6.27(c). The lower fitted peak is close to the two real lower peaks while the upper peak is fitted at a somewhat smaller Q value than the true peak position. With the limited statistics of this channel more complex fits, e.g. with three narrow Breit Wigners, did not produce stable solutions. The poor reconstruction of the upper peak results from these simplifying assumptions. The values of the fitted parameters are shown in table 6.3.

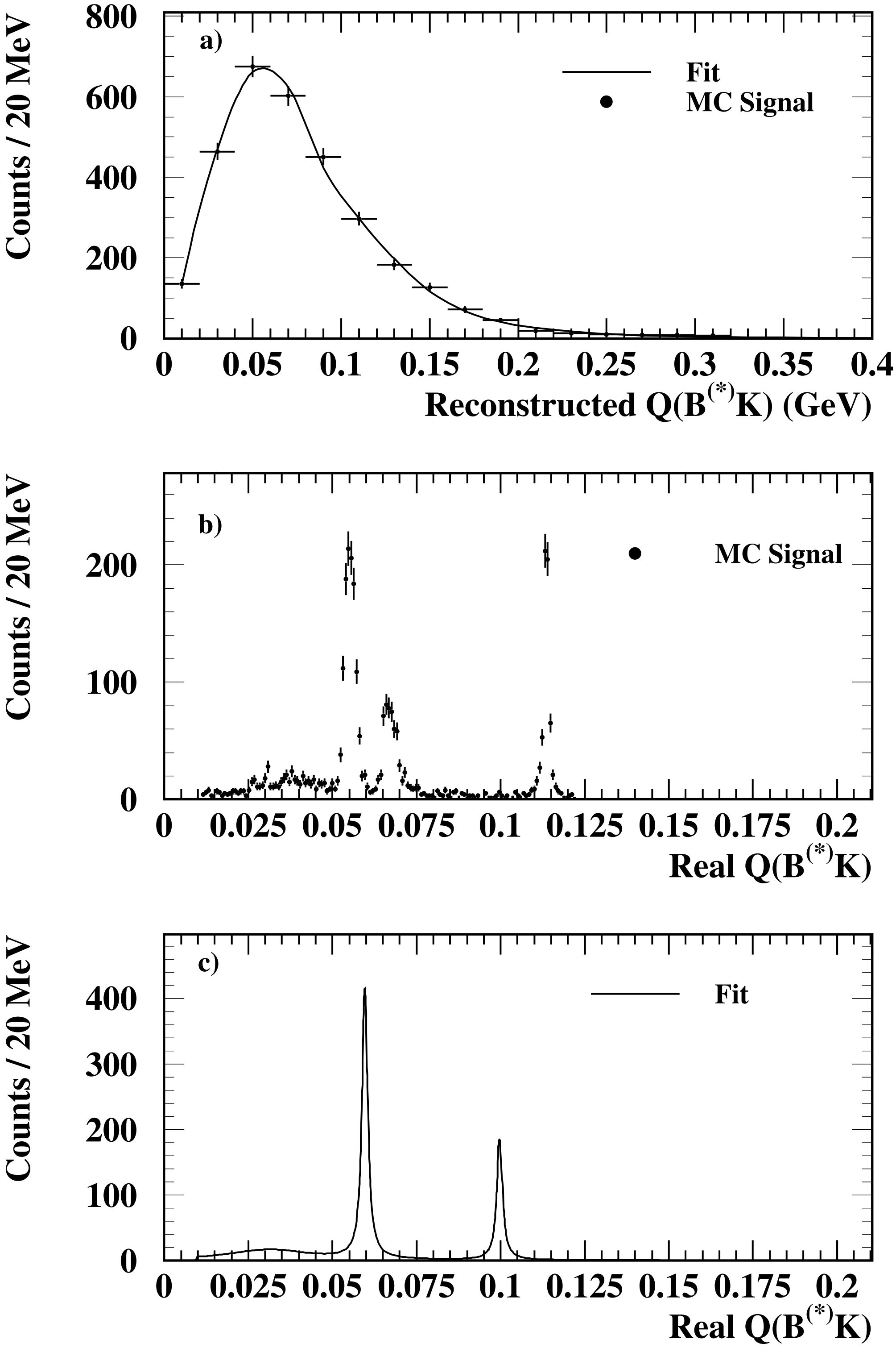

Figure 6.27: Comparing the fitted and true B_s^{**} signal in the Monte Carlo. a) The reconstructed Q distributions. b) The real Q distribution of the Monte Carlo Signal. c) The real Q distribution of the fitted signal.

Parameter	Value
Normalisation	3318 ± 62
Fraction (1)	0.291 ± 0.043
Central value (1)	0.0310 ± 0.0047 GeV
Width (1)	0.030 ± 0.0041 GeV (at limit)
Fraction (2)	0.689 ± 0.043
Central Value (2)	0.05959 ± 0.00069 GeV
Separation (2 – 3)	0.0401 ± 0.0039 GeV
χ^2/ndf	1.08

Table 6.3: The results of fitting the B_s^{**} signal in the Monte Carlo. (1) refers to the wide Breit Wigner which contains fraction(1) of the total normalisation. Fraction (2) is the fraction of the normalisation remaining after the wide Breit Wigner has been subtracted that is in the narrow Breit Wigner at the lowest Q value.

6.3.2 Extracting the B^{**} Signal from the data

The predictions from HQET for the B^{**} structure (see section 1.2.3) predict the same sort of resonance structure as that used in the existing Monte Carlo and hence the data has been fitted initially using the same functional form as in the Monte Carlo convoluted with the expected resolution. When looking at the background subtracted signal for B^{**} found in the data (figure 6.18), it can be seen that a number of bins in the range $0.6 < Q < 0.8$ have small negative values, which are unphysical, indicating problems with the background subtraction in this region. Also as for the Monte Carlo, there is a small peak at very low Q from $B\pi\pi$ decay. This shape is taken from Monte Carlo but the normalisation is allowed to vary. To reduce the sensitivity of the fit to these effects the B^{**} signal in the data has been fitted in the range $0.1 < Q < 0.6$. The fit to the reconstructed $Q(B^{(*)}\pi)$ distribution for the data, which is shown in figure 6.28(a), reproduces the experimental data quite well. The fitted result for the real Q distribution is shown in figure 6.28(b) and the fitted parameters are shown in table 6.4. The separation between the two extracted peaks is significantly larger than that seen in the Monte Carlo (due to the B^*–B mass difference) and that predicted by

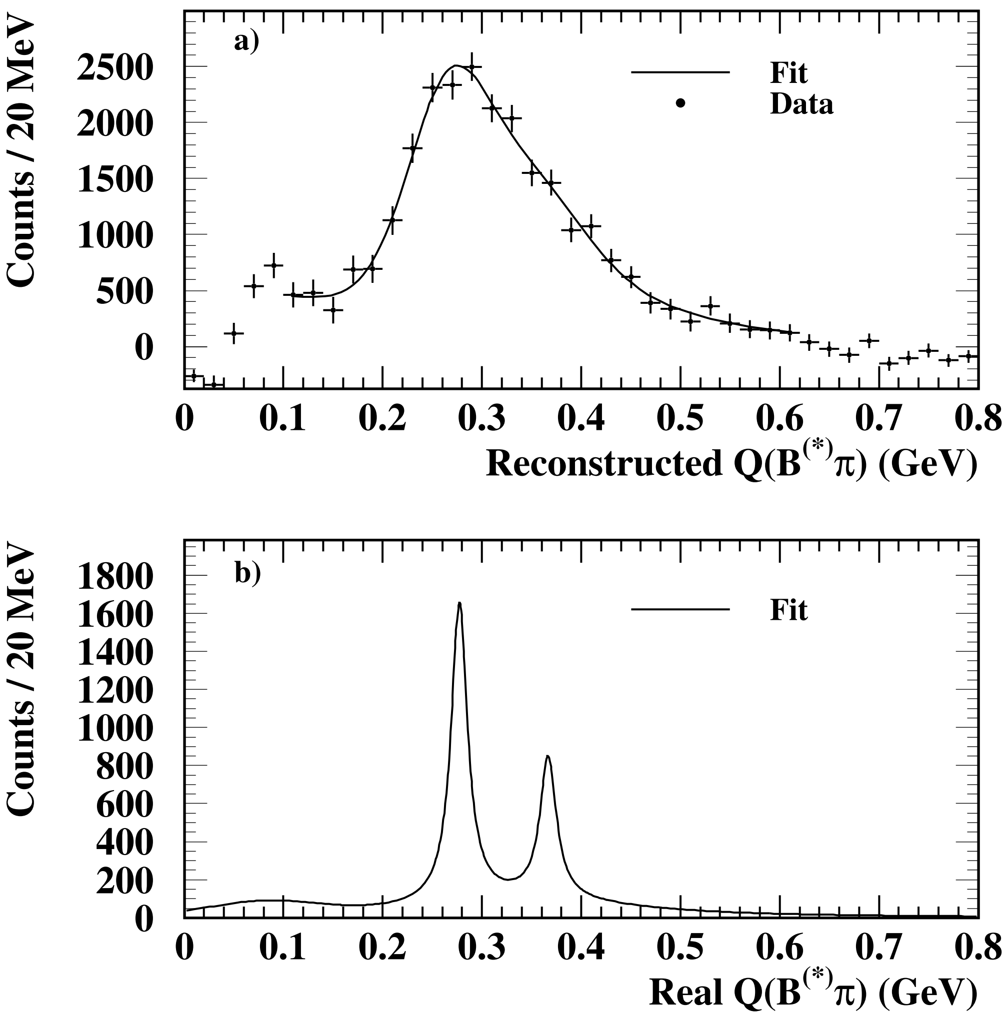

Figure 6.28: The fitted B^{**} signal in the Data. a) The reconstructed Q distributions. b) The extracted Q distribution.

Parameter	Value
B$\pi\pi$ Normalisation	2300 ± 1200
Bπ Normalisation	27700 ± 1700
Fraction (1)	0.34 ± 0.12
Central value (1)	0.343 ± 0.061 GeV
Width (1)	0.25 ± 0.48 GeV
Fraction (2)	0.681 ± 0.060
Central Value (2)	0.2772 ± 0.0066 GeV
Separation (2 – 3)	0.090 ± 0.012 GeV
χ^2/ndf	0.79

Table 6.4: The results of fitting the B** signal in the Data (1) refers to the wide Breit Wigner which contains fraction(1) of the total normalisation. The Normalisation of the wide Breit Wigner is subtracted from the total and Fraction (2) of the result is the normalisation of the narrow Breit Wigner at the lowest Q value. Central Value refers to the central value of the Breit Wigner while separation(2–3) refers to the separation between the central values of the two narrow Breit Wigners.

HQET when only statistical errors are considered. However the relative amounts of the two peaks are similar to that seen in the Monte Carlo. The size of the systematic errors will be discussed in section 6.4. The relative production ratio of B** per b-jet can be calculated from the expression

$$\frac{\sigma_{\mathrm{B}^{**}}}{\sigma_{b-jet}} = \frac{N_{\mathrm{B}^{**}}\epsilon_{\mathrm{B}}}{(N_{jets}\eta_{\mathrm{B}}\epsilon_{\mathrm{B}^{**}})} \tag{6.3}$$

where ϵ_{B} is the efficiency for tagging b-jets, N_{jets} is the number of jets selected by the jet and vertex cuts, η_{B} is the purity of the b-jet sample and $\epsilon_{\mathrm{B}^{**}}$ is the total efficiency for finding B**. In the data sample 409750 jets are selected. The purity and efficiency of the b-tagging are measured in the Monte Carlo to be $92.49 \pm 0.19\%$ and $25.381 \pm 0.040\%$ respectively. The B** efficiency (see table 5.2) is measured in the Monte Carlo to be $5.813 \pm 0.025\%$. The fitted reconstructed Q distribution when summed gives

$$N_{\mathrm{B}^{**}} = 25500 \pm 1600(\mathrm{stat})$$

events and hence the production ratio is calculated to be

$$\frac{\sigma_{\mathrm{B}^{**}}}{\sigma_{b-jet}} = 0.294 \pm 0.018(\mathrm{data\ stat}) \pm 0.0015(\mathrm{mc\ stat})$$

where the mc statistical error comes from the statistical errors on the b purity and efficiency, and also the statistical errors on the B** efficiency which are all measured using Monte Carlo data.

6.3.3 Extracting the $\mathrm{B_s^{**}}$ Signal

As in the B** case HQET predicts a similar resonant structure as that used to generate the Monte Carlo. Hence the reconstructed $\mathrm{B_s^{**}}$ signal in the data was also fitted by convoluting a combination of two narrow and one wide Breit Wigner with the expected resolution. However the normalisation of the wide Breit Wigner became extremely small so it was removed from the final fit. The fit to the reconstructed Q(BK) distribution for the data performed for $Q < 0.4$, which is shown in figure 6.29(a), reproduces the experimental data quite well at low Q values although there is some disagreement in the region $Q > 0.2$. The fitted result for the real $Q(\mathrm{B}^{(*)}\mathrm{K})$ distribution is shown in figure 6.29(b) and the fitted parameters are listed in table 6.5. The fit has a fairly large χ^2/ndf of 1.7 which is mainly due to the bins in the region $Q > 0.2$. The separation between the two peaks is significantly larger than both that extracted from the Monte Carlo and that predicted from HQET when only statistical errors are considered. The relative amounts of the two peaks is also significantly different than that extracted from the Monte Carlo with roughly equal amounts being fitted in each peak whereas the Monte Carlo fit places the ratio at 0.7:0.3 (lower peak:higher peak). The size of the systematic errors will be discussed in section 6.4.

The number of B_s^{**} is obtained by summing the function fitted to the reconstructed Q distribution.

$$N_{\mathrm{B}_s^{**}} = 1590 \pm 100(\mathrm{stat})$$

The total efficiency for finding B_s^{**} was measured to be $1.845 \pm 0.035\%$ by taking the number of reconstructed B_s^{**} and dividing by the total number of B_s^{**} present in the Monte Carlo. Hence equation 6.3 can be used to calculate

$$\sigma_{\mathrm{B}_s^{**}}/\sigma_{b-jet} = 0.0576 \pm 0.0036(\mathrm{data\ stat}) \pm 0.0011(\mathrm{mc\ stat})$$

Parameter	Value
Normalisation	1600 ± 100
Fraction (in 1)	0.493 ± 0.061
Central Value (1)	0.0363 ± 0.0028 GeV
Separation (1 − 2)	0.0803 ± 0.012 GeV
χ^2/ndf	1.7

Table 6.5: The results of fitting the B_s^{**} signal in the data (1) and (2) refer to the two narrow Breit Wigners.

6.4 Systematic Studies

Several sources of systematic errors have been considered, the size of the normalisation of the background to the data has been varied by it's error both up and down. The

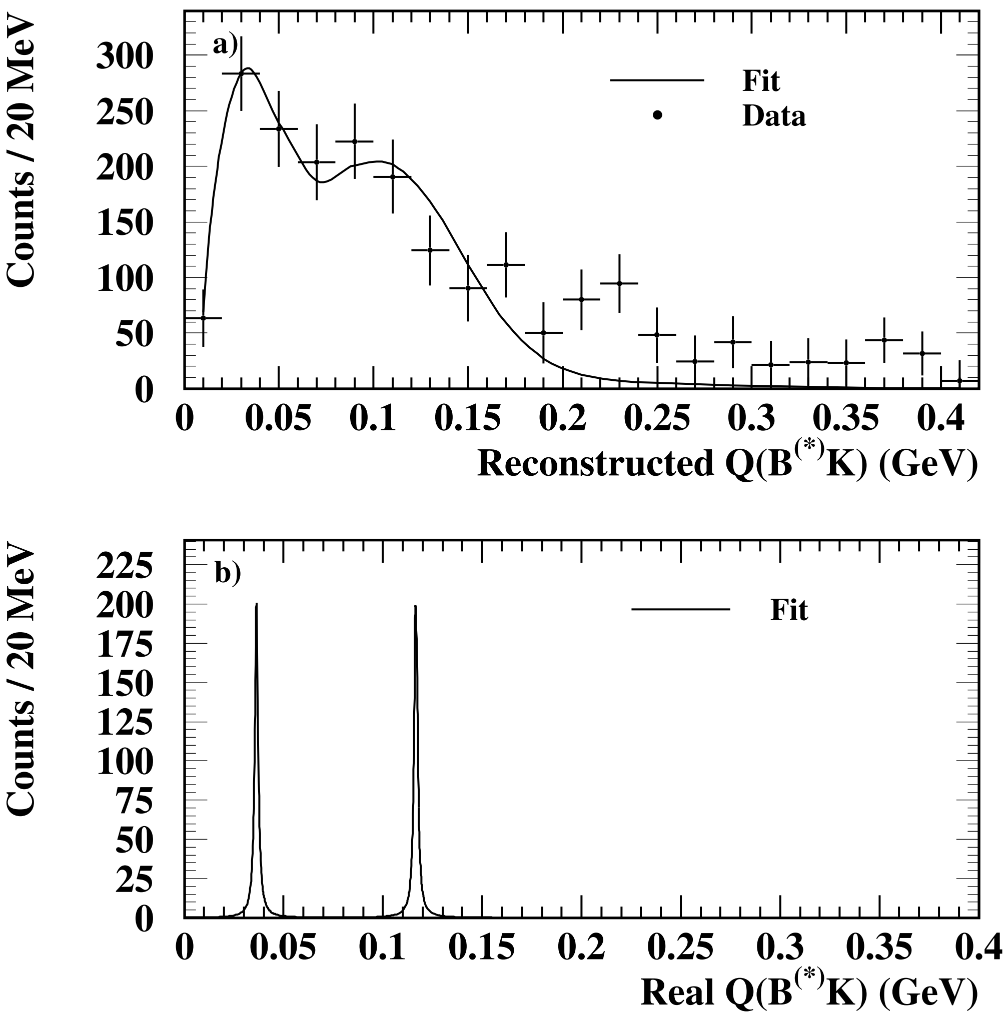

Figure 6.29: The fitted B_s^{**} signal in the Data. a) The reconstructed Q distributions. b) The extracted Q distribution.

Parameter	Standard	Norm +	Norm -	No Fit	Resolution
B$\pi\pi$ Normalisation	2300 ± 1200	2000	2600	1400	1700
Bπ Normalisation	27700 ± 1700	25000	30300	29300	28000
Fraction (1)	0.34 ± 0.12	0.24	0.43	0.51	0.40
Central value (1) /GeV	0.344 ± 0.061	0.351	0.340	0.345	0.307
Width (1) /GeV	0.25 ± 0.48	0.25	0.25	0.25	0.25
Fraction (2)	0.681 ± 0.060	0.672	0.690	0.308	0.727
Central Value (2) /GeV	0.2772 ± 0.0066	0.2778	0.2766	0.2544	0.2848
Separation (2 – 3) /GeV	0.090 ± 0.012	0.091	0.088	0.044	0.097
χ^2/ndf	0.79	0.80	0.79	1.9	0.8

Table 6.6: The sources of Systematic errors and their effects on the B** fit parameters

possible distortion of the background shape caused by fitting it to a function has been assessed by using the unfitted background shape. Possible errors caused by the resolution function being incorrect are evaluated by looking at the differences between the reconstructed Q signal distribution for the Monte Carlo and that produced by convoluting the true Q signal distribution of the Monte Carlo with the resolution function. These differences are calculated as the ratio of the two distributions. This bin by bin factor is then applied to the reconstructed Q signal distribution taken from the data and the signal fit repeated.

6.4.1 B**

The values of the fitted parameters obtained for the B** signal when these methods are applied are compared to the standard values in table 6.6. The large effect caused by not fitting the background is due to a change in the shape of the background subtracted signal distribution. This indicates that this analysis has a large dependence on the exact shape of the background prediction as the fit to the background (shown in figure 6.17) shows no obvious problems. The analysis is particularly sensitive to the background shape due to the signal peak being close to the background peak and also the relatively low purity of this analysis means a small percentage change in the background estimate leads to a large percentage change in the signal. Once systematic errors have been included the number of B^{**} within the signal becomes

$$N_{B^{**}} = 25500 \pm 1600(\mathrm{stat})^{+2100}_{-2000}(\mathrm{syst})$$

where due to the non-symmetric nature of the no fit and resolution systematics the positive and negative systematic errors have been summed in quadrature separately. This leads to the result

$$\frac{\sigma_{B^{**}}}{\sigma_{b-jet}} = 0.294 \pm 0.018(\mathrm{data\ stat}) \pm 0.0015(\mathrm{mc\ stat})^{+0.024}_{-0.023}(\mathrm{syst})$$

The separation of the two narrow Breit Wigners is

$$B^{**}\ \mathrm{Peak\ Separation} = 0.090 \pm 0.012(\mathrm{stat})^{+0.007}_{-0.045}(\mathrm{syst})$$

The size of the systematic errors means that this separation no longer excludes the possibility that the separation is due to the B^{*}–B mass difference. The central values of the two narrow Breit Wigners are found to be

$$\begin{aligned} Q(1) &= 0.277 \pm 0.007(\mathrm{stat})^{+0.008}_{-0.023}(\mathrm{syst}) \\ Q(2) &= 0.367 \pm 0.018(\mathrm{stat})^{+0.015}_{-0.068}(\mathrm{syst}) \end{aligned}$$

6.4.2 B_s^{**}

The B^{**} fit has been repeated with the normalisation varied, with the background unfitted and with the effects of a modified resolution function included as described above. The values of the fitted parameters obtained are compared to the standard fit values in table 6.7. The effects of these systematic studies on the fitted parameters are quite large and also in most cases give a much worse χ^2 per degree of freedom. These reflect the problems inherent in fitting a fairly complex function to a limited statistics sample. Also as for the B^{**} case small changes in the background shape can have large effects due to the signal being close to the background peak. Once systematic errors have been included the number of B_s^{**} within the signal becomes

$$N_{B_s^{**}} = 1600 \pm 100(\mathrm{stat})^{+160}_{-170}(\mathrm{syst})$$

Parameter	Standard	Norm +	Norm -	No Fit	Resolution
Normalisation	1600 ± 100	1450	1770	1570	1540
Fraction (in 2)	0.493 ± 0.061	0.496	0.494	0.389	0.423
Central Value (2) /GeV	0.0363 ± 0.0028	0.0361	0.0367	0.0311	0.0348
Separation (2 – 3) /GeV	0.0803 ± 0.012	0.0751	0.0866	0.0731	0.0674
χ^2/ndf	1.08	1.18	2.32	2.77	3.7

Table 6.7: The sources of Systematic errors and their effects on the $\mathrm{B_s^{**}}$ fit parameters

which in turn gives

$$\frac{\sigma_{\mathrm{B_s^{**}}}}{\sigma_{b-jet}} = 0.0576 \pm 0.0036(\text{data stat}) \pm 0.0011(\text{mc stat})^{+0.0059}_{-0.0061}(\text{syst})$$

The separation of the two narrow Breit Wigners is

$$\mathrm{B_s^{**}}\ \text{Peak Separation} = 0.080 \pm 0.012(\text{stat})^{+0.006}_{-0.016}(\text{syst})$$

This separation is 1.75σ larger than the expected value for that due to the B*–B mass difference (46 MeV) suggesting that the underlying structure may be due to more than one resonance. When the reconstructed Q distribution of the signal found in Monte Carlo (figure 6.27) is compared to the background subtracted distribution from the data (figure 6.29) there are obvious differences suggesting that this effect is unlikely to be a fitting effect. The two central values of the narrow Breit Wigners are

$$\begin{aligned} Q(1) &= 0.0363 \pm 0.0028(\text{stat})^{+0.0003}_{-0.0055}(\text{syst}) \\ Q(2) &= 0.117 \pm 0.012(\text{stat})^{+0.007}_{-0.020}(\text{syst}) \end{aligned}$$

however these should be regarded with caution given the problems found in trying to fit the Monte Carlo signal.

6.5 Comparison with Other Measurements

6.5.1 B^{**}

ALEPH have measured the production ratio [77]

$$\frac{BR(Z^0 \to b \to B^{**})}{BR(Z^0 \to b \to B_{u,d})} = 0.279 \pm 0.016(stat) \pm 0.059(syst)^{+0.039}_{-0.056}(model)$$

where they have used the fact that the fraction of $B_{u.d}$ mesons produced in $Z^0 \to b\overline{b}$ decays is $76.8 \pm 5.2\%$. Hence the following production ratio can be calculated

$$\frac{\sigma_{B^{**}}}{\sigma_{b-jet}} = 0.363 \pm 0.021(stat) \pm 0.077(syst)^{+0.051}_{-0.073}(model)$$

DELPHI have measured [78]

$$\frac{\sigma_{B^{**}}}{\sigma_{b-jet}} = 0.26 \pm 0.015(stat) \pm 0.05(syst)$$

both of which are compatible with the measurement from this analysis of

$$\frac{\sigma_{B^{**}}}{\sigma_{b-jet}} = 0.294 \pm 0.018(\mathrm{data\ stat}) \pm 0.0015(\mathrm{mc\ stat})^{+0.024}_{-0.023}(\mathrm{syst})$$

Although this analysis has a much larger background subtracted signal to fit than either of these measurements the lower purity coupled with the effects of fitting a more complex signal shape, including the $B\pi\pi$contributions, gives this analysis a similar size of statistical error to those of ALEPH and DELPHI. The systematic errors of this measurements are smaller than those obtained by ALEPH and DELPHI.

Both ALEPH and DELPHI have fitted the B^{**} signal to a single Gaussian so for comparison the signal from this measurement has also been fitted to a Gaussian (plus the $B\pi\pi$ contribution) convoluted with the experimental resolution. The fitted function can be seen in figure 6.30 and the values of the fitted parameters in table 6.8. This fit gives a χ^2 per degree of freedom of 1.9 which is as expected much larger than the value of 0.79 found when the standard fit is used. The previously mentioned systematic studies have been repeated and the results are shown in table 6.8. The resulting value for the central position of the Gaussian is $0.3099 \pm 0.0024(\mathrm{stat})^{+0.0007}_{-0.0090}(\mathrm{syst})$ GeV. ALEPH found a central value of $0.284 \pm 0.004(\mathrm{stat}) \pm 0.010(\mathrm{syst})$ GeV while DELPHI a value of $0.285 \pm 0.005(\mathrm{stat}) \pm 0.012(\mathrm{syst})$ GeV which are both approximately 2σ from the value measured here.

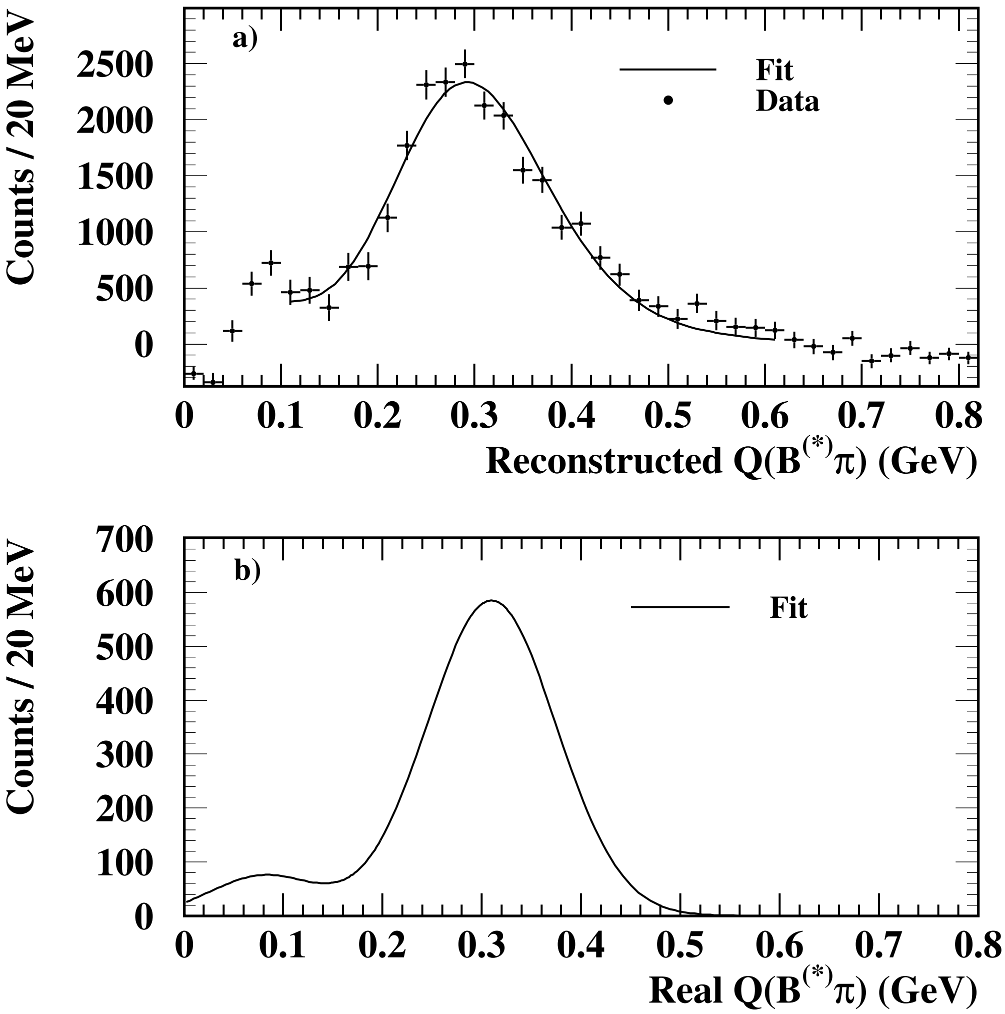

Figure 6.30: Fitting the B^{**} signal to a single Gaussian. a) The reconstructed Q distributions. b) The real Q distribution.

Parameter	Standard	Norm +	Norm -	No Fit	Resolution
$B\pi\pi$ Normalisation	2540 ± 810	2070	2930	2150	2510
$B\pi$ Normalisation	23800 ± 610	22320	25410	23250	23710
Central Value (GeV)	0.3099 ± 0.0024	0.3091	0.3105	0.3009	0.3100
σ (GeV)	0.0650 ± 0.0034	0.0611	0.0690	0.0629	0.0652
χ^2/ndf	1.9	1.7	2.3	3.9	2.0

Table 6.8: The results of fitting the B^{**} signal with a single Gaussian.

6.5.2 B_s^{**}

The only other measurement of the B_s^{**} mass peaks has been performed by DELPHI [78], where they report finding two separated peaks. This analysis has not found a similar structure in the reconstructed Q distribution (figure 6.29(a)). However to allow a comparison the reconstructed Q distribution has been refitted by adding an extra narrow Breit Wigner at $Q = 0.142$ GeV, the value reported by DELPHI. The normalisation of this peak has been varied and the effect on the χ^2 of the fit is shown in figure 6.31. The results show that if this extra peak is included the fit prefers a non-

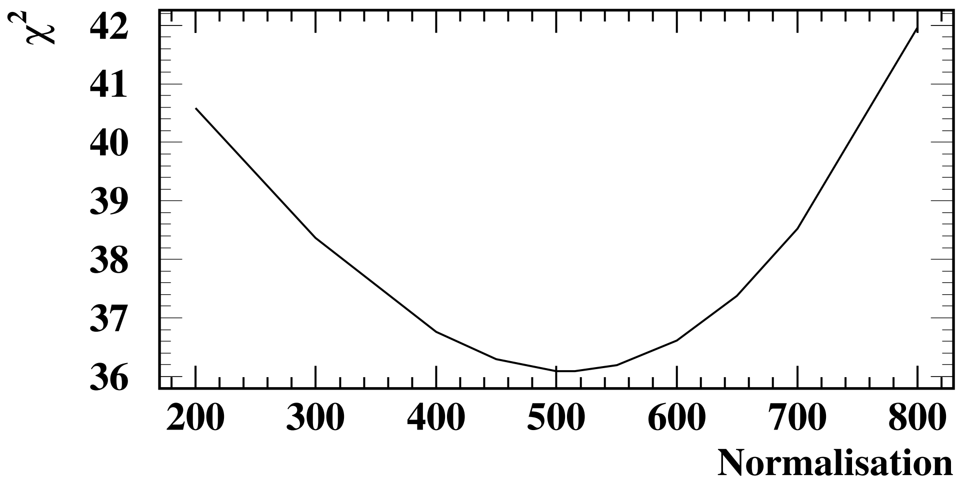

Figure 6.31: The effects on the χ^2 for the fit of including a narrow Breit Wigner at the upper position found by DELPHI.

zero contribution from it. The fit was repeated with the normalisation of the DELPHI peak allowed to vary, the fitted Q distributions are shown in figure 6.32 and the fit parameters in table 6.9. Delphi reported a production rate of

$$\frac{\sigma_{B^*_{s2}} \cdot Br(B^*_{s2} \to BK)}{\sigma_{b-jet}} = 0.016 \pm 0.005(\text{stat}) \pm 0.007(\text{syst})$$

This measurement gives a value of 0.0185±0.0047 which is compatible with the DELPHI result.

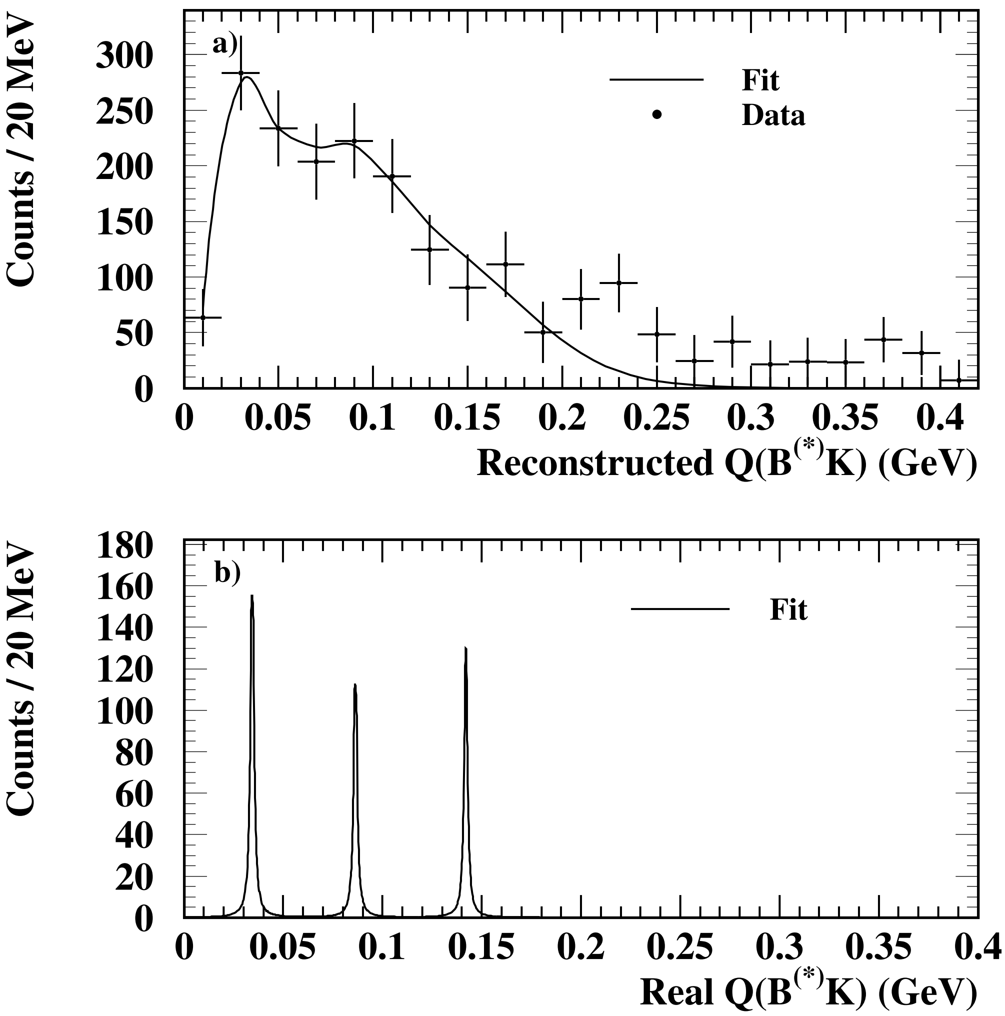

Figure 6.32: The fitted B_s^{**} signal in the Data when an extra peak at the Q value measured by DELPHI is included in the fit. a) The reconstructed Q distributions. b) The extracted Q distribution.

Parameter	Value
Normalisation of DELPHI peak	510 ± 130
Normalisation of other peaks	1170 ± 130
Fraction (1)	0.58 ± 0.11
Central value (1)	0.0344 ± 0.0034 GeV
Separation (1 – 2)	0.0520 ± 0.0089 GeV
χ^2/ndf	1.4

Table 6.9: The results of fitting the B_s^{**} signal including a narrow Breit Wigner at the Q value reported by DELPHI. Of the two other narrow Breit Wigners fraction(1) of the normalisation is contained within the lower peak which is centred at central value (1). Separation(1–2) refers to the separation between the two non DELPHI narrow Breit Wigners. Errors are statistical only.

6.6 Conclusions

This analysis has performed the reconstruction of B^{**} and B_s^{**} using an inclusive B reconstruction technique. The backgrounds to the signals have been determined using the data sample. The signals have then been fitted using signal functions convoluted with the experimental resolution. The B^{**} fit gives the following central values for the two narrow Breit Wigners in the fit.

$$\begin{aligned} Q(1) &= 0.277 \pm 0.007(\text{stat})^{+0.008}_{-0.023}(\text{syst}) \\ Q(2) &= 0.367 \pm 0.018(\text{stat})^{+0.015}_{-0.068}(\text{syst}) \end{aligned}$$

The separation between the two peaks is compatible with that which is expected due to the B^*–B mass difference. The number of B^{**} found has been used to calculate the production ratio

$$\frac{\sigma_{B^{**}}}{\sigma_{b-jet}} = 0.294 \pm 0.018(\text{data stat}) \pm 0.0015(\text{mc stat})^{+0.024}_{-0.023}(\text{syst})$$

Similar quantities have been extracted from the B_s^{**} fit:

$$\begin{aligned} Q(1) &= 0.0363 \pm 0.0028(\text{stat})^{+0.0003}_{-0.0055}(\text{syst}) \\ Q(2) &= 0.117 \pm 0.012(\text{stat})^{+0.007}_{-0.020}(\text{syst}) \\ \frac{\sigma_{B_s^{**}}}{\sigma_{b-jet}} &= 0.0576 \pm 0.0036(\text{data stat}) \pm 0.0011(\text{mc stat})^{+0.0059}_{-0.0061}(\text{syst}) \end{aligned}$$

The separation between the two peaks is 1.75σ larger than that expected due to the B^*–B mass difference suggesting that the underlying structure may be due to more than one resonance.

The effects of including a third peak in the B_s^{**} fit at the Q value reported by DELPHI have been investigated and yield a production ratio which is compatible with that reported by DELPHI.

Appendix A

Relating $\langle Q_j Q_l \rangle$ to χ

The probability of the case where no mixing occurs and the lepton tags the $\overline{\mathrm{b}}$, is $(1-\chi)/2$ the 1/2 is present because χ is the probability for mixing to occur in the event and we are only sensitive to one side of the event having mixed. The value of Q_l will be +1 and the value of Q_j will be $\langle Q_- \rangle$ (Q_- denotes the jet charge in a hemisphere containing a negatively charged primary quark), giving a value for $\langle Q_j Q_l \rangle$ of $\langle Q_- \rangle$. Table A.1 shows the four types of events that can occur with their probabilities and values of $\langle Q_j Q_l \rangle$.

Jet Charge	Lepton tags	Probability	$\langle Q_j Q_l \rangle$
b	$\overline{\mathrm{b}}$	$\frac{1}{2}(1-\chi)$	$\langle Q_- \rangle$
$\overline{\mathrm{b}}$	b	$\frac{1}{2}(1-\chi)$	$-\langle Q_+ \rangle$
b	$\overline{\mathrm{b}}\rightarrow\mathrm{b}$	$\frac{1}{2}\chi$	$-\langle Q_- \rangle$
$\overline{\mathrm{b}}$	$\mathrm{b}\rightarrow\overline{\mathrm{b}}$	$\frac{1}{2}\chi$	$\langle Q_+ \rangle$

Table A.1: Event probabilities

Hence the overall $\langle Q_j Q_l \rangle$ is given by the weighted sum of the four possibilities:

$$\langle Q_j Q_l \rangle = \frac{1}{2}(1-2\chi)(\langle Q_- \rangle - \langle Q_+ \rangle) \tag{A.1}$$

which is the same as

$$\langle Q_j Q_l \rangle = \frac{1}{2}(1-2\chi)\delta \tag{A.2}$$

Appendix B

Relating $\langle Q_F Q_B \rangle$ to δ

If we define Q_F and Q_B as the jet charges measured in the forward and backward hemispheres then we can measure the quantities $\langle Q_F - Q_B \rangle$ and $\langle Q_F \cdot Q_B \rangle$. We can also measure the mean, $\mu(Q)$, and width, $\sigma(Q)$, of the distribution of jet charge for all forward and backward hemispheres. In the Monte Carlo it is possible to measure Q_- and Q_+, the jet charge of the negatively charged and positively charged quarks respectively. Starting from the definition of the covariance of Q_- and Q_+,

$$\begin{aligned} \mathrm{cov}[Q_-, Q_+] &= \langle Q_- Q_+ \rangle - \langle Q_- \rangle \langle Q_+ \rangle \\ &= \langle Q_- Q_+ \rangle + \frac{1}{4}(\delta^2 - \epsilon^2) \end{aligned} \tag{B.1}$$

where

$$\begin{aligned} \delta &= \langle Q_- \rangle - \langle Q_+ \rangle \\ \epsilon &= \langle Q_- \rangle + \langle Q_+ \rangle = 2\mu(Q) \end{aligned}$$

The quantity δ is called the *charge separation* and ϵ is called the *charge offset*. Using $\langle Q_F Q_B \rangle = \langle Q_- Q_+ \rangle$ and $\epsilon^2 = 4\mu^2(Q)$ and rewriting equation B.1 gives:

$$\begin{aligned} \delta^2 &= 4\{-\langle Q_- Q_+ \rangle + \mathrm{cov}[Q_-, Q_+]\} + \epsilon^2 \\ &= 4\{-\langle Q_F Q_B \rangle + \mathrm{cov}[Q_-, Q_+] + \mu^2(Q)\} \end{aligned} \tag{B.2}$$

If we assume that $\sigma(Q_-) = \sigma(Q_+)$, for which there are good physical grounds and the Monte Carlo confirms, then the covariance can be rewritten in terms of the correlation,

$\rho[Q_-, Q_+]$, as:

$$\begin{aligned} \mathrm{cov}[Q_-, Q_+] &= \rho[Q_-, Q_+]\sigma(Q_-)\sigma(Q_+) \\ &= \rho[Q_-, Q_+](\sigma^2(Q) - \frac{1}{4}\delta^2) \end{aligned} \tag{B.3}$$

where we have used:

$$\begin{aligned} \sigma^2(Q) &= \langle Q^2 \rangle - \langle Q \rangle^2 \\ &= \frac{1}{2}\langle Q_-^2 \rangle + \frac{1}{2}\langle Q_+^2 \rangle - (\frac{1}{2}\langle Q_- \rangle + \frac{1}{2}\langle Q_+ \rangle)^2 \\ &= \frac{1}{2}\sigma^2(Q_-) + \frac{1}{2}\sigma^2(Q_+) + \frac{1}{4}\delta^2 \end{aligned} \tag{B.4}$$

Hence the equation for δ becomes:

$$\delta^2 = 4\left(\frac{-\langle Q_F Q_B \rangle + \rho[Q_-, Q_+]\sigma^2(Q) + \mu^2(Q)}{1 + \rho[Q_-, Q_+]}\right) \tag{B.5}$$

References

[1] F. Halzen and A.D. Martin, *Quarks and Leptons: An Introductory Course in Modern Particle Physics*, John Wiley and Sons, 1984.

[2] S.L. Glashow, Nucl. Phys. **22** (1961) 579.

[3] A. Salam, in : 'Elementary Particle Theory', ed. N. Svartholm, Almqvist and Wikel (1968), 361.
S. Weinberg, Phys. Rev. Lett. **19** (1967) 1264.

[4] T.D. Lee and C.N. Yang, Phys Rev. **98** (1955) 1501.
C.S. Wu *et al.*, Phys. Rev. **105** (1957) 1413.

[5] P.W. Higgs, Phys. Lett. **12** (1964) 132;
Phys. Rev. Lett. **13** (1964) 508;
Phys. Rev. **145** (1966) 1156.

[6] LEP Electroweak Working Group, *Lower Bound for the SM Higgs boson mass: combined result from the four LEP experiments*, contribution Jerusalem, 1997.

[7] LEP Electroweak Working Group, *A combination of Preliminary Electroweak Measurements and Constraints on the Standard Model*, contribution Jerusalem, 1997.

[8] ATLAS Collaboration, Letter of Intent CERN-LHCC/92-4 (1992);
Technical Proposal CERN-LHCC/94-43 (1994).
CMS Collaboration, Letter of Intent CERN-LHCC/92-3 (1992);
Technical Proposal CERN-LHCC/94-38 (1994).

[9] H. Fritzsch, M. Gell-Mann and H, Leutwyler, Phys. Lett. **B47** (1973) 365.

[10] N. Cabibbo, Phys. Rev. Lett. **10** (1963), 531.

[11] S.L. Glashow, J. Iilopoulos and L. Maiani, Phys. Rev. **D2** (1970), 1285.

[12] M. Kobayashi and T. Maskawa, Prog. Theor. Phys. **49** (1973), 652.

[13] J.H. Christenson, J. Cronin, V. Fitch and R. Turlay, Phys. Rev. Lett. **13** (1964), 138.

[14] R.M. Barnett et al., Physical Review **D54** (1996), 1.

[15] LEP Electroweak Working Group, CERN-PPE/96-183, December 1996.

[16] E.J. Eichten, C.T. Hill and C. Quigg, *Orbitally Excited Heavy-Light Mesons Revisited,* Fermilab-Conf-94/118-T (1994).

[17] D.G. Charlton, BHAM-HEP/95-01, November 1995.

[18] S. Myers and E. Picasso, *The design, construction and commissioning of the CERN Large Electron-Positron collider*, Contempory Physics, volume 31, number 6, (1990).

[19] D. Decamp *et al.* (ALEPH), Nucl. Instr. and Meth. **A294** (1990) 121.

[20] P. Aarnio *et al.* (DELPHI), Nucl. Instr. and Meth. **A303** (1991) 233.

[21] B. Adeva *et al.* (L3), Nucl. Instr. and Meth. **A289** (1990) 35.

[22] OPAL Collaboration, K. Ahmet *et al.*, Nucl. Instrum. Methods **A305** (1991) 275.

[23] P.P. Allport *et al.*, Nucl. Inst. and Meth. **A324** (1993) 34.
P.P. Allport *et al.*, Nucl. Inst. and Meth. **A346** (1994) 479.

[24] J.R. Carter *et al.*, Nucl. Inst. and Meth. **A286** (1990) 99.
J.M. Roney *et al.*, Nucl. Inst. and Meth. **A279** (1989) 236.

[25] R.D. Heuer and A. Wagner, Nucl. Inst. and Meth. **A265** (1988) 11.
H.M. Fischer *et al.*, Nucl. Inst. and Meth. **A252** (1986) 492.

[26] H. Mes *et al.*, Nucl. Inst. and Meth. **A265** (1988) 445.

[27] A. ji-Gang *et al.*, Nucl. Inst. and Meth. **A267** (1988) 386.

[28] C. Beard *et al.*, Nucl. Inst. and Meth. **A286** (1990) 117.

[29] R.M. Brown *et al.*, IEEE Trans. Nucl. Sci. **30** (1983) 479.
M. Akrawy *et al.*, Nucl. Inst. and Meth. **A290** (1990) 76.

[30] A.H. Ball, 'Calorimetry in the OPAL Experiment at LEP', proceedings of the Beijing Calorimetry Symposium (October 1994). OPAL Conference Report CR-199 (unpublished).
P. Mättig, 'Photon Energy Resolution in the Lead Glass Calorimeters', OPAL technical note TN-324 (1995) (unpublished).

[31] A.H. Ball *et al.*, IEEE Trans. Nucl. Sci. **37** (1990).
G. Artusi *et al.*, Nucl. Inst. and Meth. **A279** (1989) 523.

[32] G. Bella *et al.*, Nucl. Inst. and Meth. **A252** (1986) 503.
G. Mikenberg *et al.*, Nucl. Inst. and Meth. **A265** (1988) 223.

[33] J. Allison *et al.*, Nucl. Inst. and Meth. **A236** (1985) 284.

[34] G.T.J. Arnison *et al.*, Nucl. Inst. and Meth. **A294** (1990) 431.

[35] D.C. Imrie *et al.*, Nucl. Inst. and Meth. **A238** (1989) 515.

[36] B.E. Anderson *et al.*, IEEE Trans. Nucl. Sci. **41** (1994) 845.

[37] M. Mannelli, OPAL Physics Note **PN142** (1994)

[38] M. Arignon *et al.* (OPAL), Nucl. Instr. and Meth. **A313** (1992) 103.

[39] S. Weisz, D. Lellouch, C. Hawkes, M. Redmond and O. Schaille, *The ROPE Users Guide* Version 409, OPAL internal note.

[40] D. Ward and P. Ward, *The GOPAL Primer* Version 133, OPAL internal note.

[41] J. Allison *et al.*, Nucl. Instr. and Meth. **A294** (1990) 431.

[42] T. Sjöstrand, Comp. Phys. Comm. **39** (1986) 347; JETSET

[43] G. Marchesini, B.R. Webber, G. Abbiendi, I.G. Knowles, M.H. Seymour and L. Stanco, Computer Phys. Comm. **67** (1992) 465; HERWIG 5.8

[44] S. Jadach, B.F.L. Ward, and Z. Was, Comp. Phys. Comm. **66** (1991) 276; KORALZ

[45] S. Jadach, J.H. Kuhn, and Z. Was, **CERN-TH-5856/90** (1990); TAUOLA.

[46] JADE Collaboration, W. Bartel *et al.*, Z. Phys. **C33** (1986) 23.
JADE Collaboration, S. Bethke *et al.*, Phys. Lett. **B213** (1988) 235.

[47] OPAL Collaboration, M.Z. Akrawy *et al.*, Z. Phys. **C49** (1991) 375.

[48] T. Sjöstrand, Comp. Phys. Comm. **39** (1986) 347.
T. Sjöstrand and M. Bengtsson, Comp. Phys. Comm. **43** (1987) 367.
T. Sjöstrand, CERN-TH.6488/92.

[49] OPAL optimised parameters were used, as described in
OPAL Collaboration, M.Z. Akrawy *et al.*, Z. Phys. **C47** (1990) 505 and
OPAL Collaboration, P. Acton *et al.*, Z. Phys. **C58** (1993) 387.

[50] T. Sjöstrand, CERN-TH/93-7112 (revised August 1995).

[51] R.J. Hemingway, *An OPAL Tune of JETSET7.4 Using Z0 Data*, OPAL Technical Note TN279.

[52] J. Allison *et al.,* Phys. Rev. **A317** (1992) 47.

[53] OPAL Collaboration, G. Alexander *et al.*, Z. Phys. **C52** (1991), 175.
T. Mori, 'Multihadronic Cross Section in 1990', OPAL Technical Note TN-025 (1990) (unpublished).
G. Duckeck, 'Large Acceptance Multihadron Selection', OPAL Technical Note TN-086 (1992) (unpublished).

[54] S.L. Lloyd, 'The OPAL Primer (version 3.0)', OPAL Internal Note (1995).

[55] R.V. Kowalewski, ‘A Study of Jet Finding for b Physics in OPAL’, OPAL Technical Note TN-180 (1993) (unpublished).

[56] JADE Collaboration, S. Bethke *et al.*, Phys. Lett. **B213** (1988), 235.

[57] OPAL Collaboration, M. Akrawy *et al.*, Z. Phys. **C49** (1991), 375.

[58] UA1 Collaboration, G. Arnison *et al.*, Phys. Lett. **B132** (1983), 214.
UA1 Collaboration, G. Arnison *et al.*, Phys. Lett. **B123** (1983), 115.
UA2 Collaboration, J. Alitti *et al.*, Phys. Lett. **B257** (1991), 232.
CDF Collaboration, F. Abe *et al.*, Phys. Rev. **D45** (1992), 1448.

[59] OPAL Collaboration, R. Akers *et al.*, Z. Phys. **C68** (1995), 179.
L.A. del Pozo, ‘Tests of QCD from Jet and Hadron Production at LEP’, Ph.D. Thesis, Cambridge University (1993).

[60] R. Hawkings and S. de Jong, ‘The Beam Spot Location in OPAL in 1994 Data’, OPAL Technical Note TN-321 (1995) (unpublished).
S. de Jong, ‘Determination of the LEP Beam Spot Location in OPAL. An Update of TN041’, OPAL Technical Note TN-251 (1994) (unpublished).
S. de Jong, ’Determination of the LEP Beam Spot Location in OPAL with Pass 3 Data’, OPAL Technical Note TN-041 (1991) (unpublished).

[61] R.V. Kowalewski, ‘A Study of Lifetime Tagging of b Hadrons in OPAL’, OPAL Technical Note TN-181 (1993) (unpublished).

[62] R.V. Kowalewski and P.S. Wells, ‘BTagging Software (version 108/29)’, OPAL Internal Note (1993).

[63] OPAL Collaboration, ‘Measurement of the Average B Mixing Probability on the Z^0 Resonance using Leptons and a Jet Charge Method’, OPAL Physics Note PN-208 (1996).

[64] OPAL Collaboration, R. Akers *et al.*, Z. Phys. **C65** (1995) 17.

[65] OPAL Collaboration, R. Akers *et al.*, Z. Phys. **C67** (1995) 365.

[66] Oliver Cooke, *Evaluating the effects of a lifetime tag on the charge separation of b quark events*, OPAL Technical Note TN316.

[67] L. Montanet et al., Physical Review **D50** (1994), 1173.
A 1995 off-year partial update for the 1996 edition is available on the Particle Data Group WWW pages (`http://pdg.lbl.gov/`).

[68] D. Bardin *et al.*, CERN-TH 6443/92, May 1992.

[69] LEP Electroweak Working Group, CERN-PPE/95-172, November 1995.

[70] Masahiro Morii, Private Communication, (1995).

[71] OPAL Collaboration, G. Alexander *et al.*, CERN-PPE/95-179, December 1995.

[72] ALEPH Collaboration, D. Buskalic *et al.*, Phys. Lett. **B284** (1992) 177.

[73] ALEPH Collaboration, D. Buskalic *et al.*, Z. Phys. **C62** (1994) 179.

[74] DELPHI Collaboration, P. Abreu *et al.*, Phys. Lett. **B322** (1994) 459.

[75] DELPHI Collaboration, P. Abreu *et al.*, Phys. Lett. **B332** (1994) 488.

[76] L3 Collaboration, M. Acciarri *et al.*, Phys. Lett. **B335** (1994) 542.

[77] ALEPH Collaboration, D. Buskalic *et al.*, CERN-PPE/95-108, July 1995.

[78] DELPHI Collaboration, P. Abreu *et al.*, Phys. Lett. **B345** (1995) 598.

[79] OPAL Collaboration, R. Akers *et al.*, Z. Phys. **C66** (1995) 19.

[80] DELPHI Collaboration, contribution eps0563, Brussels, 1995.

[81] R. Kowalewski, Study of lifetime tagging of b hadrons in OPAL, OPAL Technical Note TN181, 18th August 1993.

[82] OPAL Collaboration, QCD Studies Using a Cone-based Jet Finding Algorithm for e+e- Collisions at LEP, R. Akers *et al.*, Z. Phys. **C63** (1994) 197.

[83] OPAL Collaboration, A Measurement of the Average Bottom Hadron Lifetime, K. Ackerstaff *et al.*, Z. Phys (1996).

[84] OPAL Collaboration, K.Ackerstaff *et al.*, Z. Phys. **C74** (1997) 413.